



UNIVERSITÀ  
DEGLI STUDI  
DI PADOVA

Sede Amministrativa: Università degli Studi di Padova  
Dipartimento di Geoscienze

---

SCUOLA DI DOTTORATO DI RICERCA IN: SCIENZE DELLA TERRA  
CICLO XXV

**FROM DEEP - SEATED GRAVITATIONAL MOVEMENTS TO  
ROCK AVALANCHES: THE ROLE OF FAILURE  
MECHANISM IN SUDDEN ROCK SLOPE COLLAPSE.**

**Direttore della Scuola:** Ch.mo Prof. Massimiliano Zattin

**Supervisore:** Ch.mo Prof. Rinaldo Genevois

Dott. Matteo Massironi

Ch.mo Prof. Douglas Stead

**Dottorando :** Luca Zorzi



# Abstract

This project is focused on understanding the processes of failure evolution (from triggering to propagation) and deformation mechanisms of Deep Seated Gravitational Movement (DSGSD) and Rock Avalanches (RA) in massive brittle rock slopes. In particular, the focus of this work is directed to the failure mechanism of these phenomena, the influence of failure mechanisms on the slope stability and dynamics of the collapse. This research aims to improve the understanding and modeling of brittle fracture and progressive failure in massive metamorphic rock slopes through a combination of structural geology, geomechanics, geomorphology, numerical and experimental modeling.

Triggering factors and failure mechanisms were studied on one mass wasting phenomenon in the Eastern Alps (Ridnaun Valley Rock Avalanche). The left slope of the Ridnaun Valley (Sterzing/Vipiteno, South Tyrol, Italy), set on the crystalline units of the Austroalpine Nappe of the alpine orogenic wedge, shows evidence of quaternary gravitational evolution which highly depends on the brittle/ductile structural setting of the slope. Detailed field work and LiDAR-derived digital elevation model analysis clearly revealed different gravitational movements. A fully evolved gravitational collapse, having the typical features of a Rock Avalanche (RA), characterizes the central part of the slope; whereas to the east and west of the RA, deep-seated gravitational slope deformations, pointed out for the first time with this research, still involve the slope.

Making use of different approaches, such as geomorphology, structural geology and geomechanical analysis, and numerical modeling, the present work shows how the brittle/ductile tectonic setting acts on one hand as primary controlling factors of the detected large mass movements; on the other hand, can control the evolutionary type of failure (i.e.: rock avalanche).

It is expected that the findings obtained through this investigation will enhance our fundamental knowledge on DSGSD evolutionary type on poly-deformed metamorphic masses, particularly with regard to understanding the key stages of the progressive evolution of rock slope failures from a secondary creep stage to the sudden collapse.

# Riassunto

Questo progetto di ricerca ha come focus la comprensione dei meccanismi di deformazione e di collasso (dall'innescò alla propagazione della rottura) che governano Deformazioni Gravitative Profonde di Versante (DGPV) e valanghe di roccia (rock avalanches) in versanti rocciosi. In particolare, l'attenzione primaria di questo lavoro è indirizzata ai meccanismi di propagazione della rottura, alla loro influenza sulla stabilità dei versanti ed alle dinamiche del collasso. Lo scopo principale è migliorare le conoscenze ed i modelli relativi ai meccanismi di fratturazione e di rottura progressiva in ammassi rocciosi foliati, attraverso un approccio multidisciplinare che prevede l'analisi del versante con tecniche geologico - strutturali, geomorfologiche, geomeccaniche e di modellazione numerica.

Cause innascenti e meccanismi di rottura progressiva sono stati analizzati prendendo come caso studio un collasso gravitativo di grandi dimensioni nelle Alpi orientali (la rock avalanche della Val Ridanna). Il versante sinistro della Val Ridanna (Sterzing/Vipiten, Alto Adige, Italia), collocato geologicamente nelle unità cristalline della falda Austroalpina del prisma orogenetico delle Alpi, mostra evidenze un'evoluzione gravitativa quaternaria di tipo differenziale, la quale è fortemente controllata dall'assetto geologico duttile/fragile delle unità metamorfiche costituenti il versante. Indagini di terreno, unite ad una dettagliata analisi del modello digitale del terreno ottenuti da acquisizioni LiDAR, ha permesso di riconoscere differenti deformazioni gravitative all'interno del versante studio. La parte centrale della valle è caratterizzata da un evidente accumulo derivante da un collasso gravitativo di tipo rock avalanche; lungo il versante, ad ovest ed ad est dell'area sorgente della rock avalanche, due DGPV, riconosciute per la prima volta grazie a questo lavoro, coinvolgono il versante.

Il presente lavoro mostra come l'assetto duttile/fragile agisca da un lato come fattore predisponente alle deformazioni gravitative riconosciute; dall'altro controlla direttamente le modalità evolutive delle deformazioni stesse.

Si ritiene che i risultati ottenuti da questa tesi di dottorato possano contribuire al miglioramento delle conoscenze sull'evoluzione di DGPV in rocce metamorfiche polideformate, in particolare per quanto concerne i meccanismi che governano l'evoluzione parossistica di una massa in deformazione lenta.



# Index

1.	Introduction .....	12
1.1	Statement of the problem.....	12
1.2	Rock - slope deformations and failures .....	13
1.2.1	Brittle rock progressive failure and its implication for slope stability.....	15
1.2.2	Modeling brittle rock failure in numerical analysis .....	17
1.3	Aims and objectives.....	17
1.4	Thesis structure.....	18
2.	Methods and Materials .....	20
2.1	Introduction .....	20
2.2	Geological and geomorphological characterization .....	20
2.2.1	Topographic base map .....	20
2.2.2	Airborne Laser Scanner – High Resolution Digital Elevation Model (ALS-HRDEM).....	20
2.2.3	Aerial photos and orthophotos interpretation.....	21
2.2.4	Faults mapping .....	21
2.2.5	Structural analysis .....	21
2.3	Geomechanical characterization.....	22
2.3.1	Electronic “SilverSchmidt” Schmidt hammer.....	23
2.3.2	RocLab .....	24
2.3.3	Dips .....	24
2.3.4	Geological Strength Index (GSI).....	25
2.3.5	Rock quality designation index (RQD).....	25
2.3.6	Rock Mass Rating (RMR).....	26
2.3.7	Slope Mass Rating (SRM).....	27
2.4	Laboratory techniques .....	27
2.4.1	Point load test.....	27
2.4.2	Uniaxial and Triaxial compressive tests.....	28

3.	Numerical modelling techniques for progressive rock slope failure simulation.....	36
3.1	Introduction .....	36
3.2	Numerical methods for rock mechanics problems .....	36
3.3	Hybrid elasto – plastic finite element method: Phase2.....	38
3.4	Modeling brittle fracture of rocks.....	39
3.5	Hybrid FEM/DEM model – ELFEN code (Rockfield) .....	40
4.	Inherited structures and slope evolution: the case of the left slope of the Ridnaun Valley	44
4.1	Introduction .....	44
4.2	Geological and geomorphological setting .....	45
4.3	Material and Methods .....	47
4.4	Geomorphology of the left slope of the Ridnaun Valley.....	49
4.4.1	Western sector .....	50
4.4.2	Central sector.....	51
4.4.3	Eastern sector .....	52
4.5	Interferometry data .....	53
4.6	Geomechanical analysis .....	54
4.7	Structural analysis.....	55
4.8	Gravitational evolution of the left slope of the Ridnaun Valley.....	56
4.8.1	Wetterspitz DSGSD .....	57
4.8.2	Telfer Weissen DSGSD. ....	58
4.8.3	The Ridnaun rock avalanche .....	59
4.9	Discussion.....	59
4.10	Conclusions.....	61
4.11	Tables.....	63
4.12	Figure captions.....	64
5.	Rock mass properties .....	80
5.1	Introduction .....	80

5.2	Discontinuity characterization .....	80
5.2.1	Spacing .....	81
5.2.2	Joint compressive strength (JCS) and Joint roughness coefficient (JRC).....	81
5.3	Rock mass classification.....	82
5.3.1	Geological strength index.....	82
5.4	Intact rock characterization .....	83
5.4.1	Point load tests .....	84
5.4.2	<i>Uniaxial compression tests</i> .....	85
5.5	Geomechanical domains.....	87
5.6	Figure Captions.....	102
6.	A FEM/DEM approach for modeling progressive failure in foliated rock slopes: the Ridnaun rock avalanche .....	110
6.1	Introduction .....	110
6.2	Progressive failure in rock slopes.....	111
6.2.1	The Ridnaun rock avalanche .....	113
6.3	Numerical analysis of progressive failure initiation and propagation.....	114
6.3.1	Material and methods .....	114
6.3.2	Valley excavation approach .....	116
6.3.3	Modeling of process initiation.....	116
6.3.4	Modeling of brittle fracture initiation and propagation.....	119
6.4	Discussion and conclusion.....	120
6.5	Figure Captions.....	122
7.	Conclusions .....	128
8.	References .....	132
9.	Appendix A .....	150

# Index of figures

Figure 2.1: <i>Shaded relief image of ALS – HRDEM</i> .....	30
Figure 2.2: Rock joint roughness profiles showing the typical range of JRC (after Barton and Chubey 1977). .....	31
Figure 2.3: Concrete test hammer “Silverschmidt”. .....	31
Figure 2.4: GSI table proposed by Marinatos and Hoek (2000). .....	32
Figure 2.5: example of a point load test apparatus.....	33
Figure 2.6: the automatic system ADVANTEST9 and SERCOMP7, available at the Rock Mechanics lab of the Geosciences department of the University of Padova (developed, produced and solded by Controls-Italia s.r.l.). .....	33
Figure 2.7: Hoek cell used for triaxial tests. ....	34
Figure 4.1: Geographical and geological setting of the study area; a) Geographical map of northern Italy; b) Structural map of the eastern Alps (from Sölva et al, 2005, modified); the rectangle represent the location of the study area c) Geodynamic model of the Schneeberg Normal Fault Zone (from Bestmann et al, 2011, modified).....	64
Figure 4.2: Distribution of seismic event between northern Italy – South Austria.....	64
Figure 4.0.3: Map of the location of the Geomechanical station along the slope. As base map, a shaded relief image of ALS-HRDEM was used.....	64
Figure 4.4: Map of the distribution of GSI values. The values show a discrete areas characterized by N-S distribution of the values. ....	64
Figure 4.5: Simplified geological map of the left slope of the Ridnaun valley on shaded relief image of ALS-HRDEM; a) contour plot of the foliations measured in the ÖSC (number of measures: 160); b) contour plot of the foliations measured in the SMU (number of measures: 130); c) contour plot of the crenulation cleavages measured within both the complex (number of measures:100); .....	64
Figure 4.6: Shaded relief image of ALS-HRDEM showing the subdivision of the slope into three sectors: Western, Central and Eastern. The rockslide body is visible in the eastern sector of the rock avalanche deposit, with a clear source area located on the slope. The rectangle a, b and c are related defined the location of the field images of Figure 4.8; .....	64
Figure 4.7: 3D ALS-HRDEM image of the study area (perspective view from the SE). The A-A’ profile (Western) shows a near-stable geometry, with a slightly concavity, followed by an incipient bulging in the central sector of the slope; the B-B’ profile (Central sector) highlights a strongly irregular topography, resulting from a fully evolved rock slope collapse; the C-C’ profile is the expression of an an unbalanced geometry: the uphill sector is	

characterized by a strong irregular topography due to the presence of a glacial cirque and morphostructures; the downhill part shows evidence of a bulge induced most by the DSGSD deformation. .... 64

Figure 4.8: Geomorphic features affecting each sector; a) field evidence of scarps and trenches relative to the Wetterspitz DSGSD (Western sector; view from the W); b) Geomorphic features deriving from the ongoing toppling evolution of the rock avalanche niche (Central sector; view from the W); c) Mainly trenches and scarps defining the crown area of the Telfer Weissen DSGSD (Eastern sector; view from the NW); d) polished surfaces indicating high rates of ongoing activity recorded by the morphostructures. .... 64

Figure 4.9: Outcrop of the rock avalanche deposit (image taken looking towards the south). 64

Figure 4.10: DS-InSAR interferometry map derived from Radarsat data (courtesy of the Geological Survey of the Autonomous Province of Bolzano). The image shows only LOS-displacement along a descending orbit (NE- Line of sight)..... 64

Figure 4.11: Contour plot of the brittle discontinuities measured in the field during both geological and geomechanical surveys; a) contour plot of the faults detected in the field (number of measures: 50); F1, F2 and F3 define the three fault sets detected, whereas UTC defines the ultracataclastic fault detected mainly in the ÖSC; b) contour plot of all the joint measured on the entire slope (number of measures: 1023); K1 set is the expression of a brittle reactivation of the hinge zone of Sr folds; K2 set follows the F2 fault set (see image a in this figure) ; K3 follows the UTC faults; K4 is the expression of the factures induce by F1 faults and the S set is the brittle reactivation of the Sr foliation ; c) contour plot of the joint sets measured on the Western sector (number of measures: 615); only the K1, K3, K4 and S sets were detected; d) contour plot of the joint sets measured on the Central sector (number of measures: 169); in this sector only K2 ans S set were detected; e) contour plot of the joint set measured in the Eastern sector (number of measures: 208); this sector is the only one showing all five discontinuity sets..... 64

Figure 4.12: a) Field example of the garnet-micaschists of the SMU; b) C'-type shear band cleavage found in the garnet-micaschists; In dashed red line the C'- structures; reaction rims (mainly sigma-type) accompany the garnet porphyroblasts;c) crenulation cleavage of the garnet-micaschists of the SMU; d) Field evidence of the low angle N-dipping ultracataclastites; in specific, the image represent an incoherent ultracataclasite; e) field expression of F1 and F2 fault sets; the picture show a F2 fault, defined by a damaged fault core having the thickness of about 1-1.5 m filled by an incoherent fault breccia..... 65

Figure 4.13: Geological and geomprphological setting of the detected rock slope instabilities; a) geology of the Wetterspitz DSGSD; the DSGSD involves mainly paragneisses ÖSC than

the SMU. b) zoom on the rock avalanche crown area; scarps and trenches define ongoing gravitational deformation affecting the area; c) Geology of the Telfer Weissen DSGSD; the DSGSD involves mainly the garnet micaschists of the SMU, confining the ÖSC in its crown area. .... 65

Figure 4.14: Geological section of the detected deep-seated deformation; traces of the sections are the one for the topographic profile of figure 4.6. a) geological cross-section of the Wetterspitz DSGSD; b) geological cross-section of the Ridnaun rock avalanche; the dashed black line represent the hypostasized pre-failure topography; c) geological cross-section of the Telfer Weissen DSGSD; uncertainties still remains on the width of the deforming area. .... 65

Figure 5.1: Histogram graphs of the distribution of spacing and JCS in the SMU and OSC complex; a) histogram graph of the spacing distribution in the ÖSC; b) histogram graph of spacing distribution in the SMU; c) histogram graph of the JCS values collected on the SMU; d) histogram of the JCS values collected on the ÖSC. .... 99

Figure 5.2: Histogram of the distribution of GSI within the SMU and OSC complex in the Western and Eastern sector; a) histogram graph of the GSI distribution along the SMU in the Western sector; b) histogram graph of the GSI distribution along the ÖSC in the Western sector; c) histogram graph of the GSI distribution along the SMU in the Eastern sector; d) histogram graph of the GSI distribution along the ÖSC in the Eastern sector. .... 99

Figure 5.3: Failure strength versus  $\beta$  for gneiss samples of ÖSC and garnet – micaschists samples of SMU. .... 99

Figure 5.4: Stress – strain curves of gneiss samples of ÖSC; ..... 99

Figure 5.5: Stress – strain curves of garnet – micaschists of SMU; ..... 99

Figure 5.6: Distribution of UCS values compared to Young’s modulus and Poisson’s ration in the ÖSC; a) distribution of UCS versus  $E_{\tan 50}$ ; b) distribution of UCS versus Poisson’s ratio.

Figure 5.7: Distribution of UCS values compared to Young’s modulus and Poisson’s ration in the SMU; a) distribution of UCS versus  $E_{\tan 50}$ ; b) distribution of UCS versus Poisson’s ratio.

Figure 5.8: Map of geomechanical domanis derived from field and laboratory geomechanical analysis. Base map: shaded relief image of ALS – HRDEM. .... 99

Figure 6.1: Finite-element continuum modelling of glacial loading and unloading process. The staged simulation includes: a) initial bedrock conditions, b) shaping of the valley through glaciation and replacement of the rock by glacial ice; c) retreat of glacier in 5 stages;

Figure 6.2: N – S topographic profile of the Ridnaun valley; ..... 119

Figure 6.3: Finite – element Phase<sup>2</sup> simulation. The images referre to continuum modelling of glacial erosion and unloading process on basal shear zone development; a) Shear strain distribution; b) shear strain distribution coupled with yielding elements. .... 119

Figure 6.4: Finite – element Phase2 simulation. The images referre to continuum modelling of seismic effect on basal shear zone development and stability of the studied slope; a) Shear strain distribution; b) shear strain distribution coupled with yielding elements.....119

Figure 6.5: Hybrid finite/discrete – element model employing a Mohr – Coulomb with Rankine tensile cut – off, showing a progressive fracturing widely distributed below the glacial shoulder. .... 122

## Index of tables

Table 3.1: Material properties that have to be specified as input parameters for a “Mohr – Coulomb – Rankine tensile cut – off” analysis (after Elmo, 2006). .... 43

Table 4.1: principal morphometric parameters of the Wetterspitz DSGSD ..... 63

Table 4.2: principal morphometric parameters of the Telfer Weissen DSGSD..... 63

Table 5.1: geomechanic data collected during geomechanical surverys. In this table, RMR and SRM rock mass classification are presented. .... 91

Table 5.2: geomechanical caractereization of the 20 scan line type surveys. .... 93

Table 5.3: point load tests performed on the paragneiss of the ÖSC. .... 95

Table 5.4: point load tests of the garnet – micaschists of the SMU. .... 96

Table 5.5: Summary of the uniaxial compressive tests performed on rock samples related to the ÖSC. .... 97

Table 5.6: Summary of the uniaxial compressive tests performed on rock samples related to the SMU. .... 98

Table 5.7: Principal mechanical paramenters definig the different joint sets within the different domains..... 99

Table 5.8: Strength paramenters evaluated starting from the Q – system..... 100

Table 5.9: rock mass strength paramenters evaluated using Hoek and Brown strength criterion based on GSI. Data calculated using RocLab software (Rocscience)..... 101

# 1. Introduction

## 1.1 Statement of the problem

Deep Seated Gravitational Slope Deformations (DSGSDs), also referred to as creep or rock flows (Radbruch-Hall, 1978; Agliardi et al., 2001, 2012), involve large rock volumes and cause important morphologic changes due to lateral and vertical movements of the rock mass. Different factors such as structural and geological settings, hydrogeological and geomechanical characteristics, seismic events and unloading due to glacial retreat may control both the triggering and development of DSGSDs (Varnes et al. 1989; Bovis and Evans, 1996; Agliardi et al., 2001, 2012). Usually such large-scale mass movements are characterized by a low probability of evolution into a catastrophic event, but in the worst-case scenario they can result in significant direct or indirect damage and thus represent important hazards (Bonnard et al., 2004). They can indeed represent the incipient stage of hazardous large-scale mass movements both for the extensive area and volumes involved and for their possible catastrophic evolution in large scale phenomena such as rockslides (e.g. Vajont rockslide) or rock avalanches (e.g. Val Pola, Karakoram Himalaya, New Zealand) (Hewitt, 1999, Crosta et al. 2006, Hewitt et al, 2008, McColl and Davies, 2010). In particular, a Rock Avalanche (R.A.) is unequivocally characterized by the sudden release of massive volumes ( $> 10^6$  m<sup>3</sup>) of rocks which are reduced in particle size, so resembling, in its descent downhill an avalanche.

Generally, the temporal evolution of DSGSDs has been studied through analysis of the counterscarp deposits, giving among other things relative ages of the slope movements. Quantitative estimation of deformation rate and identification of reactivation phases is quite rare (Hippolyte et al. 2006). Considering a specific area, the danger of these catastrophic events is determined through a combination of the *time factor* (instantaneous collapse), and the areal extent of their *propagation* (runout). Due to their nature, it is extremely difficult to predict when the catastrophic failure will occur. In addition, determining the propagation of the phenomenon is a complex matter, which can be tackled only by studying rock avalanche behaviour from past events. Indeed, these phenomena may repeatedly affect the same areas over time, due to their unfavourable conditions. The risk of recurrences of devastating phenomena over the same areas is often underestimated because of the large time interval separating two subsequent events. For this reason, towns, villages and infrastructures have been frequently rebuilt over ancient deposits from past landslide activity.



## 1.2 Rock - slope deformations and failures

Deep-Seated Gravitational Slope Deformations (DSGSD) affecting valley walls are very common in the Alps, governing the evolution of mountain landscapes and the related hazards (Mortara and Sorzana, 1987, Crosta, 1996; Agliardi et al, 2001, 2009, 2012). DSGSDs are large mass movements on high-relief slopes that normally extend from near the valley floor to, or beyond, the ridge crest (Agliardi et al., 2012). Deformations at the level of large slopes were first observed during 1940s (Ampferer, 1939; Stini, 1941; Terzaghi, 1963), and DSGSD were first studied in detail by Zischinsky (1966, 1969), Nemcok et al. (1972), and Mahr and Nemcok (1977).

The deformation mechanism related to these phenomena is commonly referred to as creep (Radbruch-Hall, 1978; Hutchinson, 1988, Chigira, 1992; Chigira and Kiho, 1994), and is characterized by low to extremely low deformation rates (Cruden and Varnes, 1996, Agliardi et al., 2012). Common field indicators of these phenomena are surface deformational features such as double ridges, scarps and counterscarps (Agliardi et al., 2001, 2012). Chigira (1992) and Chigira and Kiho (1994), illustrated how many tectonic features, such as brittle faults and folds, cataclastic bands) can be produced at the slope scale by mass movement, and thus taken as field indication of rock mass creep. Toes of many DSGSDs lie below valley floors, and can be covered by alluvial or lacustrine sediments (Agliardi et al., 2012). Commonly, secondary rock failures affect the lower parts of DSGSDs, leading in some case to large catastrophic failures (Agliardi et al., 2012). As suggested by Agliardi et al. (2012), interpreting the kinematic significance of surface geomorphic features, their spatial geometries and associations is crucial for the definition of the overall geometry and kinematics of DSGSD, due to the lack of deep exposure or site investigation data. DSGSDs basal shear zones have been observed or inferred at dam sites (Barla et al., 2010; Agliardi et al., 2012) and in borehole logs (Ambrosi e Crosta, 2006; Bonzanigo et al., 2007; Zangerl et al., 2007).

In the Italian Alps, DSGSDs are very common, and in the last decades several phenomena have been investigated in detail (Mortara and Sorzana, 1987; Crescenti et al., 1994; Agliardi et al, 2001, 2009, 2012; Bistacchi and Massironi, 2001; Massironi et al., 2003, 2010; Eberhardt et al., 2004; Soldati et al., 2006; Ambrosi and Crosta, 2006; Bonzanigo et al., 2007; Ghirotti et al., 2011; Gischig et al., 2011a and b; Löw et al, 2012; Zorzi et al., accepted - pending revision). Structural controls and mechanisms

It is widely accepted that the DSGSDs evolution of a slope is strongly controlled by the structural setting of the bedrock. In particular, a close relationship between gravitational morphostructures and brittle tectonic features has been extensively demonstrated (Zischinsky,

1966, 1969; Nemcok, 1972; Radbruch – Hall, 1978; Chigira, 1992; Crosta, 1996; Crosta and Zanchi, 2000; Agliardi et al. 2001, 2009, 2012, Brideau et al., 2009; Jaboyedoff et al., 2009; Ambrosi and Crosta, 2011). These authors emphasized the role of pre - existing fractures for the initiation of large rock - slope instabilities.

Considering large rock slope instability affecting foliated metamorphic rock masses, few studies have investigated in detail and taken into account how, at the slope scale, the inherited ductile framework affects slope stability (Massironi et al., 2003, 2010; Henderson et al., 2006; Brideau et al., 2009; Jaboyedoff et al., 2011; Oppikofer et al., 2011, Zorzi et al, accepted - pending review – in attachment on this thesis).

Several processes have been proposed as potential triggers of DSGSDs (Agliardi et al., 2012). First of all, topographic stresses can interact with tectonic or locked - in stresses inducing shear stress concentration at the toe of the slope along with tensile damage along the ridge area (Varnes et al., 1989; Savage, 1994; Miller and Dunne, 1996; Molnar, 2004; Ambrosi e Crosta, 2011; Agliardi, 2012). This may lead to high relief rock slope instabilities, which can be either catastrophic or progressive depending on rock mass strength (Agliardi et al., 2012). Acceleration or reactivation of DSGSDs can be triggered by ground shaking and coseismic displacements along faults during earthquakes (McCalpin, 1999; Moro et al., 2007; Agliardi et al., 2009b, 2012; Ambrosi and Crosta, 2011).

Large rock - slope instabilities are commonly involving slopes of glacial valleys that have been steepened by recurrent glacial erosion during Pleistocene (Radbruch – Hall, 1978; Bovis, 1982; Caine, 1982; Ballantyne, 2002; Agliardi et al, 2012; see next paragraph).

Retreat of Pleistocene glaciers that left behind unstable over-steepened slopes is to be considered as the main cause for the initiation of these phenomena (Nemcok and Pasek, 1969; Dramis, 1984; Augustinus, 1995; Dikau et al., 1996; Kellerer-Pirklbauer et al., 2010; Ambrosi and Crosta, 2011). Nevertheless, some alpine DSGSDs show evidence of activity covering more than one glacial cycle, with clear evidence of reactivation after successive glaciations (Agliardi et al., 2012).

Until now, the relative influence of controlling factors remains unclear and requires further investigations (Bouissou et al., 2012).

The long - term evolution of DSGSDs (Bovis, 1990; Ballantyne, 2002; Prager et al., 2008), suggested by geomorphological and geochronological evidences, could be related to the concept of progressive failure (Eberhardt et al., 2004; Agliardi et al., 2012).

### *1.2.1 Brittle rock progressive failure and its implication for slope stability*

In rock slope stability analysis, the failure surface is often assumed to be structurally controlled and predefined as a continuous plane or series of interconnected planes. Such assumptions are only valid in cases where the volume of the failed block is relatively small (e.g. thousands of m<sup>3</sup>) or where major persistent faults and/or bedding planes are present and favorably oriented. In massive natural rock slopes, the presence of persistent key discontinuities enabling kinematical release is more limited, and a complex interaction between existing natural discontinuities and brittle fracture propagation through intact rock bridges is required to bring the slope to failure (Bachmann et al., 2009; Eberhardt et al. 2004 and Eberhardt 2008). The shear strength along potential failure surfaces is hence determined partly by the failure through intact rock and partly by shear along discontinuities.

The process of failure through intact rock in massive rock slopes, called progressive failure (Terzaghi, 1962; Eberhardt et al., 2004, Groneng et al. 2010), entail the progressive degradation and destruction of the rock mass cohesive elements (strength degradation processes), manifested through internal mass deformation and damage mechanisms, enabling the kinematic release (Hajiabdolmajid, et al, 2002; Eberhardt et al, 2004; Yan, 2008). Massive rock slopes may not experience a rapid change in kinematic state and frequently have stood in a relative stable condition over periods of thousands of years. The final failure surface may eventually develop through the interconnection of discontinuity affecting the slope. Dilation and internal deformation mechanisms may partly drive the failure processes, which normally should initiate at the toe of the rock slope where stresses are higher (Eberhardt et al., 2004; Stead et al, 2006). This is suggested by the typical DSGSD geomorphic features such as scarps, counterscarps and trenches defining the top of a deforming slope. Progressive failure mechanisms are allowed by simple decrease of rock mass strength due to slopes undercut and erosion (Jaboyedoff et al., 2009; Leroueil, 2001; Cruden and Martin, 2004), with the failure surface that can be controlled either by the geometry of the slope (Golts and Rosenthal, 1993; Jaboyedoff et al., 2004a) or by strength degradation phenomena due to glacial unloading. Agliardi et al. (2001) and Eberhardt et al. (2004) showed that Alpine valley slopes undergo slow destabilization phenomena due to valley reshaping and glacial unloading, triggering progressive failure mechanisms on brittle rock slopes.

According to Augustinus (1995), glaciation and deglaciation cycles influence rock mass stability in two main ways: steepening of rock slopes due to glacial erosion and debuttrass with consequent stress release. Rock-slope steepening increases the self-weight (overburden) shear stress acting within the rock mass (Radbruch – Hall, 1978; Bovis, 1982; Caine, 1982;

Ballantyne, 2002), generating shear stress condition at the toe of the slope (Augustinus, 1995; Eberhardt et al., 2004).

In addition, during valley glaciers retreat and resultant unloading of glacially stressed rocks, strain energy is released (Ballantyne, 2002). The induced stress redistribution results in shifts in the orientation of the principal stress field in the rock mass. Thus, relaxation of tensile stress within the rock mass causes a “rebound” effect of the valley walls, whose magnitude is dependent on the residual strain energy and the modulus of elasticity of the rock (Ballantyne, 2002). Stress release may result in fracture propagation through the internal discontinuity network, along with loss of rock mass cohesion through breaking of rock bridges. Internal deformation mechanisms, damage and strength degradation processes (progressive failure) are considered to be controlled by the structural setting of the rock mass, the characteristics of the discontinuity sets (i.e. low or high persistence joints) and rock mass geology. Indeed, gravitational adjustments of rock slopes driven on one side by the interaction of changing stress conditions due to glacial over - steepening and stress relaxation following glacial debutress, and rock mass strength controlled by lithology and structural setting on the other. Such interaction may act as trigger for i) large scale catastrophic rock slope failure (Agliardi et al., 2001, 2012; Massironi et al, 2010), ii) large scale rock mass deformation (Eberhardt et al., 2004); iii) adjustment of rock faces by discrete rockfall events (Augustinus, 1995; Ballantyne, 2002).

Conventional linear (Mohr – Coulomb) and non-linear (Hoek – Brown) failure criterion govern strength degradation and mobilization processes, assuming implicitly a simultaneous mobilization of the cohesive and frictional strength (Yan, 2008; Barton and Pandey, 2011). This approaches, even when strain-softening models with residual strength parameters are chosen, have not been successful in predicting the damaged area in a rock mass strained beyond its peak strength (Hajiabdolmajiid et al., 2002; Barton and Pandey, 2011). To overcome this issue, Hajiabdolmajid (2001), Hajiabdolmajid et al. (2002), and Hajiabdolmajid and Kaiser (2003), starting from the work of Schmertmann and Osterberg (1960) and Martin and Chandler (1994), adopted a new constitutive based on a strain-dependent cohesion weakening – frictional strengthening (CWFS) to simulate brittle rock slope failure (i.e., Frank slide, Hajiabdolmajid, 2001). With this approach, cohesion degradation and friction mobilization are function of plastic strain ( $\epsilon_p$ ). In brittle failure of strained rock masses, cohesion degradation is driven by time – dependent progressive breaking of intact rock bridges, governing both the progressive development of the failure surface on deforming slopes and long term stability of rock slopes (Kemeny 2003).

Indeed, modeling of progressive shear plane development needs to consider both strength degradation (plastic shear strains evolve and/or tensile fracture develops) and brittle fracture propagation (Eberhardt et al., 2004).

### *1.2.2 Modeling brittle rock failure in numerical analysis*

A model for studying rock slope stability should encompass the nucleation or activation of cracks within the rock, the possible coalescence of which would then lead to the creation of a critical failure surface. In addition, time-dependent mechanisms relating to brittle strength degradation and progressive failure may more likely be the significant contributing factors that brought the slope to failure (Eberhardt et al., 2004).

Different numerical modeling techniques have been developed during the last decade to analyze the role of non-persistent discontinuities sets and fracture propagation through intact rock bridge failure at different scales (Stead and Coggan, 2012). More recently, numerical methods have led to significant enhancement in rock slope stability analysis, which can take into account complex but realistic features (e.g., Discrete Fracture Networks, anisotropy, 3D effects, non-linear behaviour, time and coupled groundwater-mechanical response; Stead and Coggan, 2012). If classical continuous or discrete approaches in their initial formulation do not seem adequate to describe the progressive failure mechanisms in jointed rock, several attempts have been made to extend their capabilities. To date, routine analyses treat slope mass as either a continuum (finite element methods) or as a discontinuum (discrete element methods). The complex interaction existing at failure between natural discontinuities and brittle fracture propagation through rock bridges should be incorporated into large rock slope analyses. A better understanding of the mechanisms responsible for the evolution of catastrophic failures is needed to allow further advances in rock slope hazard assessment; new techniques have evolved such as hybrid finite-/discrete-element codes (ELFEN) which allow simultaneously modeling of both intact rock and joint behaviour (Eberhardt et al., 2004; Rockfield, 2008). These codes can now incorporate Discrete Fracture Networks, DFN's, allowing a more realistic simulation of failure surface propagation in rock slopes (Stead and Coggan, 2012).

## **1.3 Aims and objectives**

This project focuses on the structural and mechanical controls on anisotropy and its influence on fracture propagation, at both the micro- and macro scale with a principal objective of evaluating the initiation and evolution of rock slope instabilities. This research aims to improve the understanding and modeling of brittle fracture and progressive failure in massive

metamorphic rock slopes through a combination of structural geology, geomechanics, geomorphology, numerical and experimental modeling.

The left slope of the Ridnaun Valley (eastern Alps, Italy) was chosen as case study for this research. In fact, the left slope of the Ridnaun Valley, set on the crystalline units of the Austoalpine Nappe of the alpine orogenic wedge, shows evidences of a differential gravitational evolution: a fully evolved gravitational collapse, having the typical features of a rock avalanche, characterizes the central part of the slope; whereas to the east and west of the rock avalanche, deep - seated gravitational slope deformations pointed out for the first time thank to this research, still involve the slope.

Making use of different approaches, such as geomorphology, structural geology and geomechanical analysis, and numerical modeling, the present work shows how the brittle/ductile tectonic setting acts on one hand as primary controlling factors of large mass movements in poly-deformed foliated rock masses; on the other hand, can control the evolutionary type of failure (i.e.: rock avalanche).

#### **1.4 Thesis structure**

The thesis is presented through eight chapters. The present chapter introduces the context of the research, outlining research aims and objectives. Chapter 2 introduces the research methodologies used in this project. Chapter 3 presents the numerical modeling approach used for the mechanical analysis of the studied slope. Chapter 4 summarizes the fieldwork, analysis and results obtain for the left slope of the Ridnaun Valley. Chapter 5 summarizes the geomechanical data acquired and evaluated through field surveys and laboratory tests. Chapter 6 investigates using numerical modeling techniques (FEM and hybrid FEM/DEM codes) key stages of fracture nucleation and propagation governing progressive failure process along the slope.

The final chapter concludes the research and main findings with recommendation for further work.

Chapter 4 and 6 are written in journal paper format, because they will be submitted shortly after the defense on Geomorphology (chapter 4) and Engineering Geology (chapter 6).

In addition, a CD – rom is enclosed, containing:

- Digital copy of this thesis
- Models database
- Video files of specific simulations presented within the thesis.



# 2. Methods and Materials

## 2.1 Introduction

The methodology used in this project can be subdivided into i) methodologies for geological and geomorphological characterization; ii) methodologies for geomechanical characterization and laboratory methods. A review of numerical modelling techniques used in this research project will be the main topic of chapter three.

## 2.2 Geological and geomorphological characterization

Field stations were the basic units of the field geological, geomorphological and geomechanical mapping. Each outcrop, as well as each geomechanical station, has associated to it UTM coordinates obtained from a Garmin GPS (Garmin Etrex Vista-HC; typical accuracy between 1-3 meters). Each available outcrop was mapped and a detailed description of lithology, structure and rock mass were obtained at each outcrop along with an estimate of the quality of the outcrop.

### 2.2.1 Topographic base map

Topographic maps used for geological, geomorphological and geomechanical mapping at 1:10000 scale, are the sections 14110, 14120, 15110, 15120 of the “Carta Tecnica Provinciale” of the Autonomous Province of Bolzano. The data are available for free from the website of the Informatic Department of the Autonomous Province of Bolzano.

The study area is covered by the “Foglio 04 – Merano” of the Geological map of Italy, at scale 1:100000 (Servizio Geologico D’Italia, 1971). In addition, as reference for geological survey, the up-to-date geological map of the area proposed by Frizzo (2002) was used.

### 2.2.2 Aribone Laser Scanner – High Resolution Digital Elevation Model (ALS-HRDEM)

In the last ten years the use of HRDEM for rock slopes analysis (geomorphic analysis, landslide detection and characterization, discontinuities and fracture analysis, deforming volumes definitions) has steadily increase (Derron and Jaboyedoff, 2010, Oppikofer et al., 2011; Pedrazzini et al., 2011; Jaboyedoff et al., 2012). The main advantages of using HRDEM for DSGSD analysis (Oppikofer et al., 2011; Pedrazzini et al., 2011; Jaboyedoff et al., 2008, 2012) are i) a better detection of the typical morphological structures and geometries (i.e. scarps and counterscarps, mobilized material, slope geometry) through shaded relief images and ii) a detailed analysis of inaccessible areas. In our study, the use of ALS



derived HRDEM was of fundamental importance in the detection of all the geomorphic features involving the slope, all the regional and local structural features, and the creation of detailed topographical profiles for a complete analysis of the slope morphologies.

In specific, High Resolution Digital Elevation Model (HRDEM, resolution: 2m) obtained from Airborne Laser Scanning (ALS) (2006 LiDAR surveys made by the Autonomous Province of Bolzano), was used (Fig.2.1). This data were acquired and processed under the UTM geographic coordinate system with the global reference system WGS84, in the European implementation define as European Terrestrial Reference Frame 1989 (ERTF89). As for the topography, ascii file of ALS-HRDEM are available for free from the web-site of the Informatics Department of the Autonomous Province of Bolzano.

### *2.2.3 Aerial photos and orthophotos interpretation*

Beside ALS-HRDEM, digital orthophotos provide an excellent resource for large-scale mapping. Orthophotos of 1999 and 2006 were used in this work.

Thanks to the courtesy of the Geological Department of the Autonomous Province of Bolzano that kindly provided the data, georeferenced digital aerial photos were used especially for geomorphological analysis. The images are related to specific acquisition flights, and are:

- Images relative to the so called “Volo GAI”, acquired between 1954-1955;
- Images acquired between 1975-1970;
- Images acquired between 1982-1985;
- Images acquired between 1992-1997;

### *2.2.4 Faults mapping*

Attitude (dip and dip direction), persistence, thickness of the fault gouge, as well as the thickness of the damage zone, possible block size variation within the core and the fault zone, and, where possible, surface roughness were recorded to characterize both fault planes and damage zones.

Besides field detection and characterization, fault detection and fault length estimation was possible also from air photographs, ortophotos and ALS-HRDEM (paragraphs 2.2.2 and 2.2.4) when visible.

### *2.2.5 Structural analysis*

Mesostructural analysis was used to measure and detect relevant structural elements such as regional, inherited ductile framework and main brittle features, such as joints and faults, on

rock outcrops situated along the studied slope. Measurements of the orientation of foliation, axial plane foliations, and crenulation cleavages were collected on each mapped outcrop.

Micro-structural analysis was carried out using an optical microscope oriented thin sections of selected samples. Petrographical and microstructural description of thin sections for the various lithological units mapped on the study slope was performed by means of standard techniques (Passchier and Trouw, 2005). In fact, the different properties of the units measured and evaluated in the field and laboratory, along with the mechanical behavior of the rock units, are related to their microstructural setting (see chapter 5, 6, 7). Thin section description for each site is included in chapter 6.

All the structural data were fundamental for the definition of the brittle-ductile setting of the metamorphic units defining the study slope, as well as the relationship between the ductile setting, metamorphic anisotropy of the rock mass and the gravitational-induced geomorphic features.

### **2.3 Geomechanical characterization**

Geomechanical surveys were carried out in order to collect information about the physical and mechanical properties of the rock mass and discontinuity sets required by the numerical modeling. Data were acquired by field survey and measurements, empirical correlation (Willye and Mahr, 2005; Barton and Choubey, 1997; Hoek and Brown, 1980; Hoek and Karzulovic, 2000; Hoek, 2006; Hoek and Diederichs, 2006; Barton and Pandey, 2011) and by means of laboratory tests (see paragraph 2.4). Geomechanical surveys were performed throughout scanline- type station and so called “random-type stations. Location of geomechanical stations was controlled mainly by the accessibility at each site, but efforts were made to ensure that the studied area and the structures of interest were covered homogeneously. At each station, both scanline and random, a description of the lithology, structure and rock mass were obtained along with an estimate of the quality of the outcrops. In addition, where possible, discontinuity analysis and Schmidt hammer measurements and rock samples were collected.

Scanline stations were executed to systematically characterize the discontinuities sets providing the fundamental mechanical parameters of rock mass, such as orientation, persistence, spacing and termination of the discontinuities, as well as Joint wall Compressive Strength (JCS) and Joint Roughness Coefficient, (JRC) (Willye and Mahr, 2005).

The attitude of each discontinuity plane was recorded as a dip and dip direction using a Burton compass. When possible, for each discontinuity plane the roughness, persistence and the spacing were recorded. In specific, to evaluate the roughness on the joint planes, Joint

Roughness Coefficient (JRC) was estimated by comparing the appearance of a discontinuity surface with standard profiles published by Barton and Choubey (1977) (Fig.2.2).

Scanline station typically covered outcrops that have extensions of at least 5 meters. The number of discontinuities mapped on each station was variable, ranging from 24 to 101. Locally, even scalines shorter than 5 m were performed due to the low extension of the outcrops in some areas of the slope.

“Random”-type station is defined the station in which, due to the really low extend of the outcrop (about 1 m in radius), no tape measure was used and the discontinuity were mapped in a non-systematic way. Normally, random type stations were performed on high altitude on the slope, and in area not easily accessible.

Unfortunately, not all the areas were covered with geomechanical stations. In fact, due to the presence of quaternary cover, the rock avalanche crown area do not show any useful outcrop for both scanline-type or random-type station.

Rock Quality Designation index (RDQ; Deere and Miller, 1966), Rock Mass Rating (RMR; Bieniawski, 1976), and the Q index (Barton, 1974, 2002) for rock mass classification were evaluated for each geomechanical station. Average values of RMR rate and Q index made possible to obtain, through empirical correlation (Hoek and Brown, 1980; Bieniawski 1989; Barton, 2002) geomechanical properties of the rock mass, such as rock mass Young modulus, rock mass cohesion and rock mass friction angle, fundamental for a complete characterization of the rock mass and for further numerical simulations (see chapter 5).

The Joint Wall Compressive Strength (JCS) of the recognized joint sets was measured directly on the field thank to the used of the electronic “SilverSchmidt” Schmidt Hammer (see paragraph 2.3.2; Proceq, 2010).

### *2.3.1 Electronic “SilverSchmidt” Schmidt hammer*

Schmidt Hammer, also known as Swiss hammer or a rebound hammer, is a device used to measure the strength properties of concrete or rock (Fig.2.3). It was used first to test rock hardness and strength by Deere and Miller (1966). The rebound of a spring-loaded mass impacting against the tested surface is measured by the hammer, with an impact force that is known. The measured rebound is dependent on the hardness of the testes material. Using common Schmidt hammers, the average rebound values, called “R”, can be then correlated to the unconfined compressive strength (UCS) of the intact rock. In fact, empirical correlation exist between R and UCS which are specific to the rock lithology and weathering conditions (Kahraman, 2001; Dincer et al., 2004; Tansi et al., 2000; Greco and Sorriso-Valvo, 2005). However, traditional hammers suffer from the following limits:

- Time consuming data collection.
- The rebound value is strictly dependent on the impact direction.
- The rebound value is affected by internal friction.
- Limited tightness of sealing causes premature loss of accuracy

Thus, for this work a new type of Schmidt Hammer was used, the “Silverschmidt” Schmidt hammer was used (Proceq, 2010) (Fig. 2.3). More in detail, the Silverschmidt Silver-PC N-type hammer was used. This electronic device overcomes all the issues that traditional hammers show.

Differently from the “R” value acquired by traditional hammers, the test hammer SilverSchmidt acquires the "Q"-value by measuring the velocity of impact and of rebound immediately before and after the impact. Thus, the rebound value requires no angular correction (Proceq, 2010).

In addition, a large number of measurements points can be collected and automatically stored and evaluated, according to statistical criteria, by the device. Beside the stored “Q” value of each measure, mean UCS value of a data acquisition set related to the tested discontinuity is automatically given by the device.

Given all its characteristics, along with the intuitive user interface and the low weight, make the Silverschmidt a very powerful tool for rock strength properties analysis.

### 2.3.2 *RocLab*

RocLab (2002) is freeware software for determining rock mass strength parameters, based on the latest version of the generalized Hoek-Brown failure criterion and Mohr – Coulomb failure criterion. The input parameters required are UCS, GSI and the intact rock parameter  $m_i$  which derives from triaxial tests. Tables of typical  $m_i$  values for various lithologies are included in the software. Outputs from RocLab were used as input parameters for the numerical simulation (see chapter 5 and 6).

### 2.3.3 *Dips*

Dips is a software package developed by Rocscience (2010) that allows the user to analyze and visualize structural data following the same techniques used in manual stereonet. In addition, dips allows contouring of the structural data and provides a statistical analysis of user defined discontinuity sets. Standard kinematic analysis for planar and toppling failure mechanism incorporated recorded discontinuity sets were performed (Willye and Mahr, 2005).

### 2.3.4 Geological Strength Index (GSI)

For each mapped outcrop during the field work, a value of the Geological Strength Index (GSI) was evaluated and assigned. The GSI, introduced by Hoek (1994), Marinos and Hoek (2000), provides a system for estimating the reduction in rock mass strength for different geological conditions as identified by field observations (Hoek et al., 1998). Rock mass strength is assigned by ready field observations of the rock mass structure and the conditions of fractures planes, in terms of roughness and alteration (Hoek et al., 1998; Marinos and Hoek, 2000). The combination of these two parameters allows the estimation of GSI values by mean of contours given by the GSI tables proposed by Hoek (1994), Hoek et al. (1998), Marinos and Hoek (2000) (Fig. 2.4). In specific, for this work the updated version of the GSI table proposed by Marinos and Hoek (2000), which accommodates the effect of schistosity and shear planes, was used. A GIS-based contour map of the GSI values, using ArcGis 9.3, assigned to all mapped outcrops was then created to evaluate the spatial distribution and possible variability of the values.

### 2.3.5 Rock quality designation index (RQD)

The rock quality designation index (RQD) is a standard parameter in drilled core logging (Deere, 1963). It has defined as the percentage of intact rock pieces longer than 100 mm to the total length of the core. RQD values are useful, as starting parameters, to evaluate outcrop quality, and it can be calculated by (Deere, 1963):

$$RQD = \frac{\sum L_c}{L_t} * 100 \text{ eq. 2.1}$$

Where  $L_c$  is the sum of length of core pieces longer than 100 mm and  $L_t$  is the total length of the core. However this equation is applicably only for outcrops having number of fractures per cubic meter of volume ( $J_v$ ) lower than 35. If value of  $J_v$  are higher than 35, other relation can be used. In this thesis work, the following equations were used:

$$RQD = 110 - 2,5 J_v \text{ eq. 2.2 (Palmström, 2005)}$$

$$RQD = (100e^{-N\lambda}) * (N\lambda + 1) \text{ eq. 2.3 (Priest and Hudson, 1981).}$$

Where  $\lambda$  is the discontinuity frequency and  $N$  is the length of the line.

### 2.3.6 Rock Mass Rating (RMR)

The rock mass rating (RMR) classification, developed by Bieniawski (1976), has become a standard classification system used in rock mass characterization. The rock mass is classified thank to the definition of a numerical index which correspond to a class of rock mass quality. The rock mass is classified into five classes as follows:

<b>RMR</b>	100 – 81	80 – 61	60 – 41	40 – 21	≤ 20
<b>Class</b>	I	II	III	IV	V
<b>Description</b>	Very good	Good	Fair	Poor	Very poor

The  $RMR_b$  proposed by Bieniawski (1976) can be calculated starting from five coefficients:

$$RMR_b = A1 + A2 + A3 + A4 + A5 \quad \text{eq. 2.4}$$

Where  $A1$  is a coefficient depending on  $\sigma_c$  value ,  $A2$  is related to the RQD value,  $A3$  is an index related to the joint spacing, whereas  $A4$  depends on the joint condition and  $A5$  is dependent to the rock conditions.

Romana (1985, 1993, 1995) modified the original formulation in order to make it more suitable also for slopes problems, adding a new parameter  $A6$  changing the RMR formulation as follows:

$$RMR_c = A1 + A2 + A3 + A4 + A5 + A6 \quad \text{eq. 2.5}$$

RMR classification system allows the evaluation of rock mass strength parameters like  $c$  and  $\varphi$  as follows:

$$c = 5 * RMR_b \quad \text{eq. 2.6}$$

$$\varphi = 0.5 * RMR_b + 5 \quad \text{eq. 2.7}$$

Beside rock mass strength parameters, Bieniawski (1978) proposed a relation for the evaluation of rock mass deformation modulus:

$$E_d = 2 * RMR_b - 100 \quad \text{eq. 2.8}$$

Serafim and Pereira (1983) stated that equation XX is valid for  $RMR_b$  values higher than 50. For lower values, they proposed the following equation:

$$E_d = 10\left(\frac{RMR_b - 10}{40}\right) \text{ eq. 2.8}$$

$$E_d = 0.87e^{0.0455 * RMR_b} \text{ eq. 2.9}$$

### 2.3.7 Slope Mass Rating (SRM)

The slope mass rating (SRM) classification system, introduced by Romana (1985), derives from the Bieniawski RMR. In fact, SRM can be calculating subtracting several parameters (F1, F2, F3, F4) related to the joint – slope relationships and the method of excavation. SRM introduces four adjusting factors which allow a simple estimation of RMR correction factors:

$$SMR = RMR_b - |(F1 * F2 * F3)| + F4 \text{ eq. 2.10}$$

## 2.4 Laboratory techniques

A series of laboratory tests were performed with the aim of constraining the physical and mechanical properties of the rock mass. Results of these tests were used as input parameters for the subsequent numerical modelling (see chapter 5).

### 2.4.1 Point load test

Point load test apparatus is shown in figure 2.5. Tests were conduct according to the International Society for Rock Mechanics (ISRMS, 1985). In these tests, rock specimens (cylindrical, prismatic or irregular) are loaded between two conical platens (of stipulated geometry and hardness), and fail by the development of one or more extensional planes containing the line of loading. These failure modes are referred as valid failure modes, whereas deviations from these failure patterns are consider to be invalid by standards like ISRM and ASTM (ISRM, 1985; ASTM, 2001; Basu and Kamran, 2010). Standards stated that point load strength determined from a point load tests that has led to invalid failure mode should be rejected (Basu and Kamran, 2010). This is applicable for isotropic rocks, in which invalid failure is controlled by some preferential cracks not representative of the whole rock material. In case of anisotropic rocks, in which foliation/planes of weakness control the mechanical behavior of the rock and the failure modes, the ISRM and ASTM standards do not accommodate the validity of failure in such rock types. Basu and Kamran (2010) suggests to reconsider in the standards the stipulations about failure modes and feasibility of their acceptance Indeed, for anisotropic rocks in the existing standardized point load methods.

The point load index, corrected for the size factor  $Is_{50}$ , was calculated using the following equations (Basu and Kamran, 2010):

$$Is_{50} = F \times \frac{P}{De^2} \quad (\text{Eq. 2.11})$$

$$F = \sqrt{\frac{De}{50}} \quad (\text{Eq. 2.12})$$

$$De^2 = 4A/\pi \quad (\text{Eq. 2.13})$$

$$A = W \times D \quad (\text{Eq. 2.14})$$

Where  $F$  is the size correction factor,  $Is$  is the uncorrected point load strength,  $De$  is the equivalent core diameter,  $P$  is the applied load,  $A$  the minimum cross sectional area of a plane through the platen contact points.  $W$  and  $D$  are block dimensions.

To calculate the UCS values starting from Point load index, the relation proposed by Basu and Kamran (2010) was used:

$$UCS = 11.103 Is_{50} + 37.659 \quad (\text{Eq. 2.15})$$

This equation was used because in our opinion it represents the best correlation so far when dealing with anisotropic rocks. In fact, to evaluate the strength anisotropy of the metamorphic units, tests were performed both perpendicular and parallel to the foliation.

To quantify the strength anisotropy of the tested rock samples, an isotropic index was then measured on the basis of the one proposed by Brideau (2002):  $Is_{50\text{perpendicular}} / Is_{50\text{parallel}}$ .

#### 2.4.2 Uniaxial and Triaxial compressive tests

Uniaxial and triaxial tests were performed at the Rock Mechanics Laboratory at the Department of Geosciences of the University of Padova. The lab is equipped with the automatic system ADVANTEST9 and SERCOMP7, which are developed, produced and sell by Controls-Italia s.r.l. (Fig.2.6).

ADVANTEST9 is a servo-hydraulic command system, which controls the vertical applied load, and it was the apparatus used for Uniaxial Compressive Tests. For triaxial tests, SERCOMP7 system was used along with ADVANTEST9. In fact, SERCOMP7 system allows the application of confining pressure during the test, by mean of Hoek cell. The apparatus consists of a control console containing a high pressure pump with piloted valves for the automatic control of the load gradient from values close to zero up to the maximum oil delivery of the pump. Both uniaxial and triaxial tests were conduct on the Controls 50-C5800 compression testing frame.



In all experiments, vertical load is applied after a pre-load of about 9 MPa, imposed automatically by the system itself. The machines is certified according to the UNI EN 12390-4, ASTM C39 and AASHTO T22 standard procedures.

Experiments were performed on cylindrical samples having a diameter of about 38mm and a length-to-diameter ratio between 2.0 and 2.5 according to the ASTM-D7012 (2010) and ASTM-D4543 (2008) specifications. Young's Modulus and Poisson's ratios were derived from the tests thanks to the use of two linear electrical strain gauges (TML), bonded along the axial and horizontal direction of the specimen.

Considering first Uniaxial compressive Strength (UCS hereafter), the shape effect of cylinder sample on UCS values is still debated (e.g., Tuncay and Hasancebi, 2009), and the equations suggested to correct the results for L7D ratios are not applicable to every rock-type (Hoek and Brown, 1980; Hawkins, 1998; Tuncay and Hasancebi, 2009). According to Hawkins (1998), maximum strength can be obtained on samples having a diameter ranging from 38 to 54 mm.

For UCS, samples were loaded at a constant rate of 0.300 MPa/s, to reach failure in a test time interval between 2 and 15 minutes, following the guidelines of ASTM-D7012 (2010).

Triaxial tests were performed with both ADVANTEST9 and SERCOMP7 systems, with a 3000 kN oil press capacity. Experiments were performed at constant velocity of 1.0  $\mu\text{m/s}$  controlled by three vertical Linear Velocity Displacement Transducers (LVDT, Solartron; maximum displacement: 10 mm. The confined tests were performed following the ASTM-D7012 method (2010).

Confining pressure was applied through a Hoek cell (Fig. 2.7). This lasts, developed by Hoek and Franklin (1968) is widely used for testing cylindrical rock specimens under triaxial compression. The maximum pressure that the cell can manage is around 70-80 MPa. All the triaxial tests were performed under controlled displacement to avoid explosive fracture of the sample and possible damage to the Hoek cell.







According to Wittke (1990), Jager and Cook (2007), tests were performed with a loading direction parallel, perpendicular and with an angle of 30° to the metamorphic fabric. Using this approach, anisotropy-induced strength variation can be measured.

Figures



Figure 2.1: *Shaded relief image of ALS – HRDEM*



		SURFACE CONDITIONS				
		VERY GOOD	GOOD	FAIR	POOR	VERY POOR
<b>STRUCTURE</b>		DECREASING SURFACE QUALITY →				
	INTACT OR MASSIVE - intact rock specimens or massive in situ rock with few widely spaced discontinuities	90			N/A	N/A
	BLOCKY - well interlocked undisturbed rock mass consisting of cubical blocks formed by three intersecting discontinuity sets	80	70			
	VERY BLOCKY- interlocked, partially disturbed mass with multi-faceted angular blocks formed by 4 or more joint sets		60	50		
	BLOCKY/DISTURBED/SEAMY - folded with angular blocks formed by many intersecting discontinuity sets. Persistence of bedding planes or schistosity			40	30	
	DISINTEGRATED - poorly interlocked, heavily broken rock mass with mixture of angular and rounded rock pieces				20	
	LAMINATED/SHEARED - Lack of blockiness due to close spacing of weak schistosity or shear planes	N/A	N/A			10

↑ DECREASING INTERLOCKING OF ROCK PIECES ↓

Figure 2.4: GSI table proposed by Marinos and Hoek (2000).





Figure 2.5: example of a point load test apparatus.



Figure 2.6: the automatic system ADVANTEST9 and SERCOMP7, available at the Rock Mechanics lab of the Geosciences department of the University of Padova (developed, produced and sold by Controls-Italia s.r.l.).

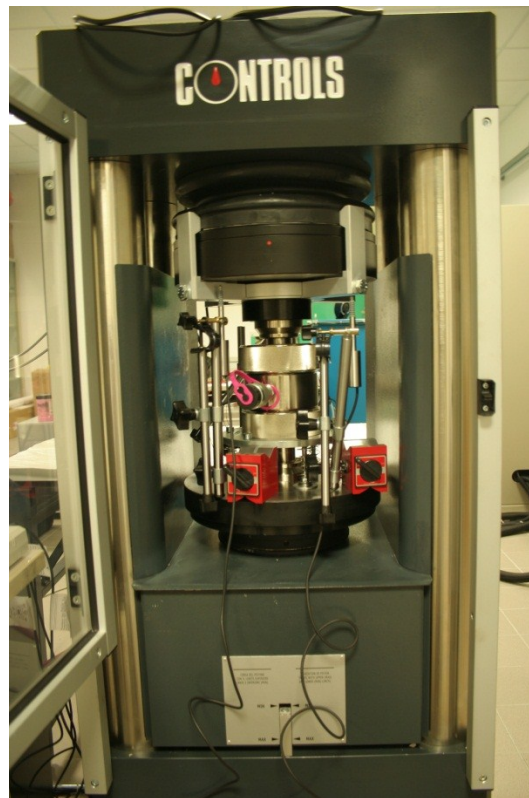


Figure 2.7: Hoek cell used for triaxial tests.



# **3. Numerical modelling techniques for progressive rock slope failure simulation.**

## **3.1 Introduction**

This chapter reviews some numerical models for stress analysis and progressive rock slope failure simulation. The aim is to present the basic concepts of the principal numerical models used in this thesis to simulate the mechanical behaviour of rock masses, with a particular attention on numerical modelling of fractured rock masses. The review does not include a detailed dissertation of mathematical formulations for each numerical method, but presents the assumptions made in the different methods.

## **3.2 Numerical methods for rock mechanics problems**

Numerical modelling of rock slopes is now used routinely in the civil and mining engineering sectors as well as academic research (Stead et al., 2006; Elmo, 2006). Nowadays, limit equilibrium methods still remain the most common adopted method in surface rock engineering although major rock slope instabilities often involve complex internal deformation and fracturing. This is in contrast with rigid block assumptions adopted in most limit equilibrium back-analyses. Creep, progressive deformation and extensive internal rupture of slope mass (brittle/plastic damage) are the main controlling factors for slope failures. Thus, numerical modelling methods incorporating intact rock deformation (strain), are needed to attempt to simulate and investigate the mechanical response of a rock mass subject to a set of initial conditions such as in situ stresses and water levels, boundary conditions and induced changes on the slopes such as erosion, excavation and seismic shakings.

A detailed and comprehensive review of state of the art numerical modelling techniques for rock mechanics and rock engineering in general was provided by Jing and Hudson (2002) and Jing (2003).

Any complex model conceptualisation should try and reflect the inherent Discontinuous, Inhomogeneous, Anisotropic, and Not-Elastic nature of the rock mass (DIANE concept, after Harrison and Hudson, 2000), including all the features that are deemed necessary for the purpose. In relation to the intrinsic discontinuous nature of rock masses, the numerical



models should also incorporate a characterization of pre-existing fractures, as well as fractures induced by changes in the original state of stress. Parameter representability associated with sample size, representative elemental volume and homogenisation/upscaling represent fundamental problems associated with modelling. For this reason, any modelling and subsequent rock engineering design will have to include some form of subjective judgements (Jing, 2003).

Numerical modelling is essential for the investigation of the fundamental processes occurring in rocks and for rock engineering design. Two main approaches are used for the numerical modelling of fractured rock masses, based on the concept that the deformation of a rock mass subjected to applied external loads can be considered as being either continuous or discontinuous. The main differences between the continuum and discontinuum analysis techniques lie in the conceptualisation and modelling of the fractured rock mass and the subsequent deformation that can take place in it.

Conventionally, numerical modelling approaches may be subdivided into:

- Continuum methods: Boundary Element Method (BEM), Finite Element Method (FEM) and Finite Difference Method (FDM).
- Discontinuum methods: Discrete Elements Method (DEM), Discontinuous Deformation Analysis (DDA) and Discrete Fracture Network Method (DFN).
- Hybrid models: Hybrid BEM/DEM, Hybrid FEM/BEM, Hybrid FEM/DEM and other hybrid models.

When considering a given rock mechanics problem, some regions of the rock mass could be treated as continuous, whilst discontinuum analysis would explicitly apply to other elements like discontinuities. A continuum model would reflect mainly material deformation of the system, whereas a discontinuum model would reflect the component movement of the system (Elmo,2006). Based on these observations, the most common types of numerical models that have found application in the solving of rock mechanics problems can be grouped as follows:

- Continuum methods: Boundary Element Method (BEM), Finite Element Method (FEM) and Finite Difference Method (FDM).
- Discontinuum methods: Discrete Elements Method (DEM), Discontinuous Deformation Analysis (DDA) and Discrete Fracture Network Method (DFN).
- Hybrid models: Hybrid BEM/DEM, Hybrid FEM/BEM, Hybrid FEM/DEM and other hybrid models.

In this research project continuum methods and hybrid models were used. Indeed, the following sections review the basic concepts of continuum and hybrid methods used.

### 3.3 Hybrid elasto – plastic finite element method: Phase2

The proprietary Phase<sup>2</sup> (Rocscience, 2008) is a typical example of FEM program for stress analysis simulations. The code Phase<sup>2</sup> is a two - dimensional elasto-plastic finite element stress analysis program, based upon a hybrid finite/boundary element method (FEM/BEM). The hybrid FEM/BEM programming permits Phase<sup>2</sup> to model multiple materials and simulate non – linear behaviour close to the excavation boundaries, whereas a – field in – situ stresses are modelled via a boundary method (Hoek et al., 1998; Styles, 2009). The FEM composition of Phase<sup>2</sup> models allows to simulate progressive failure/post – failure behaviour of the rock mass (Rocscience, 2008).

Due to the FEM continuum – based approach, the consideration of discontinuity – controlled failures is limited, and the simulation of direct displacements cannot be simulated upon these. One of the major features of Phase<sup>2</sup> is finite element slope stability analysis using the shear strength reduction method. This option is fully automated and can be used with either Mohr-Coulomb or Hoek-Brown strength parameters. Shear strength reduction (SSR) method make Phase<sup>2</sup> able to analyze mass – controlled shear failure.

The SSR is simple in concept: systematically reduce the shear strength envelope of material by a factor of safety, and compute FEM models of the slope until deformations are unacceptably larger of solution do not converge (Hammah et al., 2005). Indeed, SSR techniques allows the evaluation of the critical Strength Reduction Factor (SRF), which can be consider an equivalent to the Factor of Safety (FOS), representing in fact the amount by which the mass strength must be reduced to result in failure. For Mohr – Coulomb material this procedure is defined by the following equation (Styles, 2009):

$$\frac{\tau_{mass}}{F} = \frac{c_{mass}}{F} + \frac{\tan\phi_{mass}}{F} \quad \text{eq. 3.1}$$

Where  $\tau$ ,  $\phi$  and  $c$  are the shear, frictional and cohesive mass strength;  $f$  is the SRF by which the Mohr – Coulomb strength components are reduced by to obtain a shear strength reduction. The main advantage in using the SSR method is that this method eliminated the need for the calculation of the FOS using a model that is based on a specific type of slope failure such as wedge, planar, toppling or circular. In addition, no assumptions are required on the location and shape of the failure surface. Indeed, no a priori assumptions on the failure mechanisms are required, especially when using the SSR to back analyse a slope failure. This is an advantage over some kinematic and limit equilibrium approaches which require the characterization of the failure mechanisms prior to modeling. Due to the ability of the technique to show progressive reduction in strength of the rock mass, it can capture progressive failure (Diederichs et al., 2007). An issue in SSR techniques is the fact that SFR

considers a simultaneous downgrade of both  $c$  and  $\tan\phi$ , whereas Hajiabdolmajid (2002), Diederichs (2007) and Diederichs et al. (2007) state that independent downgrade could be important as cohesion has more variability than frictional strength.

The ability of SSR approach in modeling progressive failure is clear when considering the method in an excavation application (Styles, 2009). In fact, once the last excavation slice is removed, shear strain can develop marking the location of either a continuous potential failure plane or widespread disruption of rock mass.

### **3.4 Modeling brittle fracture of rocks**

Considering for simplicity small scale fractures, three modes of displacement can occur at the crack tip. All of these eventually result in fracture propagation and, thus, considered as modes of fracture propagation (Brideau, 2002; Elmo, 2006; Styles, 2009). On the basis of relative movement between the fracture surfaces, fracture modes can be divided as follow (Fig. 3.1):

- Mode I: extension/opening of crack tips, with movements perpendicular to the fracture surfaces, caused by tensile forces;
- Mode II: in – plane shear stress causes a sliding movement (shear) parallel to the fracture surfaces;
- Mode III: anti – plane shear causes movements both parallel to the fracture front and parallel to the fracture surfaces.

Mix modes of fracturing can occur, entailing displacement that can be both parallel and perpendicular to the fracture surface. As stated by Whittaker et al. (1992), fracturing of rock is defined by both opening and shear, resulting in a mixed mode I – II fracture.

In a modelling perspective, brittle failure corresponds to a transition from a continuum to a discontinuum state, which is extremely difficult to capture in current numerical models despite the advances in discontinuum modelling.

Following work by Martin and Chandler (1994), the attention of investigators has turned to an approach based on the concept that in brittle failure peak cohesion and friction are not mobilised together and most of the cohesion is lost before peak friction is mobilised.

Several authors (Hajiabdolmajid et al., 2002; Fang and Harrison, 2002; Martin et al., 2001) adopted a “cohesion weakening and friction strengthening” (CWFS), with local degradation approach to model and predict brittle failure of rock. The utilisation of a continuum approach to modelling a process that is ultimately discontinuum has intrinsic limitations and cannot capture all the subtleties of brittle failure (Elmo, 2006).

Diederichs (1999 and 2002) using a DEM approach demonstrated how the brittle response resulting in compression spalling can be the result of purely mode I (tensile) crack initiation

and growth. As a consequence, under low confinement, extensile crack growth and mode I crack opening removes the possibility for frictional resistance between the crack surfaces. As a result, cohesive strength is lost before frictional strength can be mobilised.

Neither continuum nor discontinuum models approach could alone capture the interaction of existing discontinuities and the creation of new fractures through fracturing of the intact rock material (Stead et al., 2004; Coggan and Stead, 2005). As reported by several authors (e.g. Pariseau, 1993; Hart, 1992; Owen et al., 2004b), the introduction of a hybrid continuum/discontinuum approach, linking different numerical techniques such as FEM and DEM, could allow for large scale analysis and locally large displacements along fracture planes. A hybrid approach can also provide a better description of the physical processes involved, accounting for diverse geometric shapes and effective handling of large numbers of contact entities with specific interaction laws. The implementation of specific fracture criteria and propagation mechanisms allows the simulation of the progressive fracture process within both the finite and discrete elements. Consequently there are significant advantages in employing combined FEM/DEM solution strategies to model discrete/discontinuous systems.

The objective of a hybrid method is to combine the above methods in order to eliminate undesirable characteristics while retaining as many advantages as possible (Hoek, 2000; Elmo, 2006). Hybrid methods allow the harmonization of the geometry of the required problem resolution with the numerical techniques available, therefore providing an effective representation of the effects of the far-field to the near-field rocks (Jing, 2003; Elmo, 2006). The application of a hybrid FEM/DEM numerical method combines the advantages from both discontinuum techniques and continuum approaches (Stead et al., 2004; Elmo, 2006; Styles, 2009). In this way it is possible the modelling of intact behaviour, interaction along existing discontinuities and the initiation and development of new fractures through consideration of principle of fracture mechanics (Stead et al., 2006; Stead and Coggan, 2012).

The proprietary code ELFEN (Rockfield, 2005) provides a good example of hybrid FEM/DEM model that has recently found increasing use in rock mechanics (Coggan et al., 2003; Cai and Kaiser, 2004; Klerck, 2000, 2004; Owen et al., 2000, 2001; Eberhardt et al., 2004; Elmo et al., 2005; Coggan and Stead, 2005, Styles, 2009; Stead and Coggan, 2012).

### **3.5 Hybrid FEM/DEM model – ELFEN code (Rockfield)**

The ELFEN code is a hybrid 2D/3D numerical modelling package, incorporating both Finite Element (FE) and Discrete Element (DE) analysis, and specifically designed for application to complex non-linear finite element simulations. The code ELFEN allows the simulation of crack growth, accumulation and coalescence, thus enabling the investigation of the interaction

between newly generated and pre-existing fractures, capturing the subsequent displacement and/or rotation of independent blocks in a typical DEM fashion (Elmo, 2006).

The adaptive remeshing scheme and contact search algorithms in ELFEN, allows the simulation of brittle fracture initiation and propagation through the finite element mesh (Eberhardt, 2004; Stead et al., 2006; Elmo, 2006; Styles, 2009). In ELFEN, the fracturing process can propagate through elements (intra – element fracturing) or along element boundaries (inter – element fracturing).

The most important and so far quite unique capability of ELFEN is the ability to simulate the transition of a rock from continuum to discontinuum state (Cai and Kaiser, 2004; Elmo, 2006; Styles, 2009). In fact, FEM component of ELFEN is used until yielding condition are met, and the stress state within the material succeeds the fracture criterion. As a result, crack initiate through the DEM aspect of ELFEN. Thus, the intact joint bounded block is represent by a finite – element mesh, whereas the joint behaviour is modelled using a discrete - element mesh.

With such capability, ELFEN allows the investigation of the behaviour within a rock slope prior to and during the failure, simulating fracturing, damage and associated softening of the material (Stead et al., 2006; Styles, 2009).

ELFEN allows the investigation of rock slope failure mechanisms using a “total rock slope failure” approach (Stead and Coggan, 2006), that means the possibility to simulate a rock slope failure from initiation through transportation to deposition. To do that, detailed and relevant data collection both surface and subsurface, are required in order to constrain the results.

ELFEN code is able to model fracture propagation only through mode I fracturing. To overcome this issue, the application of the combined “Mohr – Coulomb with Rankine tensile cut – off” failure criteria allows the simulation of both mode I and II fracturing.

The Mohr – Rankine criterion is one of the elasto – plastic material models available within ELFEN. Rankine non - linear criterion allows the simulation of mode I fracture extension, whereas mode II yielding can be simulate through the Mohr – Coulomb non-linear criterion. For a specific detailed description of tensile fracture model (Rankine failure criterion) and for the Mohr – Coulomb material model implemented within ELFEN, see Elmo (2006).

The ELFEN compressive fracture model is based on the assumption that quasi – brittle fracture is extensional in nature. Thus, any yield surface is divided into regions in which extensional failure can be modelled directly (tensile stress field) and indirectly, in case of compressive stress field (Klerk et al., 2004; Elmo, 2006).

In addition, Mohr – Coulomb material model with Rankine cut – off in ELFEN is able to manage mobilised parameters with plastic strains (Hajiabdolmajiid et al., 2003) to numerically simulate the rock brittle response (Klerck et al., 2004; Elmo, 2006). Klerck (2000) presented several numerical examples to validate the use of mobilised material parameters that realise hardening/softening with respect to effective plastic strain in the context of the Mohr-Coulomb material model with Rankine cut-off.

The material properties assigned to the elements used in the ELFEN analysis are defined within the *material* data structure. Table 3.1 lists the material parameters that have to be specified for a Mohr-Coulomb with Rankine tensile cut-off type of analysis.

Appendix A contains the ELFEN neutral file, which contains an example of the definition of the material properties.

## Tables

Compulsory data	Optional data
Constant parameters specified using: <i>Elastic_properties</i> Young's modulus Poisson's ratio Density  Initial values specified using: <i>Plastic_properties</i>  Cohesion $c$ Friction angle $\phi$ Dilatancy angle $\psi$ Tensile strength $\sigma_t$ Fracture energy $G_f$	Hardening/softening specified using: <i>Hardening_properties</i>  Effective Plastic strain Cohesion $c$ Friction angle $\phi$ Dilation angle $\psi$

Table 3.1: Material properties that have to be specified as input parameters for a “Mohr – Coulomb – Rankine tensile cut – off” analysis (after Elmo, 2006).

## Figures

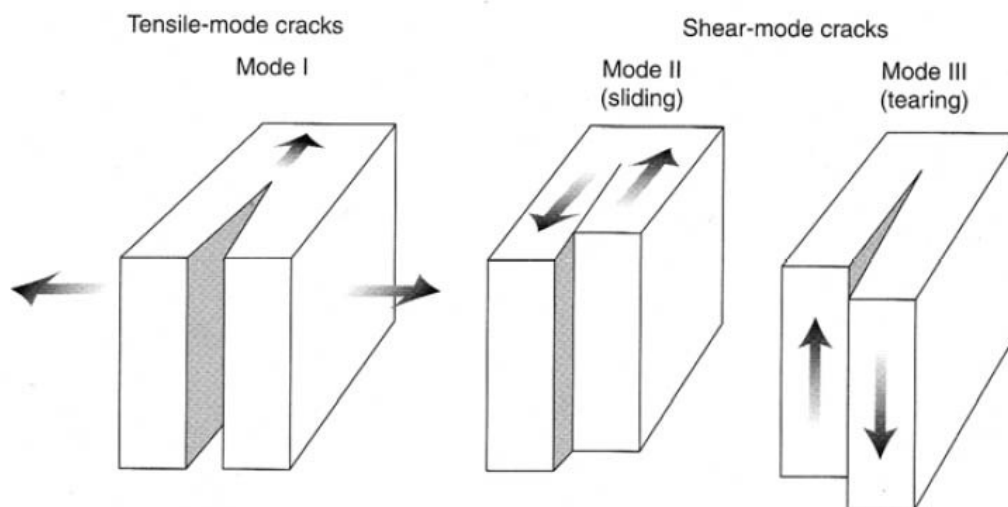


Figure 3.1: Modes of fracturing (after van der Pluijm and Marshak, 1997).

# 4. Inherited structures and slope evolution: the case of the left slope of the Ridnaun Valley

Luca Zorzi, Lorenzo Flaim, Matteo Massironi, Rinaldo Genevois, Douglas Stead

## 4.1 Introduction

Deep-Seated Gravitational Slope Deformations (DSGSD) affecting Valley walls are very common in the Alps, governing the evolution of mountain landscapes (Mortara and Sorzana, 1987; Crosta, 1996; Agliardi et al., 2001, 2009). DSGSDs are large mass movements on high-relief slopes that normally extend from near the valley floor to, or beyond, the ridge crest (Agliardi et al., 2012). The deformation mechanism related to these phenomena is commonly referred to as creep (Radbruch-Hall, 1978; Hutchinson, 1988), and is characterized by low to extremely low deformation rates (Cruden and Varnes, 1996; Agliardi et al., 2012). Common field indicators of these phenomena are surface deformational features such as double ridges, scarps and counterscarps (Agliardi et al., 2001, 2012). Retreat of Pleistocene glaciers that left behind unstable over-steepened slopes is to be considered as the main cause for the initiation of these phenomena (Nemcok and Pasek, 1969; Dramis, 1984; Augustinus, 1995; Dikau et al., 1996; Kellerer-Pirklbauer et al., 2010; Ambrosi and Crosta, 2011). Nevertheless, some alpine DSGSDs show evidence of activity covering more than one glacial circle, with clear evidence of reactivation after successive glaciations (Agliardi et al., 2012).

In addition, high relief, active tectonics and seismicity can be considered as genetic factors of deep-seated gravitational movements (Kinakin and Stead, 2005; Ambrosi and Crosta, 2011; Agliardi 2012). In the Italian Alps, DSGSDs are very common, and in the last decades several phenomena have been investigated in detail (Mortara and Sorzana, 1987; Crescenti et al., 1994; Agliardi et al., 2001, 2009, 2012; Bistacchi and Massironi, 2001; Massironi et al., 2003, 2010; Soldati et al., 2006; Ambrosi and Crosta, 2006; Ghirotti et al., 2011).

It is widely accepted that the DSGSDs evolution of a slope is strongly controlled by the structural setting of the bedrock. In particular, a close relationship between gravitational morphostructures and brittle tectonic features has been extensively demonstrated (Zischinsky, 1966, 1969; Nemcok, 1972; Radbruch – Hall, 1978; Savage and Varnes, 1987; Chigira, 1992; Dramis et al., 1994; Crosta, 1996; Agliardi et al. 2001). Few studies have investigated in detail and taken into account how, at the slope scale, the inherited ductile framework in



foliated metamorphic rocks affects slope stability (Massironi et al., 2003; Henderson et al., 2006; Brideau et al., 2009; Jaboyedoff et al., 2011; Oppikofer et al., 2011, Zorzi et al, under review – in attachment on this thesis).

The present chapter, making use of different approaches, such as geomorphology, structural geology and geomechanical analysis, evidence how the brittle/ductile tectonic setting is the primary controlling factors of large mass movements in poly-deformed foliated rock masses. The left slope of the Ridnaun Valley (eastern Alps, Italy Fig.1) was chosen as case study. In fact, the left slope of the Ridnaun Valley show evidences of a differential gravitational evolution, which is most likely controlled by is most likely controlled by the interaction between the ductile and brittle structures defining the slope.

In this chapter, a detailed geological, geomorphological and geomechanical description of the studied slope will be present, with the aim to investigate the role of brittle structures (faults and joint sets) and ductile setting (foliation at multiple scale, shear band cleavages, crenulation cleavages) on DSGSD.

## **4.2 Geological and geomorphological setting**

The E-W trending Ridnaun Valley is located in the northern sector of the South Tyrol Province (Italy), west of the town of Sterzing (Fig.4.1). The metamorphic rocks cropping out along the Ridnaun Valley belong to the basement units defining the eastern part of the Austroalpine realm (Sölva et al, 2005). They show a complex polymetamorphic history, in which four main tectono-metamorphic events have been distinguished (Thöni, 1999; Sassi et al., 2004; Sölva et al, 2005): i) a mainly magmatic event (610-420 Ma); ii) the Variscan Event (375-310 Ma); iii) the Permian-Triassic LP-event (290-220 Ma); iv) Alpine event, subdivided into the eo-Alpine sub-event (pressure peak et 105-9 Ma), the meso-Alpine sub-event (pressure peak at about 60-40 Ma) and the neo-Alpine sub-event (since 20 Ma). The Ridnaun Valley is located at the top of one of the most important geodynamic context of the Alps: the Schneeberg Normal Fault Zone (SNFZ). The SNFZ outcrops NW of Meran/Meran, in a tectonically complex area located W of the Southalpine belt. (Fig.4.1, Bestmann et al., 2011). In this Alpine area, the Austoalpine Nappe is defined by a stack of N-NW dipping complexes, namely from top to the bottom: i) Ötztal-Stubai (Variscan age), ii) Schneeberg/Monteneve (mainly Cretaceous age), iii) Texel (Cretaceous age) and iv) Campo-Ortler/Mauls- Penserjoch (Variscan age) (Thoni, 1999, Sassi et al., 2004; Schuster et al., 2001; Sölva et al, 2005). These rocks underwent a poly-phasic deformation history, which developed a 4.5 km thick extensional shear zone (SNFZ, Sölva et al, 2005). The SNFZ was interpreted to represent the hanging wall normal shear zone of an extruding wedge,

represented by the Cretaceous eclogite-facies rocks of the Textel Complex (Bestmann et al., 2011; Sölva et al, 2005). The exhumation of the high pressure Cretaceous rocks within the Variscan basement started around 95 Ma under high-pressure amphibolite facies (Konzett and Hoinkes, 1996; Sölva et al, 2005) and continued at low greenschists facies and under brittle condition at 76 Ma (Sölva et al, 2005). Among the several subunits defining the Austroalpine basement unit in this area, two of them crop out on the left slope of the Ridnaun Valley: the Ötztal-Stubai Complex and the Schneeberg/Monteneve Complex. The Ötztal-Stubai Complex is defined in this area by paragneisses intercalated with continuous levels of amphibolites, amphibolic gneisses and quartzites. Locally, discontinuous stratabound and stratiform Zn-PB mineralization, mainly made by sphalerite, pyrrhotite, galena and chalcopyrite can be found within the Ötztal-Stubai Complex (Brigo, 1965; Förster, 1963; Frizzo, 1976; Frizzo et al., 1982; Pagel, 1975). The Schneeberg/Monteneve Complex (SMU) consists mainly of garnet-micaschists, intercalated by discontinuous levels of quartzitic-micaschists, graphitic-micaschists, calc-silicate marbles and quartzites. These alternating layers are known as Bunte Serie (heterogeneous series; Mauracher, 1981; Sölva et al, 2005). In specific, the micaschists belonging to the SMU are medium to coarse grained, with centimetric porphyroblasts of garnets and biotites. The cm-size (locally > 3cm) porphyroblasts of garnet are normally heuedral, often showing rombododecahedric habit. Normally, garnets are abundant among the micaschists of the whole SNFZ, often constituting more than 7-8% in volume of the whole rock (Zanchetta, 2010). The SMU is interpreted as a Paleozoic sedimentary succession with an Alpine tectono-metamorphic imprint (Hoinkes et al., 1987; Sölva et al, 2005; Zanchetta, 2010) A total number of 5 deformation stages, considered to be discrete events along a continuous exhumation path, were distinguished (Sölva et al, 2005). The SMU/ÖSC boundary is interpreted to by a brittle/ductile tectonic contact, defined by distributed brittle strain with distinct catacalsite zones, slickensides and pseudotachylites (Sölva et al, 2005). The extensional activity of the tectonic contact was preceded by a north-verging thrust-type activity (Sölva et al, 2005).

The Ridnaun Valley is a typical alpine valley of glacial origin, as well documented by both erosional and depositional morphological features and the widespread presence of Pleistocene glacial deposits. All glacial deposits covering the slopes at this sector of the eastern Alps are related to the Last Glacial Maximum (LGM), yielding an age variable from 29000 to 17000 <sup>14</sup>C (Penck and Brückner, 1904; Preusser, 2004; van Husen, 1997, 2000, 2004). During the maximum expansion of Pleistocene glaciers, the glacial tongue almost completely filled the Ridnaun Valley and the neighboring valleys, reaching a thickness of about 1000 m (van Husen 1997; Kellerer-Pirklbauer et al., 2009; Ostermann, personal communication).

The study area is surely involved in actual neotectonic deformations, as well defined by the ongoing seismicity affecting the neighboring valleys and by recent studies on the seismicity of the central and eastern Alps (Forcella et al., 1982; Slejko et al., 1989; Khale et al., 1997; Castaldini et al., 1992; Persaud and Pfiffner, 2004; Caporali et al., 2005; Agliardi et al., 2009). In the central eastern Alps, around 200 events with magnitudes (M<sub>w</sub>) ranging between 2 and 4.9 were recorded during 1975-2008 (Bargossi et al., 2011). Focal mechanism identified in the central eastern Alps show mainly strike-slip activity, expressed by left-lateral movements along NNE-SSE striking faults and right-lateral movements along NW/WNW-ESE striking faults (Bargossi et al., 2011; Forcella et al., 1982; Castaldini et al., 1992), indicating a N-S and NNW-SSE direction of the maximum compressive stress (Fig. 4.2; Agliardi et al., 2009).

Two active seismic regions of the central eastern Alps are located nearby the Ridnaun Valley: Inntal area and the Vinschgau Valley area (Fig 4.2). Considering the last one, the most famous event that hit the area happened on 17 July 2001 with M 4.8 (Caporali et al, 2005). The epicenter of this event was located near the town of Merano, around 30km to the SW from the Ridnaun Valley.

Hence, although not directly affected by active faults, the Ridnaun Valley could be affected by severe shakings induced by the high seismicity of the neighboring areas.

### **4.3 Material and Methods**

The understanding of the close relationship between gravitational geomorphic features, inherited structural framework and deep-seated deformations requires a multidisciplinary approach, that combines geological, geomorphological and geomechanical analyses (Zorzi et al., under review). The geomorphological mapping of the entire studied area has been carried out on a scale of 1:10000 using historical orthophotos (from 2003, 2006 and 2008), a High Resolution Digital Elevation Model (HRDEM, resolution: 2m) obtained from Airbone Laser Scanning (ASL) (2006 LiDAR surveys made by the Autonomous Province of Bolzano) and detailed field work.

The main advantages of using HRDEM (Oppikofer et al., 2011; Pedrazzini et al., 2011; Jaboyedoff et al., 2008, 2012) are i) a better detection of the typical morphological structures and geometries (i.e. scarps and counterscarps, mobilized material, slope geometry) through shaded relief images and ii) a detailed analysis of inaccessible areas. In our study, the use of ALS derived HRDEM was of fundamental importance in the detection of all the geomorphic features involving the slope, all the regional and local structural features, and the creation of detailed topographical profiles for a complete analysis of the slope morphologies.

The structure and mechanism of the slope deformations were investigated by means of structural geology and geomechanical methods.

Mesostructural analysis was used to measure and detect relevant structural elements such as regional, inherited ductile framework and main brittle features, such as joints and faults, on rock outcrops situated along the studied slope. Measurements of the orientation of foliation, axial plane foliations, and crenulation cleavages were collected on each mapped outcrop. All the structural data were fundamental for the definition of the brittle-ductile setting of the metamorphic units defining the study slope, as well as the relationship between the ductile setting, metamorphic anisotropy of the rock mass and the gravitational-induced geomorphic features.

Geomechanical surveys were carried out in order to collect information about the physical properties of the rock mass and discontinuity sets (Fig. 4.3). Scanline surveys were done to systematically characterize the discontinuities sets providing the fundamental parameters needed for the geomechanical characterization of rock mass, such as orientation, persistence, spacing and termination of the discontinuities as well as Joint wall Compressive Strength (JCS) and Joint Roughness Coefficient, (JRC) (Willye and Mahr, 2005). Rock Quality Designation index (RDQ; Deere and Miller, 1966), Rock Mass Rating (RMR; Bieniawski, 1976), and the Q index (Barton, 1974, 2002) for rock mass classification were evaluated for each geomechanical station. Average values of RMR rate and Q index made possible to obtain, through empirical correlation (Hoek and Brown, 1980; Bieniawski 1989; Barton, 2002) geomechanical properties of the rock mass, such as rock mass Young modulus, rock mass cohesion and rock mass friction angle, fundamental for a complete characterization of the rock mass and for further numerical simulations (see chapter 5).

The Joint Wall Compressive Strength (JCS) of the recognized joint sets was measured directly on the field thank to the used of the electronic “SilverSchmidt” Schmidt Hammer (see chapter 2; SilverSchmidt, 2010).

Schmidt hammer tests were performed in all the geomechanical stations reported in figure 4.3, but a systematic data collection was possible only on the scanline - type stations.

The JRC is expressed by a number estimated by comparing the appearance of a discontinuity surface with standard profiles published by Barton and Choubey (1977).

For each mapped outcrop during the field work, a value of the Geological Strength Index (GSI) was evaluated and assigned. The GSI, introduced by Hoek (1994), Marinos and Hoek (2000), provides a system for estimating the reduction in rock mass strength for different geological conditions as identified by field observations (Hoek et al., 1998). Rock mass strength is assigned by ready field observations of the rock mass structure and the conditions

of fractures planes, in terms of roughness and alteration (Hoek et al., 1998; Marinos and Hoek, 2000). The combination of these two parameters allows the estimation of GSI values by mean of contours given by the GSI tables proposed by Hoek (1994), Hoek et al. (1998), Marinos and Hoek (2000). In specific, for this work the updated version of the GSI table proposed by Marinos and Hoek (2000), which accommodates the effect of schistosity and shear planes, was used. A GIS-based contour map of the GSI values, using ArcGis 9.3, assigned to all mapped outcrops was then created to evaluate the spatial distribution and possible variability of the values (Fig.4.4).

#### **4.4 Geomorphology of the left slope of the Ridnaun Valley**

The actual morphology of the left slope of the Ridnaun Valley is mainly the result of glacial, periglacial and gravitational processes. On one hand, glacial erosion features, such as roche moutoneè and smoothed outcrops, LGM - glacial deposits and slope deposits dominates the Quaternary units at high altitudes on the studied slope (i.e. above 1700 m a.s.l.). On the other hand, large debris flow bodies, alluvial and colluvial deposits, both as widespread deposits and alluvial deposits, cover the bedrock units in the downhill sectors of the slope (Fig 4.5).

Detailed field work and the ALS-HRDEM analyses allowed the definition of three sectors of the slope showing different morphological and evolutionary features highlighting a quaternary differential gravitational evolution of the studied slope. The sectors were named Western, Central and Eastern respectively. Well-developed glacial cirques, responsible for the concave topography of the uphill half of the studied slope, characterize the detected sectors at high altitudes (Fig. 4.5, 4.6 and 4.7). In addition, the relief of the slope shows an increasing trend going from the west to east, with a mean value for each detected sector of about 1350 m, 1440 m, and 1500 m respectively. The slope gradient is quite uniform among the entire studied area, ranging from 30° to 35°. Locally, slope gradients of about 40° can be found especially on the Eastern sector.

The Western sector presents a regular topography, with slightly concavity in the central part of the section and an incipient convexity in the downhill half of the slope, indicating a possible downhill mass transfer due to a DSGSD affecting the slope (Fig. 4.7).

The central sector of the slope is characterized by bench-like topography in its uphill half, with a regular geometry in the downhill half of the slope. This geometry is the expression of a fully evolved gravitational collapse having the typical features of a rock avalanche (Fig. 4.5 and 4.6; see next paragraph).

The eastern sector presents an irregular topographic profile, with the upper part of the slope showing a concave geometry, and the central part characterized by a slightly developed bulge

(convex profile; Fig 4.7). This topography is interpreted derived from a combined geomorphic effect induced both by glacial erosion and gravitational deformation: the glacial-induced concavity has been enhanced by a downhill gravitational mass transfer, resulting in the convex topography of the central part of the slope highlighting the presence of a DSGSD.

At present time, the morphological evolution of the left slope of the Ridnaun Valley is dominated by gravitational and alluvial processes. Indeed, the entire ridge of the slope is affected by rockfalls and toppling, inducing a northward regression of the ridge itself. In addition, rockfalls and toppling failures characterize the uphill half of the Central sector, mainly concentrated at the rock avalanche crown area. The debris fans and deposits generated by the slope failures act as source material for debris flows, triggered by the heavy rainfalls that hit the area mainly during the warm seasons (Fig 4.5).

#### *4.4.1 Western sector*

Slope deposits represent the dominant geomorphological unit covering the Western sector, with the glacial unit limited to a small portion of the sector (Fig. 4.5). In fact, LGM-glacial deposits and paraglacial features, such as rock glaciers, were detected in the westernmost portion of this sector, whereas in the remaining area they can be found only locally at altitudes higher than 2100 m a.s.l. The Western sector of the slope is cut by gravitational geomorphic features between an altitude ranging from 1850 m and 2250 m (Fig.4.5). They are expressed by high angle WNW-ESE striking scarps, counterscarps, and trenches, locally presenting an echelon geometry. In fact, the lateral continuity of the detected features is variable, ranging from a few tens of meters to a hundreds of meters. The openings also show variable values, from a minimum of one meter to a maximum of about ten meters, filled with coarse debris or colluvial sediments. Surficial alteration and presence of turf locally mask these features in the field, but they can be easily detected through ALS-HRDEM image analysis (Fig.4.5 and 4.6). Despite a regular topography indicating a quasi-stable condition of this sector of the slope (Fig. 4.7), the detected geomorphic feature suggests the presence of an ongoing deep-seated deformation affecting this area, named “Wetterspitz DSGSD”. In fact, the high number of geomorphic features detectable on the slope, couple with the presence of polished surfaces mainly in correspondence to the scarps, led us to believe in high degree of activity of the DSGSD (Fig. 4.8). Two incise channels, coupled with NNE-SSW and NNW-SSE trending geomorphic feature limit the deforming area to the east end to the west.

Despite the high degree of fracturing showed by the bedrock units, this sector of the slope is characterized by the presence of a high number of gullies and permanent stream that cut the slope, highlighting high degree of surficial water discharge.

#### 4.4.2 Central sector

The main morphological feature of the entire left slope of the Ridnaun Valley is the huge rock slope failure body filling the Central sector of the slope, which has been already noticed by several authors (Klebelberg, 1953; Holzmann, 2005; Ostermann et al., 2010). Its deposit is defined by a grain-sustained massive diamicton, with angular clasts covering the entire granulometric scale (Fig. 4.9), indicating a strong comminution process that involved the failed material. According to Ostermann et al., (2010), the estimated volume of the failed mass is about  $0.6 \text{ km}^3$ , covering an area of about  $2.4 \text{ km}^2$ . Thus, this rock slope failure can be classified as a *Rock Avalanche*, due to its kilometric size and the features of the deposit (strong degree of fracturing, *diamicton* texture, and absence of rounded and scored clasts, lithological homogeneity). Considering the lithology detected on the failed mass, the failure involved mainly the micaschists of the SMU, and partially the paragneisses of the ÖSC (Fig. 4.5).

This mass wasting event had blocked the Valley, resulting in a rock avalanche – dammed lake. This has been breached and run out at an interval of time not yet defined. Radiocarbon dating of organic remnants from a sandy deltaic succession shed into the former rockslide lake yielded an age of  $8865 \pm 50$  year BP; implying an older age for the rock avalanche event (Ostermann et al., 2010). The source of the failed material is defined by a 2 km long crown area, well detectable from the ALS-HRDEM images (Fig. 4.5 and 4.6). Heim's Fahrböschung (runout travel angle,  $\tan\alpha$ ) related to this event has a mean value of 0.3.

High angle NW-SE trending scarps and counterscarps still cut the two glacial cirques and the relative glacial and paraglacial deposit defining the uphill half of the slope in this sector. These geomorphic features show higher trace lengths (maximum trace length detected is about several hundreds of meters) and openings respect to the one of the DSGSD of the Wetterspizt (Fig. 4.5, 4,6 and 4.8). The maximum horizontal displacement between the main scarps and associated counterscarps, which are located in the proximity of the rock avalanche niche area, can be locally about 15m. Polished surfaces, and new opened tension cracks, easily recognizable in the field due to the lack of any infill material, highlight ongoing gravitational instabilities affecting this sector of the slope, most probably triggered by the unloading induced by the rock avalanche.

Rockfalls and toppling failures involve the steep walls of the rock avalanche niche, inducing a northward regression of the crown area. The northward regression of the niche favors the unloading of the rock avalanche crown area, sustaining the entire deep-seated deformation of the rock avalanche crown area. In addition, the debris fans and deposits generated by the slope failures act as source material for debris flows, triggered by the heavy rainfalls that hit the

area mainly during the warm seasons, responsible of the important debris flows fans that cover the bedrock units in the downslope half of the Central sector (Fig 4.5).

Geomorphic features can be detected only in the uphill half of the Central sector, whereas in the downhill half no evidences of active deep-seated deformation were detected. Morphology interpretable as a small niche of a minor rock slope failure involving the slope is well detectable on the easternmost part of this sector in ALS-HRDEM images (fig. 4.6). The deposit of this secondary failure, well detectable in the field within the rock avalanche debris and made quite completely by the micaschists units of the SMU, is defined by a rock mass subdivided into decametric blocks, with a low degree of fracturing respect to the surrounding rock avalanche debris. This rock slope failure can be classified as a rockslide.

#### *4.4.3 Eastern sector*

The Eastern sector, with its irregular topography complicated in its uphill half by the presence of scarps and trenches, shows evidenced of a DSGSD evolution (Fig. 4.6 and 4.7). Slope gradients ( $32^{\circ}$  -  $35^{\circ}$ , locally reaching  $40^{\circ}$ ) and slope relief (1500 m) for this sector of the studied slope, displayed values that has to be consider as favorable for DSGSD developments, as reported by several authors (Zischinsky, 1966, 1969; Radbruchh-Hall et al., 1976; Mahr, 1977; Mortara and Sorzana 1987). Differently to the other two sectors, no polished surfaces or newly opened tension cracks were detected during field surveys in this area. This indicates ongoing rate of activity lower than the ones showed by the other two detected rock slope instability. In addition, ALS-HRDEM images highlight a cluster of mainly WNW-ESE trending structures mainly in the western part of this sector, in correspondence to the glacial cirque responsible for the concave morphology of the slope in this part of the sector (Fig.4.5 and 8). On the contrary, no evident structures can be detected on the remaining part of the slope. Nevertheless, field surveys in the downhill half of the slope revealed the presence of trenches and scarps, having low persistency and openings. These structures cannot be distinguished on ALS-HRDEM mainly for two reasons: i) the dimension of the structures are in the same order of the ALS-HRDEM resolution; ii) the intense underwood and vegetation tends to hide the geomorphic features even on the shaded relief images.

Despite the high degree of fracturing showed by the bedrock units, even this sector of the slope is characterized by the presence of a high number of gullies and permanent stream that cut the slope, highlighting a high degree of surficial water discharge.

The quite random distribution of the gravitational structures, associated with unclear east and west boundary of the deforming area, induce us to consider the deformation as an unconfined DSGSD, which has been named DSGSD of the “Telfer Weissen”.



## 4.5 Interferometry data

PS and DS - SAR (Synthetic Aperture Radar) interferometry data (derived ERS, ENVISAT and RADARSAT scenes), generated by the Tele-Rilevamento-Europa (TRE) and provided to the EURAC-Institute for Applied Remote Sensing for the EU-FP7 Project 'SAFER', with the purpose of an integration of the Inventory of Landslide Phenomena in Italy (IFFI Project), testify an ongoing movement on both the newly defined DSGSDs bordering the rock avalanche.

The data cover three year of measurements (March 2003 – March 2006), and due to the orientation of the slope (south-facing slope of an E-W trending valley), are relative to descendent orbit of the satellite. Thus, a displacement map that can be derived from the raw data is relative to movement along the line of sight (LOS), and do not have to be consider as absolute 3D.

Contour map of LOS displacements, created and kindly given by the geology survey group of the Autonomous Province of Bolzano (Italy), shows evidence of an ongoing differential gravitational evolution of the left slope of the Ridnaun Valley (Fig. 4.10). In fact:

- The Wetterspitz DSGSD detected in the field is characterized by high rates of LOS-displacement (15-35 mm), with displaced reflectors covering the entire deforming area.
- The Telfer Weissen DSGSD shows displacement confined only to the area affected by the detected gravitational structures (scarps, counterscarps and trenches), with the remaining areas of the DSGSD that do not show any rate of movements. The absence of displaced scatterer along the slope does not necessary mean and absence of deformation. In fact, the intense vegetative cover of the Eastern sector of the slope impedes the detection of reliable permanent scatterers. Although no evidence of movements derives from interferometry data, evidences of trenches and scarps can be found in the field, testifying an ongoing deformation affecting this sector of the slope (paragraph 4.4.3).
- The deep-seated deformation involving the rock avalanche crown area can be divided into two part, which show variable rates of displacement: the western part has high rate of LOS-movements (10-30 mm), whereas the eastern part is affected by lower LOS-movements (0-15 mm). Low rate LOS-displacement has not to be interpreted uniquely as the evidence of low rate of deformation in the rock mass, because they can be also interpreted as the evidence of high deformation rates affecting the slope. In

fact, high deformation rates may have induced the loss of the permanent scatterer during data acquisition. Indeed, the low rate LOS-displacement may simply derived from the integration of displacement data, recorded only in the first stages, through the entire acquisition period (i.e. 3 years; Iasio C.Eurac research group, personal communication).

Thus, the available interferometry data seem to confirm the kinematic behavior of the slope coming from the geomorphological analysis, highlighting a most unstable area at the Wetterspitz DSGSD.

#### **4.6 Geomechanical analysis**

Geomechanical surveys were carried out in order to collect information about the physical properties of the rock mass and discontinuity sets (Fig.4.3). A total number of 45 geomechanical stations (20 scan-line type and 25 “random” type) were performed trying to cover all the sectors and lithologies characterizing the studied area. Locally, scan-line having a total length less than 5m were performed due to the reduced extension of the available outcrops.

The spatial distribution of the geomechanical station is not uniform among the slope (Fig. 4.3). Presence of widespread thick Quaternary cover hiding the bedrock, coupled with outcrops located in highly hazardous areas due to rockfalls and toppling, made locally difficult to find available and useful outcrops for geomechanical investigation, like in the Central sector of the slope (Fig.4.3 and 4.5).

The complete description of the geomechanical properties calculate for each geomechanical station are reported in Appendix XX.

More than 1000 discontinuities were measured during the field surveys and the following faults and joint sets were recognized (Fig.4.3):

- a NW-SE striking set dipping towards the SW (average dip =  $70^\circ$ ), named K1;
- a N-S striking set dipping towards the W (average dip =  $75^\circ$ ), named K2;
- a WNW-ESE striking set dipping towards the NW (average dip =  $45^\circ$ ), named K3;
- a N-S striking set dipping towards the E (average dip =  $75^\circ$ ), named K4;
- a E-W striking set gently dipping towards the N (average dip =  $14^\circ$ ), named S because it follows the regional foliation defining the fabric of the bedrock units.

The detected sets are not present continuously in all the three sectors. The Eastern sector is characterized by all 5 discontinuity sets, whereas in the Western sector the K2 systems is missing or only sporadically present (Fig.4.11). The Central sector is the one showing a completely different brittle setting, because only K2 and S sets were detected (Fig. 4.11).

To analyze possible trend in rock mass properties, GSI contour map was created in a GIS environment, considering in particular the slope ridge area (Fig.4.4). GSI contour maps do not show any clear E-W trend, whereas discrete NE-SE trend are highlighted from the GSI distribution (Fig.4.4). Lowest GSI values are located on areas affected by rock slope instabilities, in which gravity-driven geomorphic structures increase the degree of fracturing of the rock masses.

Clear differences between the two bedrock complexes arise considering the JCS values. SMU JCS values show mean low values, between 10-40 MPa, whilst ÖSC is defined by higher JCS values ranging from a minimum of 40 MPa to a maximum of 100 MPa. A W to E decreasing trend in JCS seems arise from the measured values, which seems to be independent from lithology and discontinuity sets.

Indeed, geomechanical data seem to support the subdivision of the slope into three main sectors.

#### **4.7 Structural analysis**

In order to evaluate the predisposing and controlling factors of the detected rock slope instabilities, detailed structural surveys, mapping of meso-structural elements at 1:10.000 scale, and microstructural analysis using a polarizing microscope were performed to unravel the brittle-ductile setting of the studied slope.

The entire studied slope is characterized by a low angle (15°-20°) NNE-dipping foliation (Sr), interpreted to be eo-Alpine in age by several authors in different sector of the SNFZ (Frizzo et al., 1982; Hoikens et al., 1987; Van Gool et al., 1987; Sölva et al., 2001, 2005).

Considering first the ductile setting of ÖSC, relicts of an ancient foliation ( $S_1$ ) were found within the low angle NNE-dipping eo-Alpine regional foliation Sr (Fig.4.5). According to Hoinkes et al.(1987) and Sölva et al. (2005), the detected  $S_1$  foliation is Variscan in age, and successively it has been folded during the during the Cretaceous eo-Alpine stage of the Alpine deformation (Van Gool, 1987). In fact, m-scale open to close S-SE verging folds with WNW-ESE trending axes define the  $S_1$ , inducing a change in dip direction of the foliation from a high-angle SSW-dipping foliation to a low angle E-dipping foliation (Fig. 4.5).  $S_1$  folds become more intense approaching to the SMU/ÖSC tectonic boundary. A slight E-W trending crenulation cleavage can be found also in the paragneisses of the ÖSC, whose intensity increases approaching to the SMU/ÖSC tectonic boundary.

No evidence of  $S_1$  foliation at the mesoscale was found in the SMU. In fact, SMU units are defined by more pervasive and continuous Sr foliation (Fig. 4.12), marked by biotite and white mica. The metamorphic eo-Alpine deformation completely obliterated the  $S_1$  foliation,

giving rise to the regional mylonitic foliation. A more intense E-W trending crenulation cleavage involves mainly the garnet micaschists of the SMU along the slope, which follow the trend found in the ÖSC (Fig. 4.5). C'-type shear band cleavages, with mainly high-angle S-dipping C'-structures, were locally detected within the garnet micaschists (Fig.4.12).

The main brittle structural element affecting the studied area is the low angle NW-dipping SMU/ÖSC tectonic contact (Fig.4.5), which obliquely intersects the E-W trending slope. Field work has unraveled the presence of a low angle NW-dipping ultracataclastic fault set (UTC, Fig 4.5 and 4.12), following the attitude of both the main tectonic contact and the regional foliation Sr. The fault sets, defined by a coherent and incoherent ultracataclastic core having a thickness between 10 and 30cm (Fig. 4.12), involves the hangingwall paragneisses units of the ÖSC, with decreasing spacings approaching to the tectonic contact (> 10 m near the ridge area of the slope; < 1 m approaching to the SMU/ÖSC boundary). UTC faults can be interpreted as the result of strain partitioning in the ÖSC most probably during the eo-Alpine deformation involving the SNFZ. In fact, UTC faults were rarely detected in the SMU, indicating a purely ductile behavior of this unit under the eo-Alpine deformation, as shown by Sölva et al. (2005).

Due to the widespread presence of quaternary and vegetative cover, the SMU/ÖSC boundary is not easily detectable in the field, and its attitude was traced on the bases of i) the spatial distribution of the outcrops of the due units and ii) spatial distribution of UTC faults.

Beside UTC fault, other three fault sets were detected during field surveys named F1, F2 and F3 (Fig 4.11). The high-angle N-S trending F1, and the high-angle NE-SW trending F2, are the two main sets, both defined in the field by a 1-1.5 m thick fault core made up by an incoherent fault breccia (Fig. 4.12). F1 set is much more intense in the Western sector of the slope (Fig.4.5). The recognized fault sets subdivides the slope into blocks, following the three detected geomorphic sectors.

#### **4.8 Gravitational evolution of the left slope of the Ridnaun Valley**

The multidisciplinary approach, by means of geomorphological, geological and geomechanical analyses, used in this work allowed the definition of the structural predisposing factors for the Quaternary differential evolution of the left slope of the Ridnaun Valley. The relationship between the brittle/ductile structural setting, the geomechanical setting and the detected rock slope instabilities will be presented in this paragraph.

#### 4.8.1 *Wetterspitz DSGSD*

Due to the position of the SMU/ÖSC tectonic boundary along the slope (Fig.4.5 and 4.14), the deforming area involves mainly the paragneisses of the ÖSC. In fact, scarps and trenches are pervasively and uniformly distributed among the ÖSC, involving the SMU only approaching to the SMU/ÖSC boundary (Fig. 4.5 and 4.6).

The absence of springs outcropping at the base or along the slope, coupled with the widespread distribution of scarps and trenches along the deforming area, do not give the evidence of a localized basal surface at the base of the slope. Despite the high degree of fracturing showed by the bedrock units, a high number of gullies and permanent stream cut the slope in this sector, evidencing high degree of surficial water discharge. The quite regular topography showed by the slope in this sector (Fig.4.7 and 4.14), associated with low dimensions of the recognized geomorphic features (in terms of horizontal displacement), let us believe that the thickness of the deforming area has to be consider low (<50 m). Given a possible thickness of about 50m, the probable volume involved in the deformation is about  $27 \cdot 10^6 \text{ m}^3$  (table 1; Fig.4.14).

The DSGSD is confined between F1 and F2 fault sets, which, due to the low shear strength of the incoherent breccia defining the fault core, act as lateral release for the gravitational deformation.

The high angle S-dipping K1 discontinuity set, coupled with the F1 and F2 faults, isolates a slope block containing the deforming area (Fig. 4.13).

Due to the position of the DSGSD among the tectonic contact, the ÖSC is quite dominated by the folded SSE-dipping  $S_1$  foliation, showing here high angle SSW-dipping axial planes. Thus, the ductile setting of the paragneisses of the ÖSC is favorably oriented to act key discontinuities enabling kinematical release for the DSGSD. On the other hand, in the SMU only the low angle N-dipping regional  $S_r$  foliation was detected. Thus, no clear discontinuities which can control the slope deformation are present in the SMU, although evidences of deformation involving the SMU can be found in the field (paragraph 4.3; fig. 4.5, 4.6 and 4.13). It is reasonable to believe that the garnet micaschists units of the SMU are interested by a widespread deformation, allowing the rock mass to react in a brittle-plastic way to the gravitational-induced stresses.

Given all the above mentioned characteristics, the Wetterspitz DSGSD can be interpreted as a deep-seated sliding, mainly controlled by the S-dipping  $S_1$  foliation on the ÖSC. In addition, interferometry data, coupled with the high number of geomorphic features affecting the deforming area, allow considering this DSGSD affected by an ongoing high degree of activity.

#### 4.8.2 *Telfer Weissen DSGSD.*

Due to the position of the SMU/ÖSC tectonic boundary along the slope (Fig.4.5 and 4.13), the deforming area involves mainly the garnet micaschists of the SMU, involving the paragneisses of the ÖSC only at the crown area, among the SMU/ÖSC tectonic boundary. In this sector, the NNW-dipping  $S_r$  foliation in the ÖSC, is more pervasive, with  $S_1$  domains localized only close to the tectonic contact. The recognized morphostructures involving the ÖSC, defining the crown area of the DSGSD, are confined within the  $S_1$  domains.

NNW-dipping  $S_r$  regional foliation defines the fabric of garnets micaschists, with  $C'$ -type shear band cleavages defining discrete domains within the garnet micaschists (Fig. 4.12).  $F_1$  and  $F_2$  intersect the deforming area, but, differently from the previous DSGSD, no clear confining effect seems to be played by the fault sets. In fact, only the east boundary of the DSGSD seems to be limit by a NNW-SSE trending fault, whereas no structures or geomorphological and geomorphic feature can be consider as a clear west boundary for the deforming area. Thus, uncertainties still remain on the extension of the DSGSD. The brittle discontinuity setting, defined through geomechanical survey, highlight that this area is characterized by the high angle S-dipping  $K_1$  set.  $K_1$  discontinuity set, coupled with the  $F_1$  and  $F_2$  fault sets isolate in 3D the block containing the DSGSD but do not control the deformation.  $K_2$ ,  $K_3$  and  $K_4$  discontinuity set contribute to increase the degree of fracturing of the rock mass.

Uncertainties still remain also for the south boundary of the DSGSD. The irregular topography induces to consider the toe of the bulged morphology as the southern limit of the deforming area (Fig. 4.6). However, scarps, conterscarps and trenches can be found in the field also on altitude below 1600m (downslope the bulge topography; Fig.4.7 and 4.14), letting us believe that the deformation involves the entire slope. Thus, the bulged area is interpreted as the expression of a more active sector of the DSGSD. There is no evidence of a localized basal surface at the base of the deforming slope. In fact, the lack of any springs along the slope especially at the base of the bulged topography, suggests the absence of a localized basal gliding discontinuity outcropping at the surface (Fig.4.14). The extreme fissility of the bedrock units, especially of the SMU, makes probable a shear deformation widely distributed along the deforming area.

Hypnotizing a west boundary located in correspondence to the east limit of the rock avalanche crown area, the south boundary at the toe of the slope, and a mean thickness of about 70 m, the volume of the deforming area is about  $160 \cdot 10^6 \text{ m}^3$  (Table 2).

Given the all described characteristic, the Telfer Weissen DSGSD is mainly controlled by a deformation widely distributed in the garnet micaschists of the SMU, inducing a brittle-plastic

rection of the SMU to the gravitational-induced deformation. The stiffer paragneisses of the ÖSC in the crown area of the DSGSD, react in a purely brittle way to the deformation favoring the formation of typical morphostructures, controlled by the  $S_1$  domains within the rock unit.

Due to the similar structural setting, and the probable dimensions of the pre-failure deforming area, the Telfer Weissen DSGSD can be considered as the pre-failure condition of the Ridnaun rock avalanche.

#### 4.8.3 *The Ridnaun rock avalanche*

Due to the position of the SMU/ÖSC tectonic boundary along the slope (Fig.4.5), the deforming area involves mainly the garnet micaschists of the SMU, limiting the involvement of the ÖSC only at the crown area of the failure (Fig. 4.5).

The rock avalanche source area is confined between F1 and F2 fault sets, which, due to the low shear strength of the incoherent breccia defining the fault core, most probably acted as lateral release for slope failure. The fault network seems to strongly influence also the brittle setting of the area. In fact geomechanical survey in this sector of the slope highlight only the presence of the K2 set, which contributed to increase the degree of fracturing of the pre-failure deforming rock masses (Fig.4.12).

Due to the location of the phenomenon on the slope and its position as regards the tectonic contact, it is reasonable to believe that structural control acting on the pre-failure condition of the Ridnaun rock avalanche is in between the one acting on the two DSGSDs. Like the Telfer Weissen DSGSDs, creeping brittle/plastic deformation of the garnet micaschists of the SMU, most probably triggered by the post-LGM glacial unloading, induced a purely brittle deformation of the ÖSC.  $S_1$  domains defining low strain domains within the low angle NNW-dipping regional  $S_r$  foliation, controlled the morphostructures development, as proven by active scarps and counterscarps driving the toppling instability that govern the present evolution of the rock avalanche crown area (Fig.4.8 and 4.11). More in detail, deep-seated toppling affecting the crown area of the rock avalanche most probably involve only the units of the ÖSC, with the SMU/ÖSC tectonic boundary limiting the deformation downslope (Fig.4.14)

## 4.9 Discussion

Geological, geomorphological and geomechanical surveys, coupled with detailed ALS-HRDEM and orthophotos analysis allowed us to subdivide the left slope of the Ridnaun Valley into three main sectors (Western, Central and Eastern), showing Quaternary

differential behavior and evolution (Fig.4.6); ii) to detect and analyze, besides the main geomorphic element expressed by the Ridnaun rock avalanche, two ongoing DSGSDs involving the Western and Eastern sector of the slope (Wetterspitz DSGSD and Telfer Weissen DSGSD respectively; Fig.4.6, 4.8 and 4.13) never pointed out before; iii) determine the brittle-ductile control on all the studied rock slope instabilities.

Geomechanical survey pointed out the presence of 5 main discontinuity sets (K1, K2, K3, K4, S), which are strongly controlled by the brittle/ductile structural setting of studied area. In fact, the S-dipping K1 set follows and reactivates the hinge zones of the E-W trending folds in  $S_1$ - domains. K2 and K4 follow the F2 and F1 fault sets respectively (Fig.4.11 and 4.13). The N-dipping K3 set is related to the UTC fault set, and can be structurally interpreted as synthetic Riedel structures deriving from extensional tectonic along the SMU/ÖSC boundary. The brittle discontinuity setting, defined by the three fault sets and the five discontinuity sets, is responsible i) on one hand for the subdivision of the slope into discrete 3D mega-blocks containing the deep-seated rock slope instabilities; ii) on the other hand, they increase the degree of fracturing of the rock masses, causing the worsening of rock mass quality in terms of GSI. In fact, low values of GSI are aligned mainly with the F1, F2 fault sets and related joint sets (K2 and K4)(Fig.4.4 and 4.13).

The Quaternary gravitational evolution highly depends on the interaction between the slope trend and the brittle/ductile structural setting. In fact, the non-parallelism between the ENE-SWS trending SMU/ÖSC tectonic contact and the WNW-ESE trending left slope of the valley induce an E-W increase of the area covered by the ÖSC and a relative E-W decrease of the one covered by the SMU (Fig.4.5, 4.13). The first effect is that the deep-seated deformations involve the two Austroalpine complexes in different proportion, with the Wetterspitz DSGSD mainly set on the ÖSC and the Telfer Weissen DSGSD mainly covering the SMU. As a consequence, the brittle-ductile control acting on the slope instabilities is different for each phenomenon. On one hand, the more stiff and brittle ÖSC units, with  $S_1$ -domains defined by a mainly S-dipping foliation, favor the development of a deep-seated sliding type deformation (Wetterspitz DSGSD; Fig. 4.13 and 4.14). On the other hand, due to the mm-scale metamorphic fabric, coupled with metamorphic anisotropy such as C'-type shear band cleavages, reaction rims (Fig.4.12) and crenulation cleavage, the garnet-micaschists of the SMU display a creeping brittle/plastic deformation, most probably driven by intense and widely distributed micro-cracking affecting the area under gravitational deformation (Telfer Weissen DSGSD; Fig. 4.13 and 4.14).

The Ridnaun rock avalanche is structurally located in between the two DSGSD (Fig.4.5, 4.13 and 4.14). Creeping brittle/plastic deformation of the garnet micaschists of the SMU, most



probably triggered by the post-LGM glacial unloading, induced a purely brittle deformation of the ÖSC.  $S_1$  domains defining low strain domains within the low angle NNW-dipping regional  $S_r$  foliation, controlled the morphostructures development, as proven by active scarps and counterscarps driving the toppling instability that govern the present evolution of the rock avalanche crown area. Radiocarbon dating yielded an age of  $8865 \pm 50$  year BP (Ostermann et al., 2010) for the rock avalanches, thus the debuttrass due to glacial withdraw cannot be considered as a trigger for the failure. Due to the vicinity of the left slope of the Ridnaun Valley to active seismic faults (Fig.4.2; paragraph 4.2), a seismic event can be considered as the key trigger of the rock avalanche evolution for the Central sector of the slope.

Together, the three instabilities can be interpreted as three different stages of the same evolutionary path, driving a creeping deforming rock mass into a rock avalanche-type failure. In addition, the Telfer Weissen DSGSD, due to similar structural setting and dimensions, has to be considered as the pre-failure condition of the Ridnaun rock avalanche.

#### **4.10 Conclusions**

The left slope of the Ridnaun Valley (Sterzing/Vipiteno, South Tyrol, Italy), set on the crystalline units of the Austoalpine Nappe of the alpine orogenic wedge, shows evidence of quaternary gravitational evolution which highly depends on the interaction between the slope trend and the brittle/ductile structural setting. The multidisciplinary approach used in this work aids the understanding of the Quaternary differential evolution of the slope. The results obtained by field work and the analysis of the LiDAR-derived digital elevation model clearly revealed different gravitational movements. A fully evolved gravitational collapse, having the typical features of a rock avalanche, characterizes the central part of the slope; whereas to the east and west of the rock avalanches, deep seated gravitational slope deformations, pointed out for the first time with this work, still involve the slope. The rock avalanche, whose deposit covers an area of about  $2.4 \text{ km}^2$ , had obstructed the valley, resulting in a rock avalanche – dammed lake. An ongoing gravitational deformation involves the uphill sections of the slope, next to the crown area. In addition, to the West and the East of the rock avalanche, morphostructural features as scarps – counterscarps, trenches are evident. PS and DS - SAR (Synthetic Aperture Radar) interferometry data (derived ERS, ENVISAT and RADARSAT scenes), kindly given by the Geological Survey of the Autonomous Province of Bolzano, testify an ongoing movement on both the DSGSDs bordering the rock avalanche, highlighting a most unstable area at the Western sector. Glacial unloading is to be considered as the most probable trigger for the detected DSGSDs, whereas a seismic trigger can be hypothesized for the Ridnaun rock avalanche.

The slope is carved within the paragneiss rocks of the Oetztal - Stubai Unit and the garnet-micaschists of the Schneeberg/Monteneve Unit. These two units are separated by a NNW gentle dipping tectonic contact, which obliquely intersects the E–W slope, and is well described by ultracataclastic and mylonitic layers following the regional low angle north-dipping foliation. Approaching to the tectonic contact, relicts of an ancient foliation within the regional  $S_1$  foliation in the ÖSC are defined by folds with sub-horizontal E–trending axes. The folds induce the change in the dip direction of the regional schistosity in the ÖSC from N dipping to SE dipping. NNE–SSW and N–S trending faults, having a mean 1 m thick incoherent fault breccia, affect the entire slope.

On one hand the recognized fault network together with the K1 discontinuity set, act as lateral release of the unstable areas; on the other hand, the small – scale folds in  $S_1$  domain within the ÖSC coupled with the non – parallelism between the tectonic contact trend and the slope, ease the DSGSD formation and evolution (Wetterspitz DSGSD), and acted as releasing factor for the crown area of both the rock avalanche and the Telfer Weissen DSGSD. The purely brittle deformation of the ÖSC mainly in the rock avalanche and the Telfer Weissen DSGSD, is interpreted to be driven by a brittle/plastic deformation of the garnet micaschists of the SMU, throughout a widely distributed micro-cracking of rock mass. Metamorphic anisotropy, such as shear band cleavages, crenulation cleavage, garnet porphyroblasts and reaction rims, has to be considered as site for micro-cracking nucleation and propagation through the rock mass. Hence, the Quaternary heterogeneous behavior of the slope is most likely controlled by the interaction between the ductile and brittle structures defining the slope.

## 4.11 Tables

<b>MORFOMETRY OF WETTERSPIZ DSGSD</b>	
<b>Average slope</b>	32° (63%)
<b>Slope relief</b>	630 m
<b>Azimuth of displacements</b>	240°
<b>Length</b>	950 m
<b>Probable width</b>	570 m
<b>Extension</b>	0,54 km <sup>2</sup>

Table 4.1: principal morphometric parameters of the Wetterspitz DSGSD

<b>MORFOMETRY OF TELFER WEISSEN DSGSD</b>	
<b>Average slope</b>	30° (58%)
<b>Slope relief</b>	1050 m
<b>Azimuth of displacements</b>	240°
<b>Length</b>	1830 m
<b>Probable width</b>	1278 m
<b>Extension</b>	2,4 km <sup>2</sup>

Table 4.2: principal morphometric parameters of the Telfer Weissen DSGSD

## 4.12 Figure captions

Figure 4.1: Geographical and geological setting of the study area; a) Geographical map of northern Italy; b) Structural map of the eastern Alps (from Sölva et al, 2005, modified); the rectangle represent the location of the study area c) Geodynamic model of the Schneeberg Normal Fault Zone (from Bestmann et al, 2011, modified).

Figure 4.2: Distribution of seismic event between northern Italy – South Austria

Figure 4.0.3: Map of the location of the Geomechanical station along the slope. As base map, a shaded relief image of ALS-HRDEM was used.

Figure 4.4: Map of the distribution of GSI values. The values show a discrete areas characterized by N-S distribution of the values.

Figure 4.5: Simplified geological map of the left slope of the Ridnaun valley on shaded relief image of ALS-HRDEM; a) contour plot of the foliations measured in the ÖSC (number of measures: 160); b) contour plot of the foliations measured in the SMU (number of measures: 130); c) contour plot of the crenulation cleavages measured within both the complex (number of measures:100);

Figure 4.6: Shaded relief image of ALS-HRDEM showing the subdivision of the slope into three sectors: Western, Central and Eastern. The rockslide body is visible in the eastern sector of the rock avalanche deposit, with a clear source area located on the slope. The rectangle a, b and c are related defined the location of the field images of Figure 4.8;

Figure 4.7: 3D ALS-HRDEM image of the study area (perspective view from the SE). The A-A' profile (Western) shows a near-stable geometry, with a slightly concavity, followed by an incipient bulging in the central sector of the slope; the B-B' profile (Central sector) highlights a strongly irregular topography, resulting from a fully evolved rock slope collapse; the C-C' profile is the expression of an unbalanced geometry: the uphill sector is characterized by a strong irregular topography due to the presence of a glacial cirque and morphostructures; the downhill part shows evidence of a bulge induced most by the DSGSD deformation.

Figure 4.8: Geomorphic features affecting each sector; a) field evidence of scarps and trenches relative to the Wetterspitz DSGSD (Western sector; view from the W); b) Geomorphic features deriving from the ongoing toppling evolution of the rock avalanche niche (Central sector; view from the W); c) Mainly trenches and scarps defining the crown area of the Telfer Weissen DSGSD (Eastern sector; view from the NW); d) polished surfaces indicating high rates of ongoing activity recorded by the morphostructures.

Figure 4.9: Outcrop of the rock avalanche deposit (image taken looking towards the south).

Figure 4.10: DS-InSAR interferometry map derived from Radarsat data (courtesy of the Geological Survey of the Autonomous Province of Bolzano). The image shows only LOS-displacement along a descending orbit (NE- Line of sight).

Figure 4.11: Contour plot of the brittle discontinuities measured in the field during both geological and geomechanical surveys; a) contour plot of the faults detected in the field (number of measures: 50); F1, F2 and F3 define the three fault sets detected, whereas UTC defines the ultracataclastic fault detected mainly in the ÖSC; b) contour plot of all the joint measured on the entire slope (number of measures: 1023); K1 set is the expression of a brittle

reactivation of the hinge zone of Sr folds; K2 set follows the F2 fault set (see image a in this figure) ; K3 follows the UTC faults; K4 is the expression of the fractures induced by F1 faults and the S set is the brittle reactivation of the Sr foliation ; c) contour plot of the joint sets measured on the Western sector (number of measures: 615); only the K1, K3, K4 and S sets were detected; d) contour plot of the joint sets measured on the Central sector (number of measures: 169); in this sector only K2 and S set were detected; e) contour plot of the joint set measured in the Eastern sector (number of measures: 208); this sector is the only one showing all five discontinuity sets.

Figure 4.12: a) Field example of the garnet-micaschists of the SMU; b) C'-type shear band cleavage found in the garnet-micaschists; In dashed red line the C'- structures; reaction rims (mainly sigma-type) accompany the garnet porphyroblasts; c) crenulation cleavage of the garnet-micaschists of the SMU; d) Field evidence of the low angle N-dipping ultracataclastites; in specific, the image represents an incoherent ultracataclasite; e) field expression of F1 and F2 fault sets; the picture shows a F2 fault, defined by a damaged fault core having the thickness of about 1-1.5 m filled by an incoherent fault breccia.

Figure 4.13: Geological and geomorphological setting of the detected rock slope instabilities; a) geology of the Wetterspitz DSGSD; the DSGSD involves mainly paragneisses ÖSC than the SMU. b) zoom on the rock avalanche crown area; scarps and trenches define ongoing gravitational deformation affecting the area; c) Geology of the Telfer Weissen DSGSD; the DSGSD involves mainly the garnet micaschists of the SMU, confining the ÖSC in its crown area.

Figure 4.14: Geological section of the detected deep-seated deformation; traces of the sections are the one for the topographic profile of figure 4.6. a) geological cross-section of the Wetterspitz DSGSD; b) geological cross-section of the Ridnaun rock avalanche; the dashed black line represents the hypostasized pre-failure topography; c) geological cross-section of the Telfer Weissen DSGSD; uncertainties still remain on the width of the deforming area.

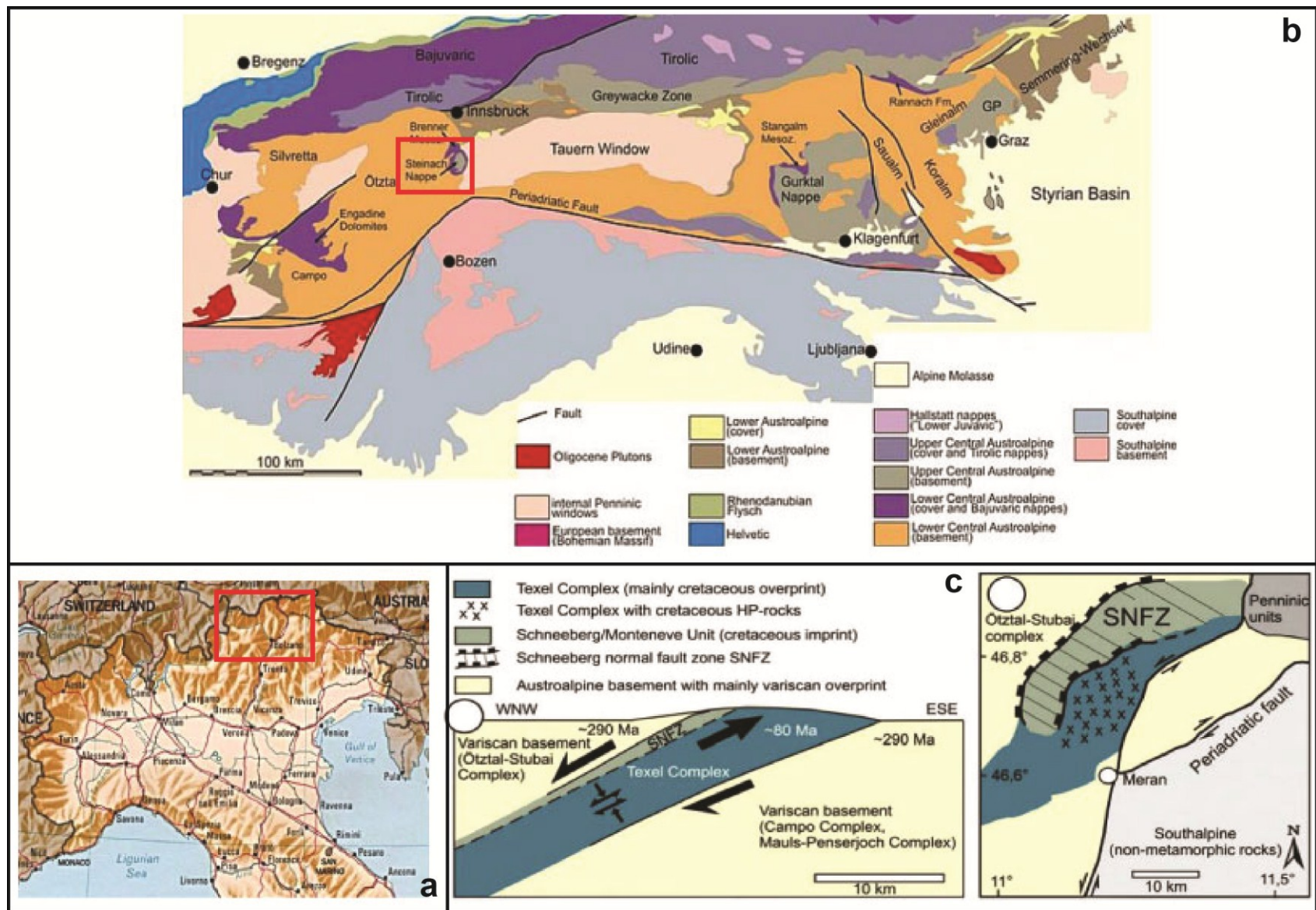


Fig. 4.1

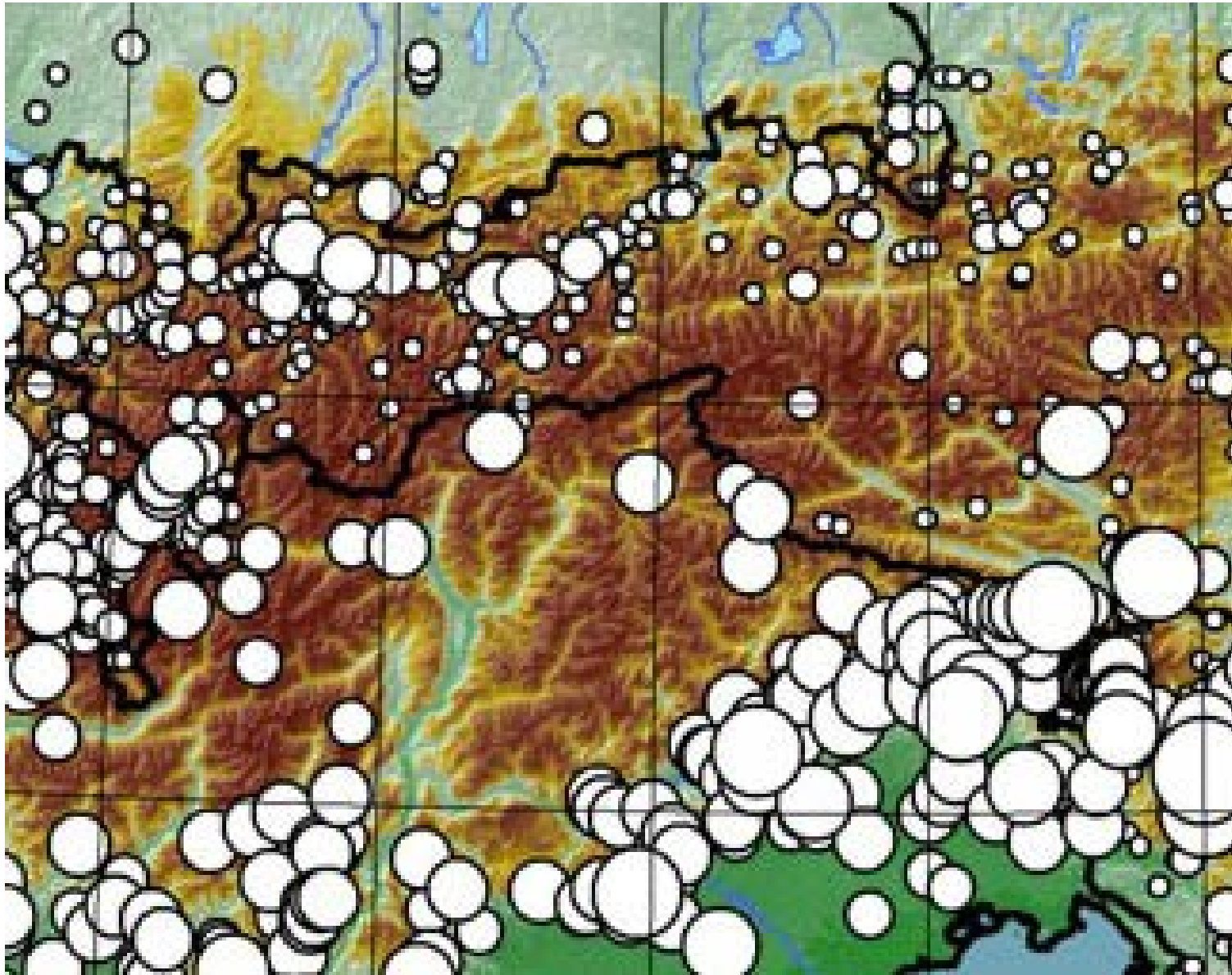


Fig. 4.2



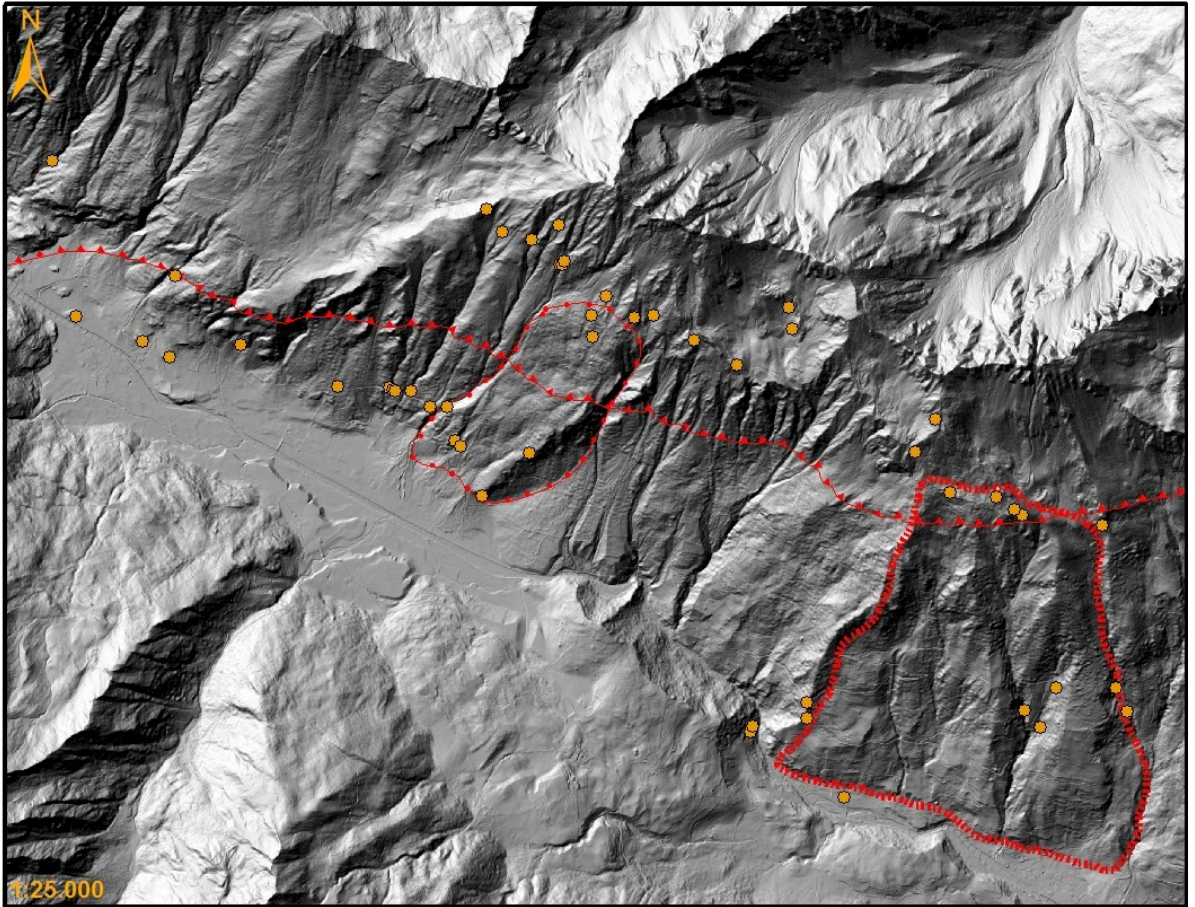


Fig. 4.3



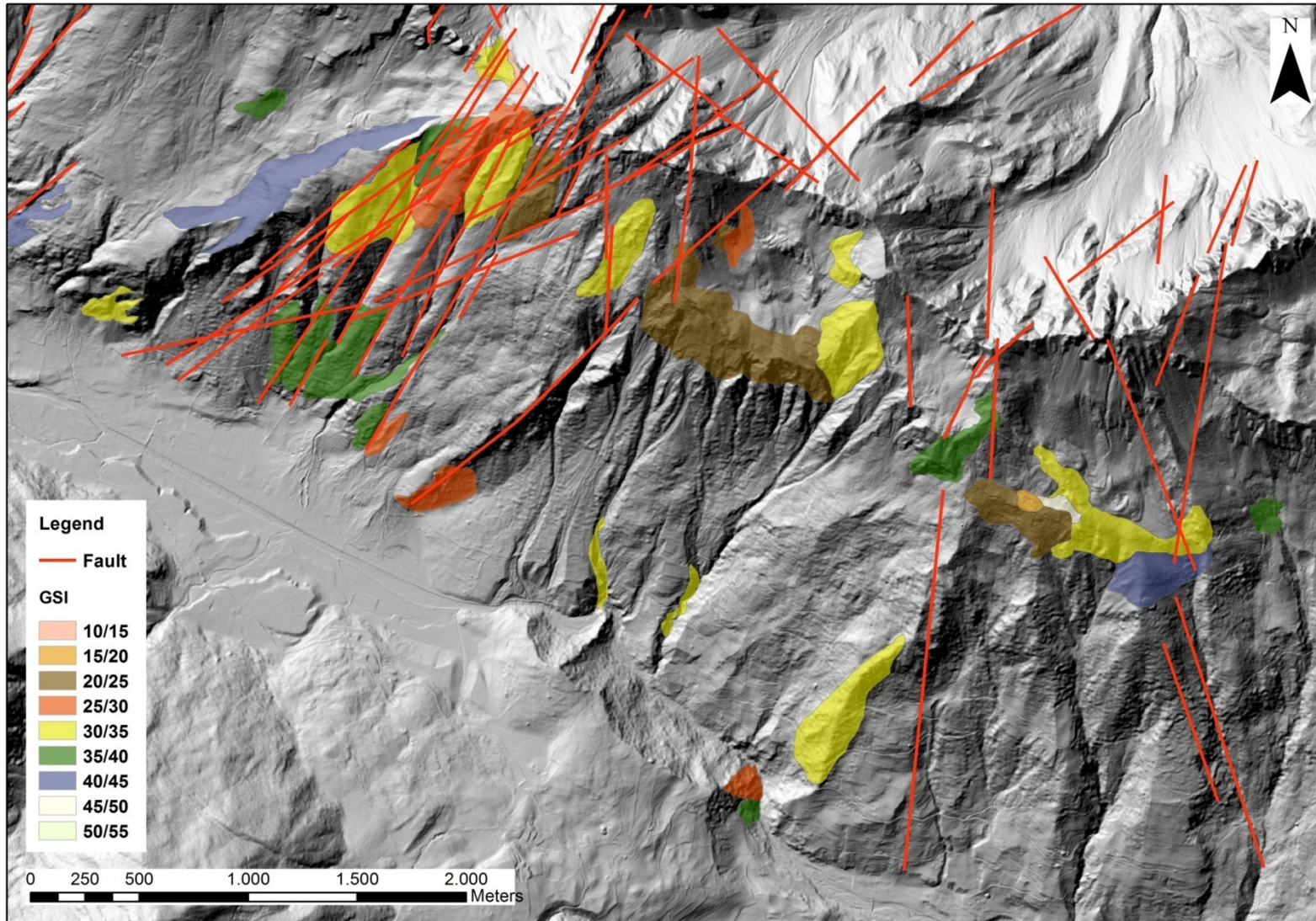


Fig. 4.4



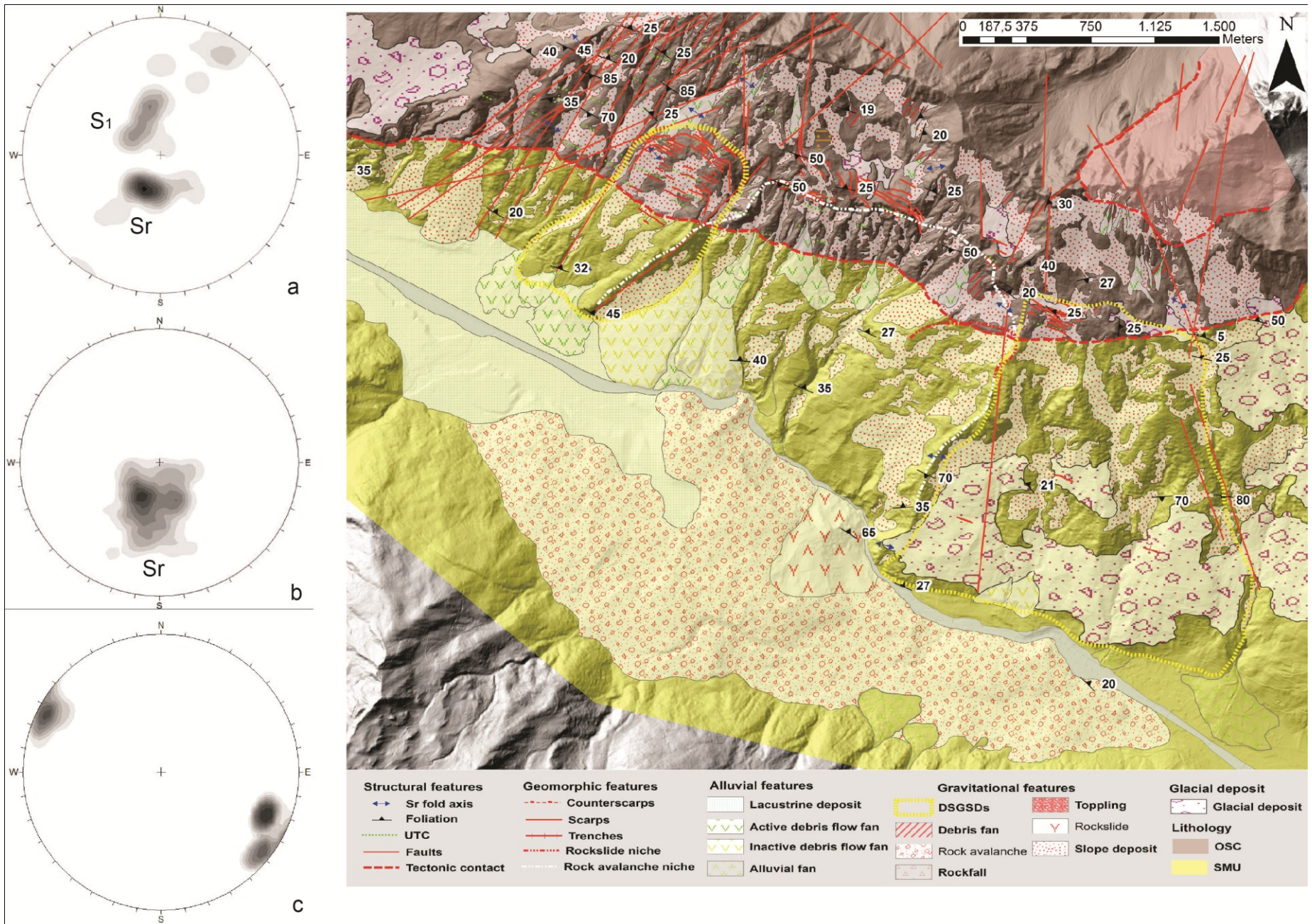


Fig. 4.5



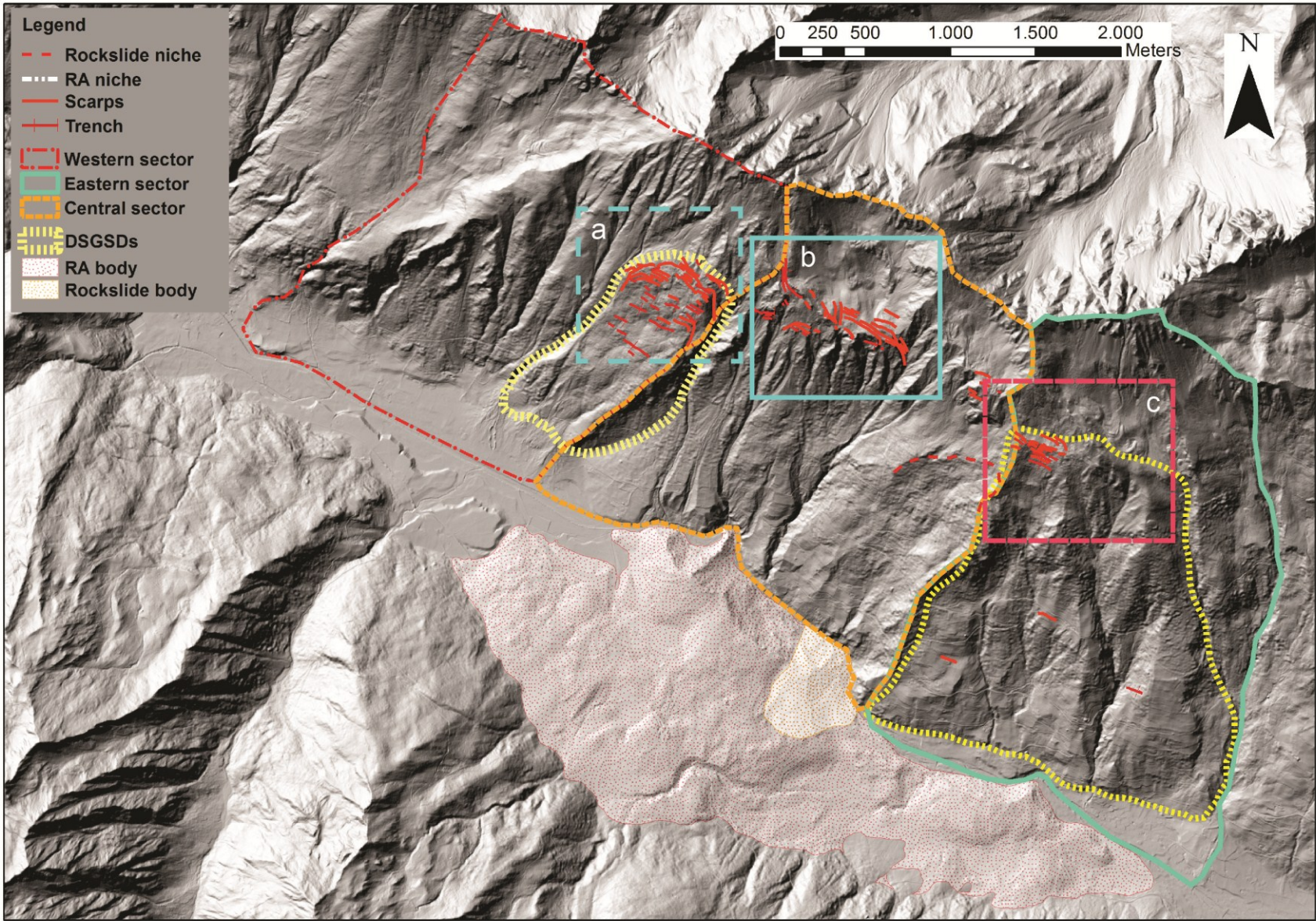
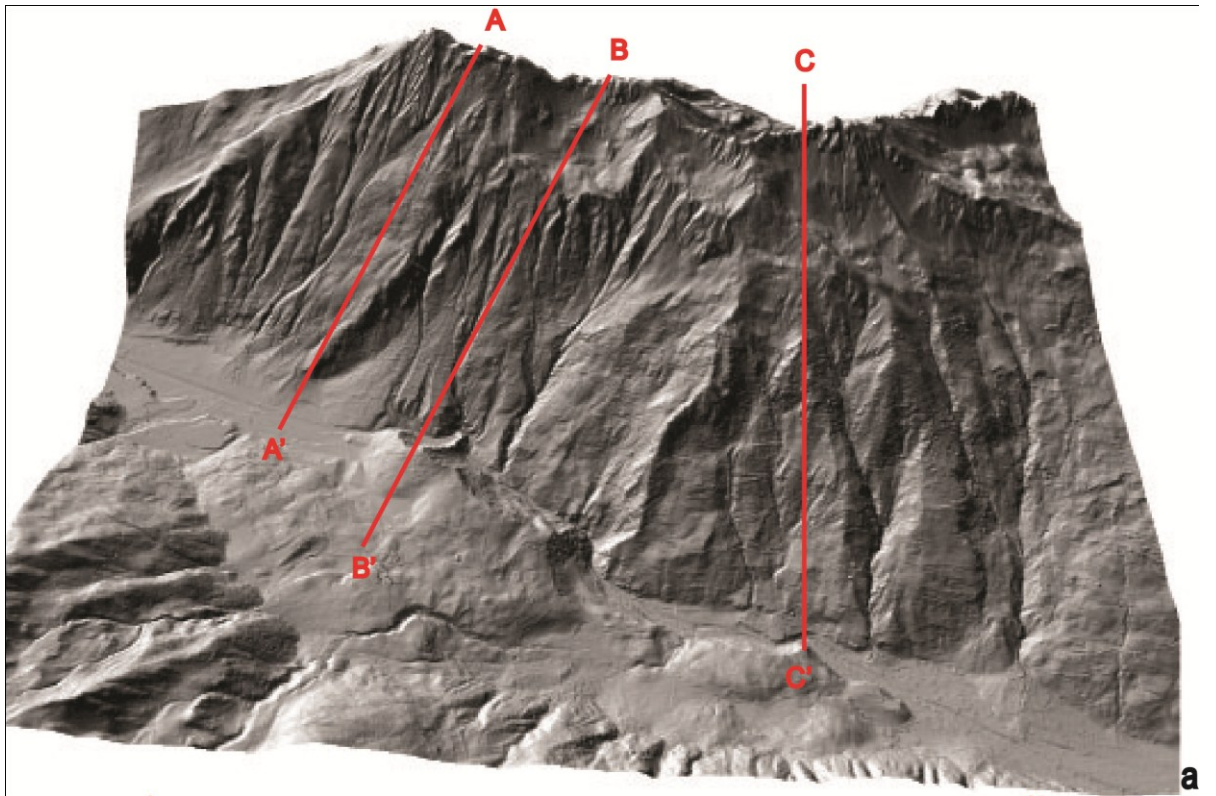
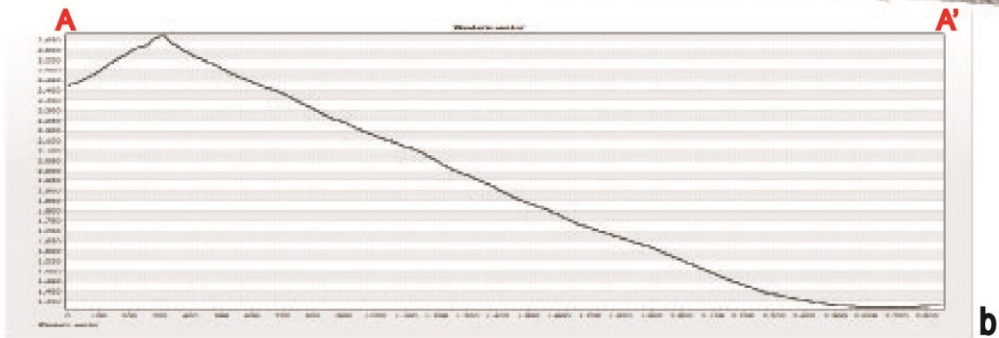


Fig. 4.6

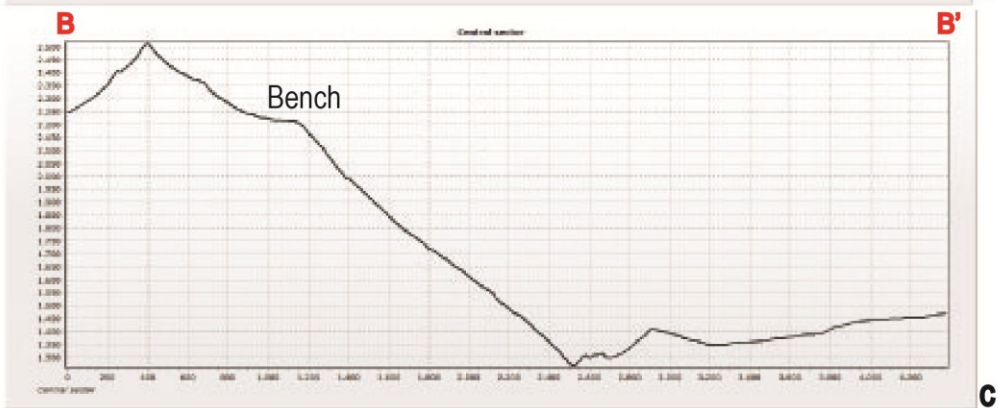




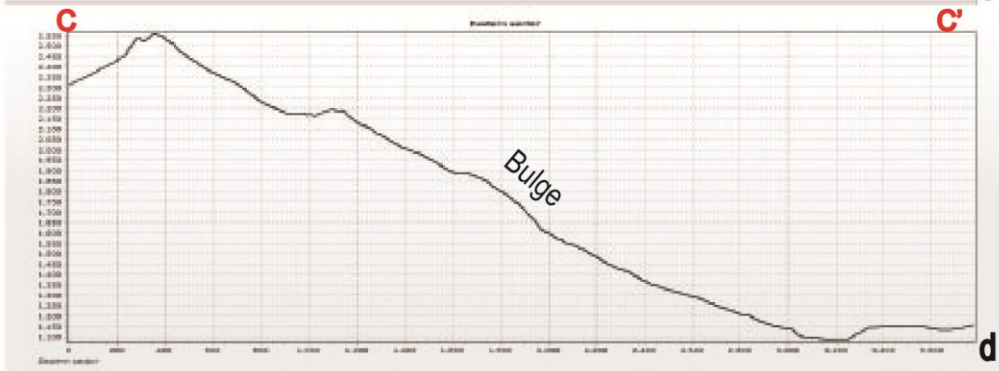
a



b



c



d

Fig. 4.7



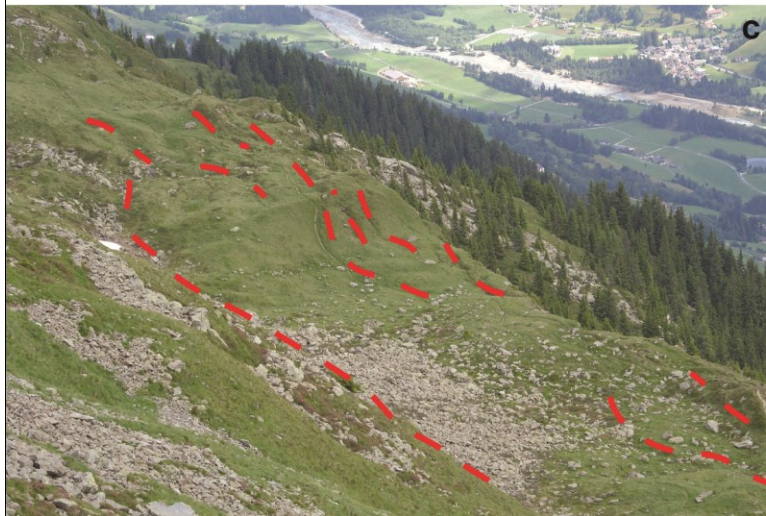


Fig. 4.8





Fig. 4.9

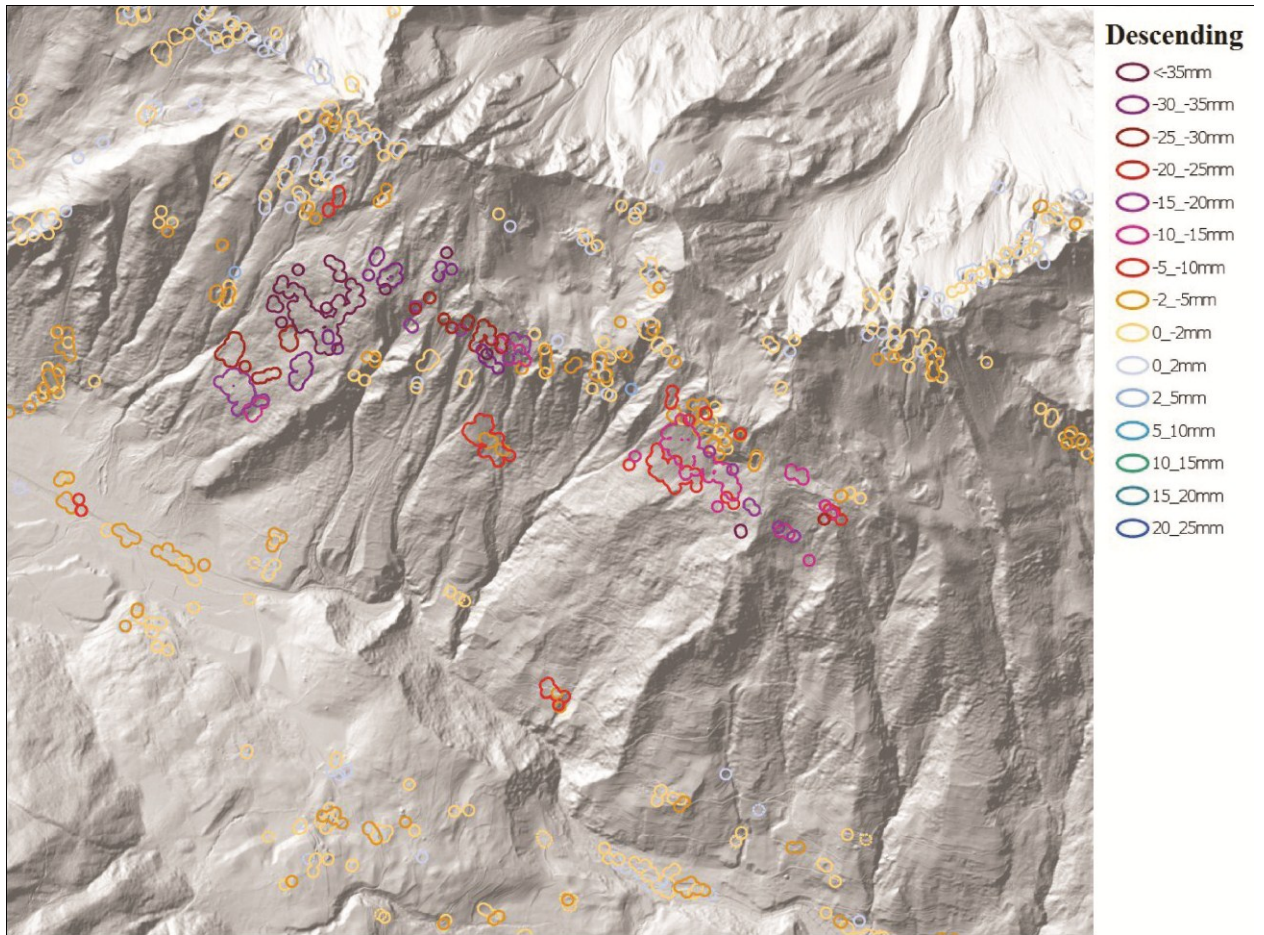


Fig. 4.10



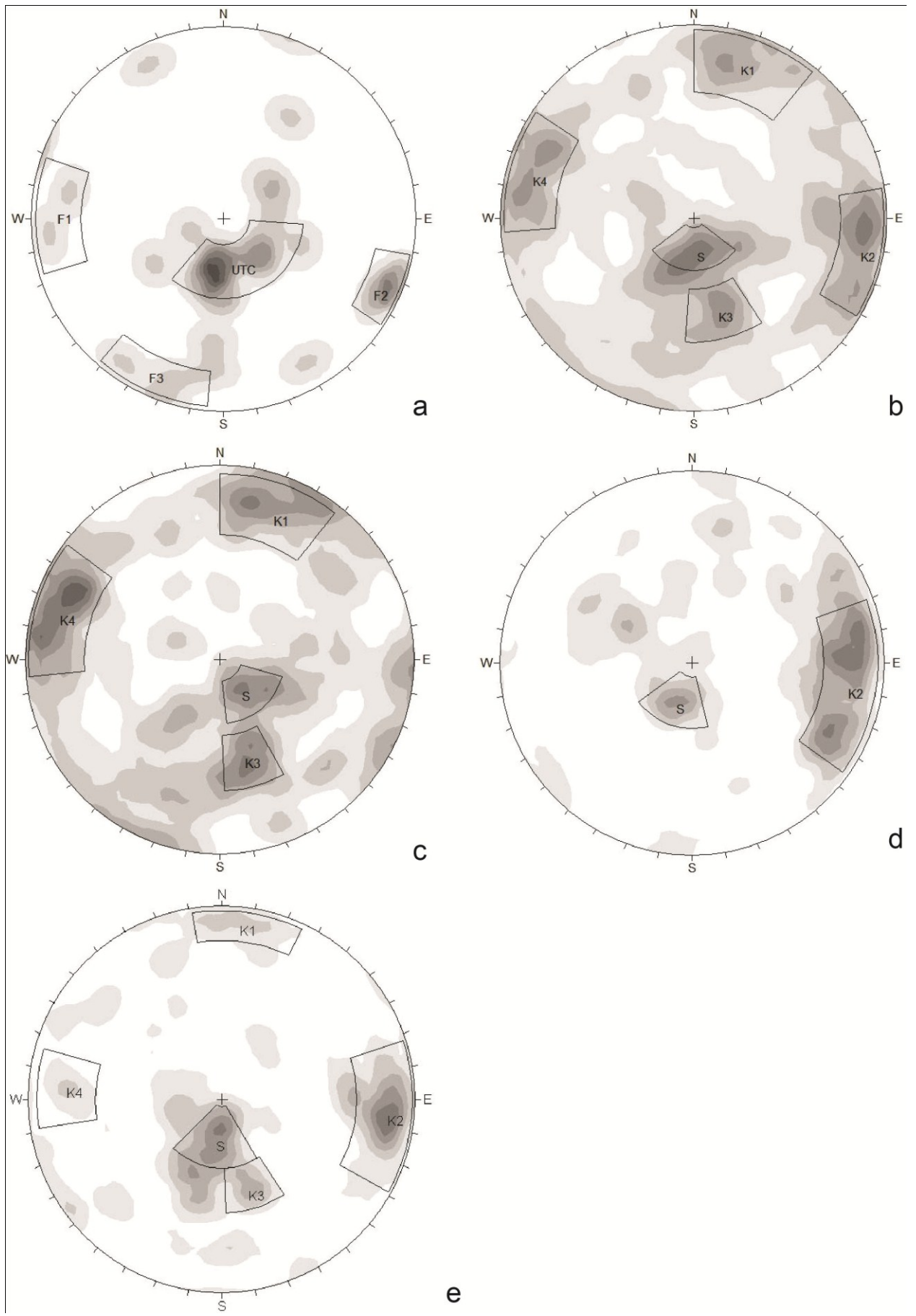
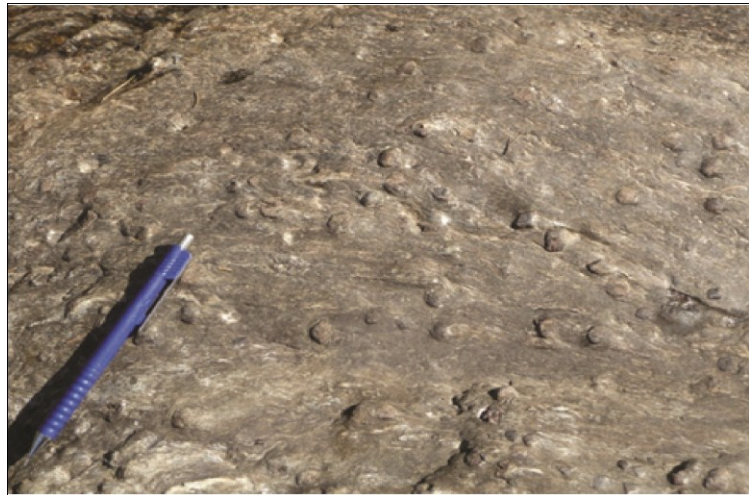


Fig. 4.11





a



b



c



d



e

Fig. 4.12



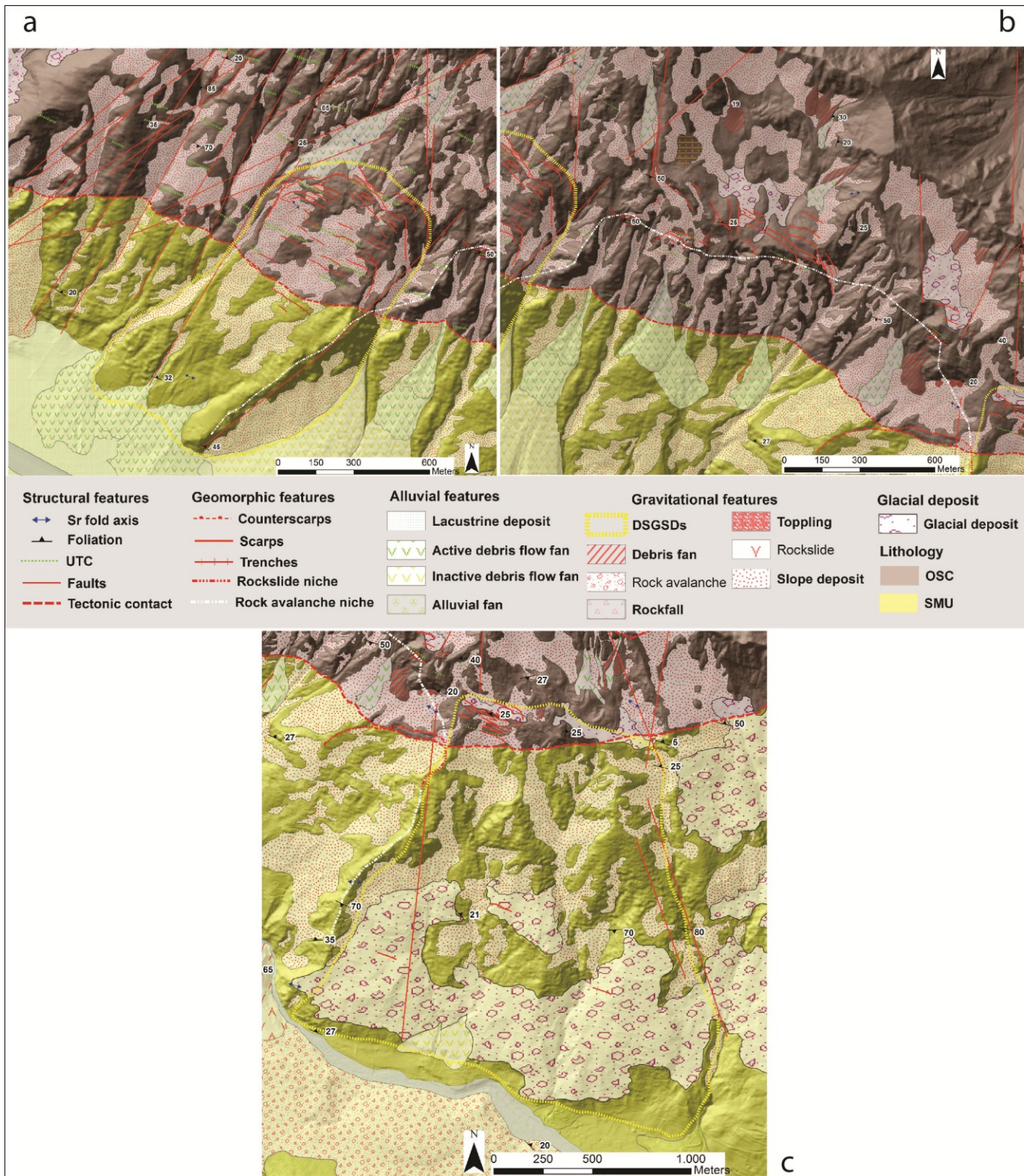


Fig. 4.13

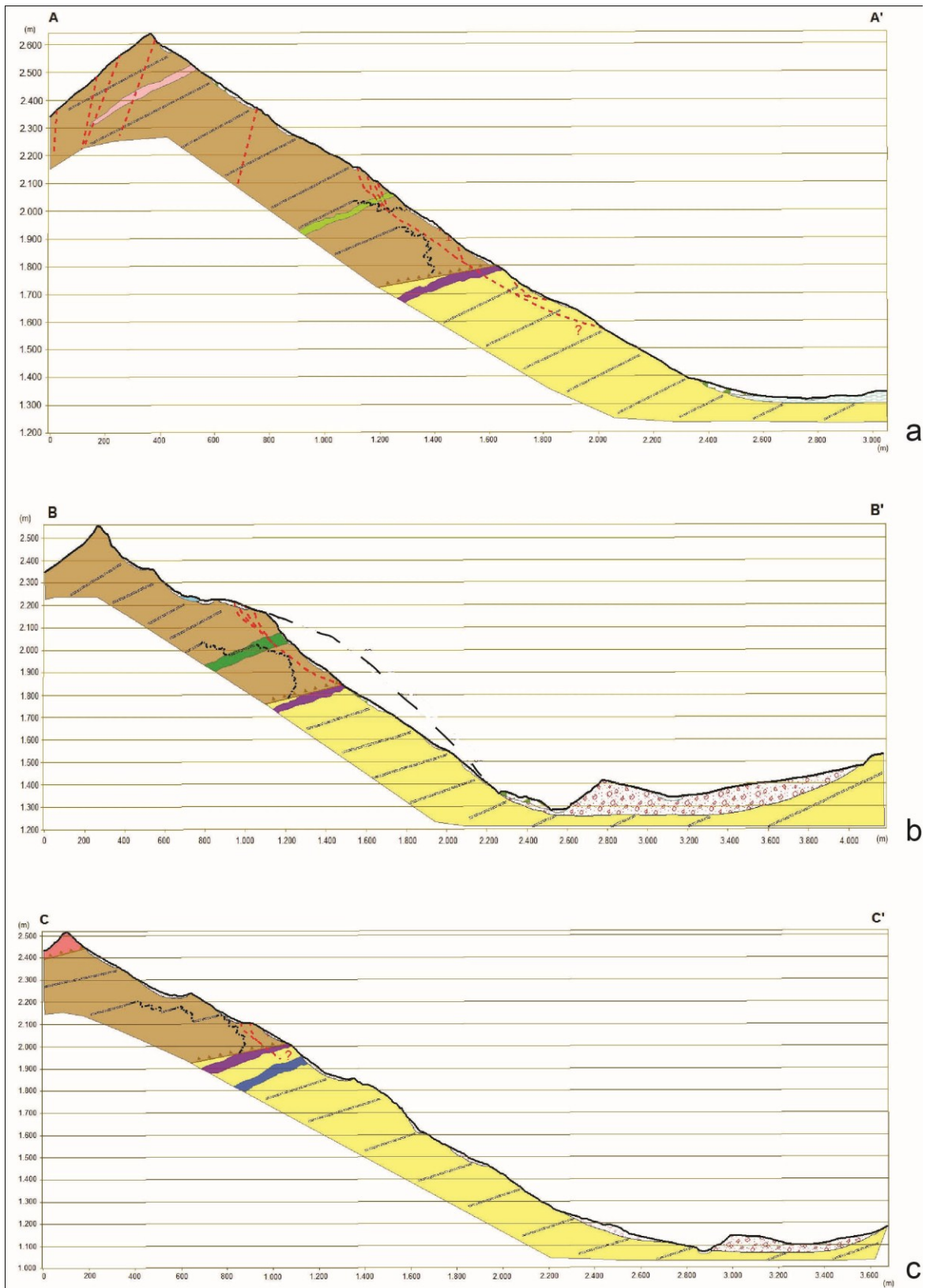


Fig. 4.14

# 5. Rock mass properties

Luca Zorzi, Lorenzo Flaim, Fabio Ferri, Rinaldo Genevois.

## 5.1 Introduction

Rock mass is to be considered as a matrix consisting of rock blocks and fragments separated by discontinuities forming a material in which all elements behave in mutual dependence as a unit (Palmstrom, 2010). Hence, rock mass mechanical properties are governed by properties of intact rock material and the discontinuities.

Reliable estimates of strength and deformation characteristics of rock masses are required for almost any form of analysis used for slope stability analysis, design of slopes, foundation and underground excavation (Hoek and Bray, 1977; Willye and Mahr, 2005; Palmström and Stille, 2010). According to Palmström (2001), rock mass parameters like degree of jointing (density, orientation and pattern of joints), joint characteristics (joint roughness, joint condition or alteration) and intact rock material through which the joint intersect (strength and elastic properties of the rocks, rock anisotropy, rock durability, mineralogic content) have the strongest impact on behavior and strength properties of the rock mass. Thus, a complete characterization of both discontinuities and intact rock are required to evaluate qualitatively and quantitatively strength and deformation characteristic of rock masses. Rock mass classification systems constitute an integral part of slope stability analysis.

After a brief recall of the geomechanical data acquired during field survey and presented on chapter 4, in this chapter the mechanical properties of both discontinuities and intact rock, evaluated through the field and laboratory methodologies presented on chapter 2, will be presented.

## 5.2 Discontinuity characterization

Geomechanical surveys were carried out in order to collect information about the physical properties of the rock mass and discontinuity sets (Fig. 4.3). Scanline surveys were done to systematically characterize the discontinuities sets providing the fundamental parameters needed for the geomechanical characterization of rock mass, such as orientation, persistence, spacing and termination of the discontinuities as well as Joint wall Compressive Strength (JCS) and Joint Roughness Coefficient, (JRC) (Willye and Mahr, 2005).

As stated in chapter 4, a total number of 45 geomechanical stations (20 scan-line type and 25 “random” type) were performed trying to cover all the sectors and lithologies characterizing the studied area. Locally, scan-line having a total length less than 5m was performed due to the reduced extension of the available outcrops.

The spatial distribution of the geomechanical station is not uniform among the slope (Fig. 4.3). Presence of widespread thick Quaternary cover hiding the bedrock, coupled with outcrops located in highly hazardous areas due to rockfalls and toppling, made locally difficult to find available and useful outcrops for geomechanical investigation, like in the Central sector of the slope (Fig.4.3).

more than 1000 discontinuities were measured during the field surveys and the following faults and joint sets were recognized (Fig.4.11):

- a NW-SE striking set dipping towards the SW (average dip =  $70^\circ$ ), named K1;
- a N-S striking set dipping towards the W (average dip =  $75^\circ$ ), named K2;
- a WNW-ESE striking set dipping towards the NW (average dip =  $45^\circ$ ), named K3;
- a N-S striking set dipping towards the E (average dip =  $75^\circ$ ), named K4;
- a E-W striking set gently dipping towards the N (average dip =  $14^\circ$ ), named S because it follows the regional foliation defining the fabric of the bedrock units.

As already presented on chapter 4, the detected sets are not present continuously in all the three sectors. The Eastern sector is characterized by all 5 discontinuity sets, whereas in the Western sector the K2 systems is missing or only sporadically present (Fig.4.11). The Central sector is the one showing a completely different brittle setting, because only K2 and S sets were detected (Fig. 4.11).

### 5.2.1 Spacing

A total number of 440 spacing data were collected during the geomechanical survey. The different joint sets show homogeneous spacing distribution both among the entire slope (Fig 5.1). In fact, mean values of 20 – 30 cm characterize all the joint sets (table XX). S joint set is characterized by a very low spacing, ranging from 4 to 10 cm, which are strongly controlled by the mm – spaced foliation.

### 5.2.2 Joint compressive strength (JCS) and Joint roughness coefficient (JRC)

A total number of 480 data regarding the Joint compressive strength (JCS) were acquired in the field. Splitting the data to complexes, differences arise in terms of JCS values between SMU and ÖSC (Fig. 5.1). Clear differences between the two bedrock



complexes arise considering the JCS values. JCS values of the SMU show mean low values, between 10-40 MPa, whilst ÖSC is defined by higher JCS values ranging from a minimum of 40 MPa to a maximum of 100 MPa.

Highest values acquired on SMU complex are due to quartzitic levels that can be detected within this complex (see chapter 4). No relevant trend is highlighted along the slope, indicating homogenous values within the SMU.

Data related to ÖSC complex are much more scattered respect to the one of the SMU (Fig. 5.1). The dispersion of the data seems not to be related to the different rock types defining the ÖSC. In addition, JCS values within the ÖSC seem to be affected by an E – W diminishing trend along the slope, independently from rock type and lithology among the OSC (Fig. 5.1). This trend is interpreted to be the effect of surficial weathering of joint surfaces involving the ÖSC. In fact, the ÖSC lithologies on the Easter sector of the slope are interested by diffuse stratabound sulphides mineralization. Thus, acid surficial waters may induce intense weathering especially on outcropping joint surfaces, causing the decrease of JCS values.

When possible, JRC values were acquired on discontinuity surface, and the mean values of each discontinuity set are listed on table 5.1. Considering the JRC of the same joint set, an increase trend going from the Western sector to the Eastern sector is highlighted.

### **5.3 Rock mass classification**

Rock Quality Designation index (RDQ; Deere and Miller, 1966), Rock Mass Rating (RMR; Bieniawski, 1976), and the Q index (Barton, 1974, 2002) for rock mass classification were evaluated for each geomechanical station. Average values of RMR rate and Q index made possible to obtain, through empirical correlation geomechanical properties of the rock mass, such as rock mass Young modulus, rock mass cohesion and rock mass friction angle, fundamental for a complete characterization of the rock mass and for further numerical simulations (Hoek and Brown, 1980; Bieniawski 1989; Barton, 2002; see chapter 2). Complete list of rock mass characterization for each station is presented on table 5.1 and 5.2.

#### *5.3.1 Geological strength index*

As stated in chapter 4, a value of the Geological Strength Index (GSI) was evaluated and assigned to each mapped outcrop during the field work. The GSI, introduced by Hoek (1994), Marinos and Hoek (2000), provides a system for estimating the reduction in rock mass strength for different geological conditions as identified by field

observations (Hoek et al., 1998). Rock mass strength is assigned by ready field observations of the rock mass structure and the conditions of fractures planes, in terms of roughness and alteration (Hoek et al., 1998; Marinos and Hoek, 2000). The combination of these two parameters allows the estimation of GSI values by mean of contours given by the GSI tables proposed by Hoek (1994), Hoek et al. (1998), Marinos and Hoek (2000). In specific, for this work the updated version of the GSI table proposed by Marinos and Hoek (2000), which accommodates the effect of schistosity and shear planes, was used. A GIS-based contour map of the GSI values, using ArcGis 9.3, assigned to all mapped outcrops was then created to evaluate the spatial distribution and possible variability of the values (Fig.4.4).

GSI contour maps do not show any clear E-W trend, whereas discrete NE-SE trend are highlighted from the GSI distribution (Fig.4.4). Lowest GSI values are located on areas affected by rock slope instabilities, in which gravity-driven geomorphic structures increase the degree of fracturing of the rock masses (Fig. 4.4). Low GSI values characterize the Western sector of the slope. This cluster is caused by the intense fracturing resulting from the fault network (see paragraph 4.7) that intensely involves this sector of the slope.

Comparing the GSI distribution in the Western and Eastern sector by plotting the values on histogram graphs, and separating them between the two complexes, no relevant differences are highlighted (Fig. 5.2). In fact, the differences in GSI within the same complex in the two sectors are due to statistic and sampling reasons than for structural reason. In addition, the lowest values showed by the ÖSC in the Eastern sector respect to the one of the SMU depend uniquely from the location and availability of outcrops: in fact, useful outcrops are located in areas interested by gravitational geomorphic features (mainly scarps and trenches) that increase the degree of fracturing of the rock mass, decreasing the GSI. Indeed, the GSI values are not useful to investigate the pre – deformed gravitational setting of this sector of the slope.

#### **5.4 Intact rock characterization**

Laboratory tests allow the reconstruction of the stress – strain behavior and the main mechanical properties of the intact rock, as well as the observation of the fracture geometry and patterns on testes samples (for this lasts, see chapter 7).

Rock strength and elastic constants such as Young's Modulus and Poisson's ratio are fundamental for numerical simulation on the trigger and evolution of a slope deformation.

Elastic properties and strength parameters of intact rock can be obtained through static methods, where the rock is gradually loaded in uniaxial, biaxial (conventional triaxial) or triaxial compression up to failure. Lateral and axial strains are measured constantly during the tests as a function of the applied stresses.

Point load tests, uniaxial compressive tests and triaxial tests were performed to characterize the lithologies constituting the metamorphic complexes outcropping in the Ridnaun Valley.

Samples used for the tests were collected during field work, mainly on sites where geomechanical stations were performed (Fig. 4.3).

#### 5.4.1 Point load tests

Uniaxial compressive strength (UCS) has always been considered to be one of the most important rock mechanical properties in rock engineering. As uniaxial compression tests required highly machined samples (see chapter 2), index tests such as the point load test required little or no specimen preparation. Despite the handiness of sample preparation and tests execution, point load test provide a useful estimation of UCS (Brook, 1985; Cargill and Shakoor, 1990; Ghosh and Srivastava, 1991; Chau and Wong, 1996; Basu, 2008; Basu and Kamran, 2010).

As explained on chapter 2, the point load index was calculated using the following equations (Basu and Kamran, 2010):

$$I_{S50} = F \times \frac{P}{De^2} \quad (\text{Eq. 2.11})$$

$$F = \sqrt{\frac{De}{50}} \quad (\text{Eq. 2.12})$$

$$De^2 = 4A/\pi \quad (\text{Eq. 2.13})$$

$$A = W \times D \quad (\text{Eq. 2.14})$$

Where F is the size correction factor,  $I_{S50}$  is the uncorrected point load strength, De is the equivalent core diameter, P is the applied load, A the minimum cross sectional area of a plane through the platen contact points. W and D are block dimensions.

To calculate the UCS values starting from Point load index, the relation proposed by Basu and Kamran (2010) was used:

$$UCS = 11.103 I_{S50} + 37.659 \quad (\text{Eq. 2.15})$$

Point load tests have been performed on samples belonging to the gneisses of the ÖSC (45 samples) and the garnet – micaschists of the SMU (15 samples). For the point load



tests, samples were tested parallel and perpendicularly to the rock fabric. The results are summarized in tables 5.3 and 5.4.

#### 5.4.2 Uniaxial compression tests

The uniaxial compressive strength of a rock is defined as the value of the peak stress sustained by rock specimen subjected to uniaxial compression, denoted as UCS or  $\sigma_c$  and expressed in MPa (Tang and Hudson, 2010). Values obtained from testing depends on the size, shape and other conditions of the tests procedures.

The rock type chosen for uniaxial compressive tests are the following:

- gneisses of the ÖSC,
- garnet micaschists, marble and quartzites of SMU.

Cylindric samples tested in this work had diameters of 38 mm and 25 mm, and a length to diameter ration between 2.0 and 2.5 according to the ASTM – D7012 (2010) and ASTM – D4543 (2008) specification. The value of constant loading rate used for the test is 0.200 MPa/s. Young’s Modulus was calculated as tangent modulus ( $E_{\tan 50}$ ) and secant modulus ( $E_{\sec 50}$ ) at 50% of the maximum load, on the linear portion of the loading curve. A pre-load of about 8-10 kN is automatically applied by the system, and unfortunately it cannot be changed. Thus, it may be possible that the “bedding down” or “initial crack closure” (Tang and Hudson, 2010) portion of the stress – strain curve cannot be recorded during the test.

On foliated lithologies, such as gneisses of the ÖSC and garnet – micaschists of the SMU, tests were performed with different  $\beta$  angle with respect to the metamorphic fabric. Three different  $\beta$  values were considered:  $0^\circ$  (foliation parallel to the load direction),  $90^\circ$  (foliation perpendicular to the load direction), and,  $30^\circ$ . Due to the extreme fissility of the foliated rock types, especially the garnet – micaschists, the number of samples on which tests with an inclined  $\beta$  were performed is less than the one for the other angles (see table 5.5 and 5.6, Fig. 5.3). For the sample RD180, due to issues in drilling the sample with the good orientation, tests with  $\beta = 75^\circ$  were performed (table 5.5 and Fig. 5.3)

In Fig.5.4 and 5.5, stress – strain curves for lateral strain  $\varepsilon_r$ , vertical strain  $\varepsilon_h$ , and volumetric strain  $\varepsilon_v$  relative to the major lithologies detected during field work are reported.

To calculate the volumetric strain  $\varepsilon_v$ , the following equation was used:

$$\varepsilon_v = \varepsilon_h + 2\varepsilon_r \quad \text{eq. 5.1}$$

where  $\varepsilon_h$  is taken positive and  $\varepsilon_r$  is taken negative.

The results obtained from uniaxial compressive tests, in terms of UCS, Young's modulus and Poisson ratio, are listed in table 5.5 and 5.6. Fracture characterization of the rock sample is not discussed in this chapter because it will be presented in detail in chapter 7.

As stated in chapter 4, the mechanical behavior of the described rock slope instabilities is governed by the behavior of the gneisses of the ÖSC and of the garnet – micaschists of the SMU. Thus, a discussion focused on these two units will be present in this paragraph. Hints will be given to the other rock type tested.

It is noteworthy the fact that values of UCS and E of  $\beta = 0^\circ$  tests are quite often higher than the one of  $\beta = 90^\circ$ . This is contrast with published data about uniaxial compressive tests in anisotropic foliated rocks (Behrestaghi et al., 1996; Nasser et al., 1997; Agliardi et al., 2010). This behavior is testified also by the plots UCS/ $E_{\tan 50}$  of figure 5.6 and figure 5.7. More specifically, if considering the plot of the Schneeberg Unit (fig. 5.7),  $\beta = 90^\circ$  samples has E values systematically lower than the one with  $\beta = 0^\circ$ .

Taking into consideration now figure. 5.3, both ÖSC gneisses and SMU garnet – micaschists are defined by higher failure strength for  $\beta = 0^\circ$  and  $90^\circ$ , and lower for  $\beta = 30^\circ$ . This behavior follows the one indicated by different authors (Deklotz et al., 1966; McCabe and Koerner, 1975; Akai, 1971; Ramamurthy, 1993; Nasser et al., 1997; Behrestaghi et al., 1996). The shapes of the curves between the uniaxial compressive strength and the orientation angle  $\beta$  suggests a type of anisotropy namely U – shaped (Ramamurthy, 1993) for the garnet micaschists of the SMU (Fig. 5.3b) and a “shoulder” shape (Ramamurthy, 1993) for the gneiss of the ÖSC (Fig. 5.3a).

Considering the stress – strain curves of ÖSC specimens, they show high E values, steep stress – strain curves indicating a stiff material with a purely brittle behavior (Fig. 5.6 and Fig.5.7), which seems to be independent from  $\beta$ .

SMU samples show different type of rock failure related to  $\beta$ . On one hand, the geometry of stress – strain curves of  $\beta = 30^\circ$  and  $\beta = 90^\circ$  samples, coupled with relative low E values, indicate a compliant or soft rock (Gudmundsson, 2011) with a predominantly brittle failure. On the other hand,  $\beta = 0^\circ$  samples stress – strain curves, with their steeper curves and higher E values, indicate a stiffer rock characterized by a predominantly strain – softening behavior. In fact, the post – peak region of the loading curves indicated a decreasing load – bearing capacity of the specimen (Fig. 5.6 and 5.7). The irregular geometry of the load curve especially in the post – peak region is to be interpreted as the indication of micro – structures break down. The stress drop recorded

in the post – peak region is related to energy release due to micro – cracks clustering into macroscopic fractures leading to the eventual failure of the sample (Tang and Hudson, 2010; Gudmundsson, 2011).

## 5.5 Geomechanical domains

Starting from the geomechanical data collected in the field, allows the subdivision of the slope into five discrete geomechanical domains (Fig. 5.8). Starting from the three geomorphologic sectors described on chapter 4, other three domains were added in order to highlight the differences in mechanical parameters between the ÖSC and SMU complexes. The domains are named:

- Western sector – ÖSC
- Western sector – SMU
- Central sector – ÖSC
- Central sector – SMU
- Eastern sector – ÖSC
- Eastern sector – SMU

Due to the lack of geomechanical station in the SMU part of the Central sector, the central sector of the slope will be considered as constitute only by one domain.

Table 5.7 presents the characteristics of the principal joint listed by domain. The base friction angle  $\phi_b$  assigned to each domain was chosen from the values proposed by Barton and Choubey (1977). To simplify the analysis, the ÖSC was consider to be made entirely by gneiss rock type and the SMU made uniquely by garnet – micaschists.

Comparing the domains in the Western sector with the one in the Eastern sector, a general decreasing trend of mechanical parameters can be seen. The presence of sulphides mineralized levels, clustered mainly on the ÖSC lithologies of the Eastern sector, may induce the formation of acid waters that may induce intense weathering on outcropping bedrock units, resulting in a decrease in mechanical properties. This interpretation seems to be sustained by the geoemchanical analysis made on the rockslide body found within the rock avalanche deposit. Geomechanical stations performed in this area (Fig. 4.3) show higher values, in terms of JCS, respect to the lithologies located in the Western sector. Indeed, this rock units involved in the rockslide, were bring to surface only after the rock failure, so exposed to surficial weathering since less time respect to the rock units investigated on the slope.

In order to evaluate the shear strength along the discontinuities, the Barton and Choubey (1977, chapter 2) was applied (table 5.8). Considering one joint set, the result show an

W to E increasing trend in term of shear strength, caused by the W to E increase of JRC (table 5.1).

Looking at the rock mass classification systems used (table XX), SRM values are located between 45 and 72, indicating a fair to good rock mass. On the contrary, Q – system values range from 1 to 9 within all the stations, indicating fair to poor rock masses.

Average values of RMR rate and Q index made possible to obtain, through empirical correlation geomechanical properties of the rock mass, such as rock mass Young modulus, rock mass cohesion and rock mass friction angle, were calculated. In table 5.8 only the parameters calculated starting from the Q – system are listed. The data calculated using the RMR were discarded, because of the unrealistic values especially concerning the rock mass cohesion ( $c = 0.2 - 0,4$  MPa; table 5.8).

In addition, starting from the GSI values assigned in the field to each mapped outcrops it was possible to estimate rock mass mechanical properties using the RockLab software (Rocscience, 2008). The estimated values are listed on table 5.9.

The calculated rock mass mechanical parameters starting from the Q – system and the GSI were used as starting input values for the back – analysis of the Ridnaun Rock avalanche using numerical modeling techniques (see chapter 6).

STOP	Structural complex	Rock type	n° Joint set	Attitude		Spacing (m)	JRC	JCS (MPa)	RMR <sub>b</sub>	φ (°)	C (MPa)	E (MPa)	SMR	GSI	Calculated GSI
				Dip Dir	Dip										
GMRD01	Monteneve	Garnet-micaschist	4	187	74	0,16	10-12	62,7	42	26,0	0,21		57		37
				347	18	0,16		139,9							
				112	69	0,62		102,0							
				083	75	1,15		53,6							
GMRD02	Monteneve	Garnet-micaschist	3	344	36	0,19		49,3	39	24,5	0,19		46	40-45	34
				102	74	0,91		113,3							
				302	23	0,46		41,8							
GMRD03	Monteneve	Garnet-quartzite	5	281	47	0,02		93,9	57	33,5	0,28	14000	71	50-55	52
				338	40	0,51		98,0							
				161	76	1,32		58,9							
				306	31	0,12		96,5							
				039	86	0,52		117,6							
GMRD04	Oetztal-Stubai	Garnet-paragneiss	6	230	88	0,22	12-14	114,7	54	32	0,27	8000	61	35-40	49
				265	38	0,38		61,6							
				235	22	0,18		122,1							
				021	87	0,21	69,0								
				086	71	0,34	161,3								
				337	65	0,39	10-12	131,4							
GMRD05	Oetztal-Stubai	Garnet-paragneiss	5	317	15	0,01		94,6	47	28,5	0,23		62	40-45	42
				180	76	0,69		147,7							
				030	86	0,40		164,8							
				081	49	1,88		87,4							
				078	81	1,89		116,4							
GMRD06	Oetztal-Stubai	Garnet-paragneiss with amphibole	6	037	29	0,25		35,6	50	30	0,25		64	25-30	45
				014	63	0,26		49,8							
				094	61	0,02		96,8							
				155	55	0,79		97,3							
				340	38	0,23		39,1							
				296	79	0,44		79,5							
GMRD07	Oetztal-Stubai	Garnet-paragneiss	4	258	77	0,11		85,1	54	32	0,27	8000	68	50-55	49
				031	20	0,11		79,3							
				296	71	1,31		100,0							
				206	38	0,19		33,3							
GMRD08	Oetztal-Stubai	Garnet-paragneiss	3	267	65	0,23		62,8	49	29,5	0,24		64	35-40	44
				139	26	0,55		19,5							
				235	60	0,47		76,9							

STOP	Structural complex	Rock type	n° Joint set	Attitude		Spacing (m)	JRC	JCS (MPa)	RMR <sub>b</sub>	φ (°)	C (MPa)	E (MPa)	SMR	GSI	Calculated GSI
				Dip Dir	Dip										
GMRD09	Monteneve	Garnet-bearing graphitic micaschist	4	275	70	0,17		38,6	50	30	0,25		65	35-40	45
				163	86	0,12		44,4							
				056	20	0,45		7,0							
				356	66	0,09		27,2							
GMRD10	Monteneve	Sericitic garnet-micaschist	3	023	35	0,10		17,2	37	23,5	0,18		51	25-30	32
				178	78	0,34	18-20	29,1							
				116	79	0,15		40,7							
GMRD11	Monteneve	Quartzite	4	293	31	0,08		33,5	49	29,5	0,24		58	35-40	44
				133	77	0,60		47,0							
				360	54	0,23	8-10	28,5							
				214	57	0,70	6-8	56,7							
GMRD12		Garnet-micaschist	7	008	64	0,34	14-16	40,6	47	28,5	0,23		58	35-40	42
				345	74	0,16	8-10	68,1							
				198	63	0,20		85,6							
				189	85	0,65		74,4							
				228	85	0,36		81,2							
				295	67	0,27	10	64,5							
				102	58	0,22	8-10	41,3							
RDL01	Oetztal-Stubai	Garnet-paragneiss	6	005	11										
				338	55			65,0							
				030	25			96,5							
				243	65			22,5							
				113	52			63,0							
				095	48			23,5							
RDL02	Oetztal-Stubai	Ultracataclasite level		330	74			13,5							
RDL03	Oetztal-Stubai	Ultracataclasite level		351	30			7,0							
RDL04	Oetztal-Stubai	Ultracataclasite level		344	10			93,5							
RDL05	Oetztal-Stubai	Micaschist paragneiss	6	016	17										
				190	15			100,0							
				087	88	0,45		100,0							
				170	40	0,25		49,0							
				198	55			90,5							
				290	70			100,0							

STOP	Structural complex	Rock type	n° Joint set	Attitude		Spacing (m)	JRC	JCS (MPa)	RMR <sub>b</sub>	φ (°)	C (MPa)	E (MPa)	SMR	GSI	Calculated GSI
				Dip Dir	Dip										
RDL06	Oetztal-Stubai	Garnet-paragneiss	6	007	25										
				315	88			40,0							
				085	71			72,5							
				027	20			100,0							
				330	16			11,0							
				200	70			31,5							
RDL07	Oetztal-Stubai	Quartzitic paragneiss	5	111	12			14,5							
				134	66			43,0							
				264	55			73,0							
				211	88			59,0							
				242	25			20,5							
RDL08	Monteneve	Garnet-micaschist	7	299	10										
				351	31			7,0							
				049	71			38,0							
				305	75										
				330	85			28,5							
				263	70			47,0							
				195	82			35,0							
RDL10	Monteneve	Garnet-micaschist	5	338	32									30-35	
				100	81			7,0							
				055	42			39,0							
				304	41			14,5							
				207	58			88,0							
RDL12	Monteneve	Garnet-micaschist	6	285	20									35-40	
				046	87			74,5							
				187	72			53,0							
				011	77			40,5							
				294	11			44,5							
				264	73			59,0							
RD136	Oetztal-Stubai	Garnet-paragneiss		340	20			80,1						40-45	
RD142	Oetztal-Stubai	Ultracataclasite level						133,9							

Table 5.1: geomechanic data collected during geomechanical surveys. In this table, RMR and SRM rock mass classification are presented.

WPT	Lithology	RQD (%)	RMR <sub>b</sub>	φ (°)	c	E <sub>m</sub>	Q	FC	CC	E <sub>m</sub>	SMR	GSI
		Deere			(MPa)	(MPa)	Index	(°)	(MPa)	(GPa)		
GMRD01	Garnet micaschist	95,1	59	34	0,29	17000	1,3	22	3,2	10,8	54	25-30
							Poor				Fair	
GMRD02	Garnet micaschist	94,4	49	29	0,24	17700	4,9	34	7,3	17,0	45	35-40
							Fair				Fair	
GMRD03	Quartzite	93,5	65	38	0,32	30600	7,2	56	4,8	19,3	72	40-45
							Fair				Good	
GMRD04	Garnet paragneiss	85,1	59	34	0,29	17800	3,4	33	5,2	15,1	59	35-40
							Poor				Fair	
GMRD05	Paragneiss	94,7	55	33	0,28	10400	5,6	31	9,3	17,7	59	35-40
							Fair				Fair	
GMRD06	Paragneiss	77,1	60	35	0,30	19200	3,9	45	3,9	15,7	64	25-30
							Poor				Good	
GMRD07	Paragneiss	86,0	59	34	0,29	17200	2,9	56	2,0	14,3	70	35-40
							Poor				Good	
GMRD08	Garnet paragneiss	89,6	56	33	0,28	12400	4,4	37	5,8	16,3	65	35-40
							Fair				Good	
GMRD09	Garnet graphitic micaschist	74,4	54	32	0,27	8600	1,3	34	1,9	10,8	66	25-30
							Poor				Good	
GMRD10	Centimetric garnet micaschist	79,6	53	31	0,26	5600	1,5	37	2,0	11,4	50	25-30
							Poor				Fair	



WPT	Lithology	RQD (%)	RMR <sub>b</sub>	φ (°)	c	E <sub>m</sub>	Q	FC	CC	E <sub>m</sub>	SMR	GSI
		Deere			(MPa)	(MPa)	Index	(°)	(MPa)	(GPa)		
GMRD11	Quartzitic micaschist	87,7	62	36	0,31	23800	3,0	45	3,1	14,5	55	35-40
							Poor				Fair	
GMRD12	Centimetric garnet micaschist	81,8	59	34	0,29	17200	1,7	37	2,2	11,8	56	35-40
							Poor				Fair	
GMRD13	Quartzitic micaschist	94,6	65	37	0,32	29400	1,9	45	1,9	12,3	28	35-40
							Poor				Poor	
GMRD14	Paragneiss	91,8	60	35	0,30	20200	3,3	45	3,3	14,9	18	30-35
											Very	
							Fair				Poor	
GMRD15	Centimetric garnet micaschist	92,0	54	32	0,27	7600	1,3	37	1,7	10,9	58	40-45
							Poor				Fair	
GMRD16	Centimetric garnet micaschist	93,2	59	35	0,29	18000	1,5	45	1,5	11,3	36	30-35
							Poor				Poor	
GMRD17	Centimetric garnet micaschist	87,5	65	38	0,32	30000	0,8	45	0,8	9,2	53	30-35
							Very					
							Poor				Fair	
GMRD18	Centimetric garnet micaschist	56,9	53	32	0,27	6400	0,6	34	0,9	8,3	61	25-30
							Very					
							Poor				Good	
GMRD19	Centimetric garnet micaschist	86,8	58	34	0,29	15600	4,1	45	4,1	16,0	69	30-35
							Fair				Good	
GMRD20	Amphibolic gneiss	86,4	69	40	0,35	38600	8,5	45	8,5	20,4	51	35-40
							Fair				Fair	

Table 5.2: geomechanical characterization of the 20 scan line type surveys.

ÖSC	n. test	lithology	type of test	direction	P (N)	D (mm)	D' (mm)	W (mm)	D <sub>e</sub> (mm <sup>2</sup> )	F	I <sub>s</sub> (MPa)	I <sub>s(50)</sub> (MPa)	UCS (MPa) (Basu & Kamran 2010)
RD 166	I	paragneiss	diametral	parall	6000	38	34		1156	0,841	5,2	4,4	86,1
	II	paragneiss	diametral	parall	2800	38	34		1156	0,841	2,4	2,0	60,3
	III	paragneiss	diametral	parall	5200	38	34		1156	0,841	4,5	3,8	79,6
	IV	paragneiss	diametral	parall	6000	38	34		1156	0,841	5,2	4,4	86,1
	V	paragneiss	diametral	parall	2500	38	34		1156	0,841	2,2	1,8	57,8
	VI	paragneiss	diametral	parall	5300	38	34		1156	0,841	4,6	3,9	80,5
	VII	paragneiss	axial	parall	4600	32	28	38	1355	0,871	3,4	3,0	70,5
	VIII	paragneiss	axial	perp	18000	36	32	38	1549	0,898	11,6	10,4	153,5
	IX	paragneiss	axial	perp	19500	35	30	38	1452	0,885	13,4	11,9	169,6
	X	paragneiss	axial	perp	19000	32	26	38	1259	0,857	15,1	12,9	181,3
	XI	paragneiss	axial	perp	13500	28	22	38	1065	0,825	12,7	10,5	153,8
	XII	paragneiss	block	perp	14500	31	23	32	938	0,802	15,5	12,4	175,4
	XIII	paragneiss	block	perp	16000	32	27	37	1273	0,859	12,6	10,8	157,6
	XIV	paragneiss	block	perp	16000	30	23	34	996	0,813	16,1	13,1	182,6
	XV	paragneiss	block	parall	8000	31	26	40	1325	0,867	6,0	5,2	95,8
	XVI	paragneiss	block	perp	10000	30	24	37	1131	0,837	8,8	7,4	119,8
	XVII	paragneiss	block	perp	17000	31	22	33	925	0,800	18,4	14,7	200,8
	XVIII	paragneiss	block	perp	16000	30	23	35	1025	0,818	15,6	12,8	179,4
GMRD07b	I	paragneiss	axial	perp	21000	36	24	38	1162	0,842	18,1	15,2	206,6
GMRD08	I	paragneiss	diametral	parall	4800	38	34		1156	0,841	4,2	3,5	76,4
	II	paragneiss	axial	perp	8000	33	29	38	1404	0,878	5,7	5,0	93,2
	III	paragneiss	block	parall	9500	34	30	35	1338	0,869	7,1	6,2	106,2
	IV	paragneiss	block	parall	6000	30	27	32	1101	0,831	5,5	4,5	88,0
	V	paragneiss	block	parall	4700	24	19	35	847	0,784	5,5	4,3	85,9
	VI	paragneiss	block	parall	10000	30	26	45	1490	0,890	6,7	6,0	104,0
	VII	paragneiss	block	parall	1000	25	21	35	936	0,802	1,1	0,9	47,2

	VIII	paragneiss	block	parall	1500	32	29	33	1219	0,851	1,2	1,0	49,3
	IX	paragneiss	block	parall	8500	32	28	38	1355	0,871	6,3	5,5	98,3
	X	paragneiss	block	parall	5000	31	27	40	1376	0,874	3,6	3,2	72,9
	XI	paragneiss	block	parall	11000	35	31	36	1422	0,881	7,7	6,8	113,3
	XII	paragneiss	block	parall	9000	26	23	35	1025	0,818	8,8	7,2	117,4
	XIII	paragneiss	block	parall	10000	31	26	34	1126	0,836	8,9	7,4	120,1
	XIV	paragneiss	block	parall	4300	33	29	34	1256	0,857	3,4	2,9	70,2
	XV	paragneiss	block	parall	6000	28	24	40	1223	0,851	4,9	4,2	84,0
	XVI	paragneiss	block	parall	1300	31	27	32	1101	0,831	1,2	1,0	48,6
	XVII	paragneiss	block	parall	9500	34	30	35	1338	0,869	7,1	6,2	106,2
	XVIII	paragneiss	block	perp	5000	35	31	40	1580	0,902	3,2	2,9	69,4
	XIX	paragneiss	block	perp	21000	36	31	45	1777	0,926	11,8	10,9	159,2
	XX	paragneiss	block	perp	3400	27	23	40	1172	0,843	2,9	2,4	64,8
	XXI	paragneiss	block	perp	13000	32	27	33	1135	0,837	11,5	9,6	144,1
	XXII	paragneiss	block	perp	4000	31	28	40	1427	0,881	2,8	2,5	65,1
	XXIII	paragneiss	block	perp	23000	35	30	42	1605	0,905	14,3	13,0	181,7
	XXIV	paragneiss	block	perp	20500	36	26	49	1623	0,907	12,6	11,5	164,9
	XXV	paragneiss	block	perp	10500	36	31	51	2014	0,953	5,2	5,0	92,8
	XXVI	paragneiss	block	perp	16000	31	27	47	1617	0,907	9,9	9,0	137,3

Table 5.3: point load tests performed on the paragneiss of the ÖSC.

SMU	n. test	lithology	type of test	direction	P (N)	D (mm)	D' (mm)	W (mm)	D <sub>e</sub> (mm <sup>2</sup> )	F	I <sub>s</sub> (MPa)	I <sub>s(50)</sub> (MPa)	UCS (MPa) (Basu & Kamran 2010)
CRD02	I	grt micaschist	block	perp	10000	37	29	39	1131	0,837	8,8	7,4	119,8
	II	grt micaschist	block	perp	7500	35	21	45	945	0,803	7,9	6,4	108,5
	III	grt micaschist	block	perp	10000	29	18	39	702	0,751	14,2	10,7	156,5
	IV	grt micaschist	block	perp	9000	35	29	39	1131	0,837	8,0	6,7	111,6
	V	grt micaschist	block	parall	1000	30	27	39	1053	0,823	0,9	0,8	46,3
GMRD10	I	grt micaschist	block	parall	100	35	35	36	1260	0,857	0,08	0,07	38,4
	II	grt micaschist	block	parall	200	35	35	36	1260	0,857	0,16	0,14	39,2
	III	grt micaschist	block	parall	100	39	39	55	2145	0,966	0,05	0,05	38,2
	IV	grt micaschist	block	perp	5500	26	20	40	800	0,77385	6,9	5,3	96,7
	V	grt micaschist	block	perp	1400	26	15	39	585	0,72123	2,4	1,7	56,8
	VI	grt micaschist	block	perp	2600	22	12	40	480	0,68983	5,4	3,7	79,1
	VII	grt micaschist	block	perp	2700	32	17	37	629	0,73309	4,3	3,1	72,6
	VIII	grt micaschist	block	perp	5400	20	13	42	546	0,71012	9,9	7,0	115,6
	IX	grt micaschist	block	perp	1600	29	10	33	330	0,63406	4,8	3,1	71,8
	X	grt micaschist	block	perp	2100	18	12	32	384	0,65605	5,5	3,6	77,5

Table 5.4: point load tests of the garnet – micaschists of the SMU.

ÖSC	n. test	lithology	direction	diameter (mm)	height (mm)	weight (g)	speed (MPa/s)	$\rho$ (g/cm <sup>3</sup> )	UCS (MPa)	$E_{\tan 50}$ (GPa)	$E_{\text{sec mod}50}$ (GPa)*	Poisson's ratio <sub>50</sub>
GMRD07b	I	paragneiss	perp	38	89,3	277,4	0,200	2,74	90,2	20,9	20,5	0,13
	II	paragneiss	paral	38	81,1	253,3	0,200	2,76	71,6	/	/	/
	III	paragneiss	perp	38	81,5	255,2	0,200	2,76	96,9	25,8	24,5	0,37
	IV	paragneiss	perp	38	74,3	232,3	0,200	2,76	98,0	19,8	19,7	0,28
GMRD08	I	paragneiss	perp	25	55,7	74,8	0,200	2,74	88,2	39,4	37,4	0,12
	II	paragneiss	paral	25	51,5	69,5	0,200	2,75	149,6	65,8	63,6	0,21
	III	paragneiss	paral	25	49,1	66,1	0,200	2,74	167,6	64,8	62,2	0,29
	IV	paragneiss	perp	38	66,9	210,1	0,200	2,77	90,2	21,0	19,8	0,18
GMRD11	I	paragneiss	paral	38	75,7	241,6	0,200	2,81	114,1			
	II	paragneiss	perp	38	67,2	213,0	0,200	2,80	82,3	49,4	48,3	
GMRD20b	I	paragneiss	paral	38	83,0	257,1	0,200	2,73	98,6	60,7	58,3	0,32
	II	mylonitized paragneiss	paral	38	84,3	267,5	0,200	2,80	32,7	10,0	11,1	0,03
RD137	I	paragneiss	paral	25	53,1	70,6	0,200	2,71	108,4	88,1	87,6	0,48
RD166	I	paragneiss	paral	38	83,1	259,5	0,200	2,75	98,1	42,9	41,1	0,12
	II	paragneiss	paral	38	73,8	231,7	0,200	2,77	82,4	43,6	44,9	0,16
	III	paragneiss	perp	38	81,9	256,6	0,200	2,76	144,1	40,9	38,0	0,38
	IV	paragneiss	perp	38	82,4	256,3	0,200	2,75	116,2	32,9	30,6	0,19
	V	paragneiss	perp	38	81,8	254,7	0,200	2,75	136,0	36,1	31,8	0,30
	VI (cycles)	paragneiss	perp	38	82,9	260,1	0,200	2,77	137,4	44,1	37,0	0,21
	VII	paragneiss	paral	38	85,6	269,7	0,200	2,78	88,6	70,9	73,7	0,31
	VIII	paragneiss	$\beta=30^\circ$	38	84,9	265,2	0,200	2,75	48,6	20,3	19,1	0,20
	IX	paragneiss	$\beta=30^\circ$	38	67,8	213,7	0,200	2,78	64,6	23,0	22,0	0,19
RD180	I	amphibolic gneiss	$\beta=75^\circ$	25	54,4	72,4	0,200	2,71	145,9	35,1	33,0	0,23
	II	amphibolic gneiss	paral	25	56,9	75,5	0,200	2,70	148,8	46,2	44,3	0,22
	III	amphibolic gneiss	$\beta=30^\circ$	25	56,4	76,0	0,200	2,75	90,3	30,6	30,2	0,25
	IV	amphibolic gneiss	$\beta=75^\circ$	25	56,3	75,5	0,200	2,73	135,8	32,5	30,9	0,29
	V	amphibolic gneiss	$\beta=75^\circ$	25	57,2	76,2	0,200	2,71	49,9	25,7	25,6	0,37

Table 5.5: Summary of the uniaxial compressive tests performed on rock samples related to the ÖSC.

SMU	n. test	lithology	direction	diameter (mm)	height (mm)	weight (g)	speed (MPa/s)	$\rho$ (g/cm <sup>3</sup> )	UCS (MPa)	$E_{\tan 50}$ (GPa)	$E_{\sec \text{ mod} 50}$ (GPa)*	Poisson's ratio <sub>50</sub>
CRD02	I	garnet micaschist	paral	38	83,0	265,7	0,200	2,83	94,9	32,3	32,7	0,13
	II	garnet micaschist	paral	38	83,5	270,5	0,200	2,86	82,7	29,1	28,3	0,12
GMRD15	I	cent garnet micaschist	perp	38	67,7	212,6	0,100	2,77	34,1	4,5	4,8	0,17
	II	cent garnet micaschist	perp	38	80,9	254,6	0,200	2,78	26,2	3,0	2,8	0,05
	III	cent garnet micaschist	perp	38	81,2	262,3	0,100	2,85	32,0	7,0	7,0	0,23
	IV	cent garnet micaschist	perp	38	78,2	249,8	0,100	2,82	31,2	5,0	4,4	0,21
GMRD09	I	grt graphitic micaschist	perp	38	84,3	272,1	0,100	2,85	72,8	26,2	24,0	0,11
	II	grt graphitic micaschist	paral	38	83,3	269,2	0,100	2,85	49,0	45,0	45,2	0,15
	III	grt graphitic micaschist	$\beta=30^\circ$	38	69,5	223,0	0,100	2,83	75,3	28,8	26,5	0,24
GMRD10	I	garnet micaschist	paral	38	70,0	221,6	0,100	2,79	24,5	20,1	20,0	
	II	garnet micaschist	paral	38	85,2	273,4	0,100	2,83	24,8	17,3	17,4	0,10
M	I	calc-silicate marble	perp	38	78,0	253,0	0,200	2,86	153,2	55,3	51,0	0,34
	II	calc-silicate marble	paral	38	82,8	269,7	0,200	2,87	137,2	49,6	43,0	0,43
	III	calc-silicate marble	perp	38	80,4	259,7	0,200	2,85	55,7	36,0	34,0	0,21
	IV	calc-silicate marble	paral	38	76,2	247,7	0,200	2,87	151,2	87,2	83,8	
RD155	I	quartzite	paral	25	49,1	62,0	0,200	2,57	33,8	38,3	39,4	0,16
	II	quartzite	perp	25	54,0	68,1	0,100	2,57	68,4	32,5	32,1	0,27
	III	quartzite	perp	25	51,0	64,9	0,100	2,59	150,8	41,4	39,3	0,17
	IV	quartzite	paral	25	58,0	74,3	0,200	2,61	59,3	34,2	35,8	0,06
RD168	I	garnet micaschist	perp	38	79,0	254,6	0,100	2,84	17,0	2,0	2,2	0,09
	II	garnet micaschist	perp	38	70,9	227,1	0,100	2,83	28,6	2,8	2,7	0,27
	III	garnet micaschist	paral	38	76,0	240,8	0,100	2,80	16,0	10,5	8,3	0,15
	IV	garnet micaschist	paral	38	74,6	232,8	0,100	2,75	27,7	18,6	23,1	0,05
	V	garnet micaschist	paral	38	74,5	238,5	0,100	2,82	32,5	23,0	23,4	0,02
	VI	garnet micaschist	$\beta=30^\circ$	38	71,1	226,4	0,100	2,81	12,3	1,4	0,9	0,10
	VII	garnet micaschist	$\beta=30^\circ$	38	56,9	181,4	0,100	2,81	23,5	5,9	5,8	0,06
RD210b	I	garnet micaschist	paral	25	57,3	85,9	0,100	3,06	82,9	/	/	/
	II	garnet micaschist	paral	25	54,3	83,2	0,100	3,12	79,0	48,9	48,5	0,19

Table 5.6: Summary of the uniaxial compressive tests performed on rock samples related to the SMU.

DOMAIN 1						
JOINT SET	Dip Dir. (°)	Dip (°)	Spacing (m)	JCS (MPa)	JRC (-)	$\phi_b$ (°)
K1	204	79	0,43	114	10-12	26÷29
K3	346	60	0,40	59	10-12	
K4	093	70	0,26	91	16-18	
S	340	20	0,12	64	4-6	
DOMAIN 2						
JOINT SET	Dip Dir. (°)	Dip (°)	Spacing (m)	JCS (MPa)	JRC (-)	$\phi_b$ (°)
K1	200	72	0,23	48	12-14	25÷30
K3	346	45	0,23	30	8-10	
K4	102	80	0,60	60	/	
S	001	27	0,11	29	/	
DOMAIN 3						
JOINT SET	Dip Dir. (°)	Dip (°)	Spacing (m)	JCS (MPa)	JRC (-)	$\phi_b$ (°)
K2	267	67	0,23	90	/	26÷29
S	024	17	0,09	94	/	
DOMAIN 4						
JOINT SET	Dip Dir. (°)	Dip (°)	Spacing (m)	JCS (MPa)	JRC (-)	$\phi_b$ (°)
K1	202	73	/	55	/	26÷29
K2	270	68	0,32	54	/	
K4	117	73	/	57	/	
S	113	19	0,08	15	/	
DOMAIN 5						
JOINT SET	Dip Dir. (°)	Dip (°)	Spacing (m)	JCS (MPa)	JRC (-)	$\phi_b$ (°)
K1	181	82	0,34	35	18-20	25÷30
K2	271	78	0,17	38	/	
K3	010	52	0,49	33	18-20	
K4	094	70	0,20	30	14-16	
S	004	19	0,10	22	/	

Table 5.7: Principal mechanical parameters defining the different joint sets within the different domains.

DOMAIN 1			
ROCK TYPE	$\phi$ (°)	c (MPa)	$E_m$ (MPa)
Paragneiss	40	6,0	16800
DOMAIN 2			
ROCK TYPE	$\phi$ (°)	c (MPa)	$E_m$ (MPa)
Micaschist	37	2,9	11800
Quartzite	49	3,2	15400
DOMAIN 3			
ROCK TYPE	$\phi$ (°)	c (MPa)	$E_m$ (MPa)
Paragneiss	47	3,9	15300
DOMAIN 4			
ROCK TYPE	$\phi$ (°)	c (MPa)	$E_m$ (MPa)
Paragneiss	/	/	/
DOMAIN 5			
ROCK TYPE	$\phi$ (°)	c (MPa)	$E_m$ (MPa)
Micaschist	39	2,7	12700

Table 5.8: Strength parameters evaluated starting from the Q – system.



<b>DOMAIN 1</b>			
<b>LITOLOGIA</b>	<b><math>\phi</math> (°)</b>	<b>c (MPa)</b>	<b><math>E_m</math> (MPa)</b>
<b>Paragneiss</b>	46	1,7	7400
<b>Amphibolitic gneiss</b>	51	1,9	8900
<b>Amphibolites</b>	51	1,8	7700
<b>DOMINIO 2</b>			
<b>LITOLOGIA</b>	<b><math>\phi</math> (°)</b>	<b>c (MPa)</b>	<b><math>E_m</math> (MPa)</b>
<b>Garnet – micaschists</b>	33	2,1	4500
<b>Quartzite</b>	47	4,5	15000
<b>DOMINIO 3</b>			
<b>LITOLOGIA</b>	<b><math>\phi</math> (°)</b>	<b>c (MPa)</b>	<b><math>E_m</math> (MPa)</b>
<b>Paragneiss</b>	51	1,1	7400
<b>Amphibolitic gneiss</b>	54	1,7	12600
<b>Amphibolites</b>	51	1,8	7700
<b>DOMINIO 4</b>			
<b>LITOLOGIA</b>	<b><math>\phi</math> (°)</b>	<b>c (MPa)</b>	<b><math>E_m</math> (MPa)</b>
<b>Paragneiss</b>	44	1,4	3400
<b>DOMINIO 5</b>			
<b>LITOLOGIA</b>	<b><math>\phi</math> (°)</b>	<b>c (MPa)</b>	<b><math>E_m</math> (MPa)</b>
<b>Garnet – micaschists</b>	31	1,7	3000
<b>Quartzite</b>	51	3,2	18200
<b>Marble</b>	41	2,0	20300

Table 5.9: rock mass strength parameters evaluated using Hoek and Brown strength criterion based on GSI. Data calculated using RocLab software (Rocscience).

## 5.6 Figure Captions

Figure 5.1: Histogram graphs of the distribution of spacing and JCS in the SMU and OSC complex; a) histogram graph of the spacing distribution in the ÖSC; b) histogram graph of spacing distribution in the SMU; c) histogram graph of the JCS values collected on the SMU; d) histogram of the JCS values collected on the ÖSC.

Figure 5.2: Histogram of the distribution of GSI within the SMU and OSC complex in the Western and Eastern sector; a) histogram graph of the GSI distribution along the SMU in the Western sector; b) histogram graph of the GSI distribution along the ÖSC in the Western sector; c) histogram graph of the GSI distribution along the SMU in the Eastern sector; d) histogram graph of the GSI distribution along the ÖSC in the Eastern sector.

Figure 5.3: Failure strength versus  $\beta$  for gneiss samples of ÖSC and garnet – micaschists samples of SMU.

Figure 5.4: Stress – strain curves of gneiss samples of ÖSC;

Figure 5.5: Stress – strain curves of garnet – micaschists of SMU;

Figure 5.6: Distribution of UCS values compared to Young's modulus and Poisson's ratio in the ÖSC; a) distribution of UCS versus  $E_{\tan 50}$ ; b) distribution of UCS versus Poisson's ratio.

Figure 5.7: Distribution of UCS values compared to Young's modulus and Poisson's ratio in the SMU; a) distribution of UCS versus  $E_{\tan 50}$ ; b) distribution of UCS versus Poisson's ratio.

Figure 5.8: Map of geomechanical domains derived from field and laboratory geomechanical analysis. Base map: shaded relief image of ALS – HRDEM.

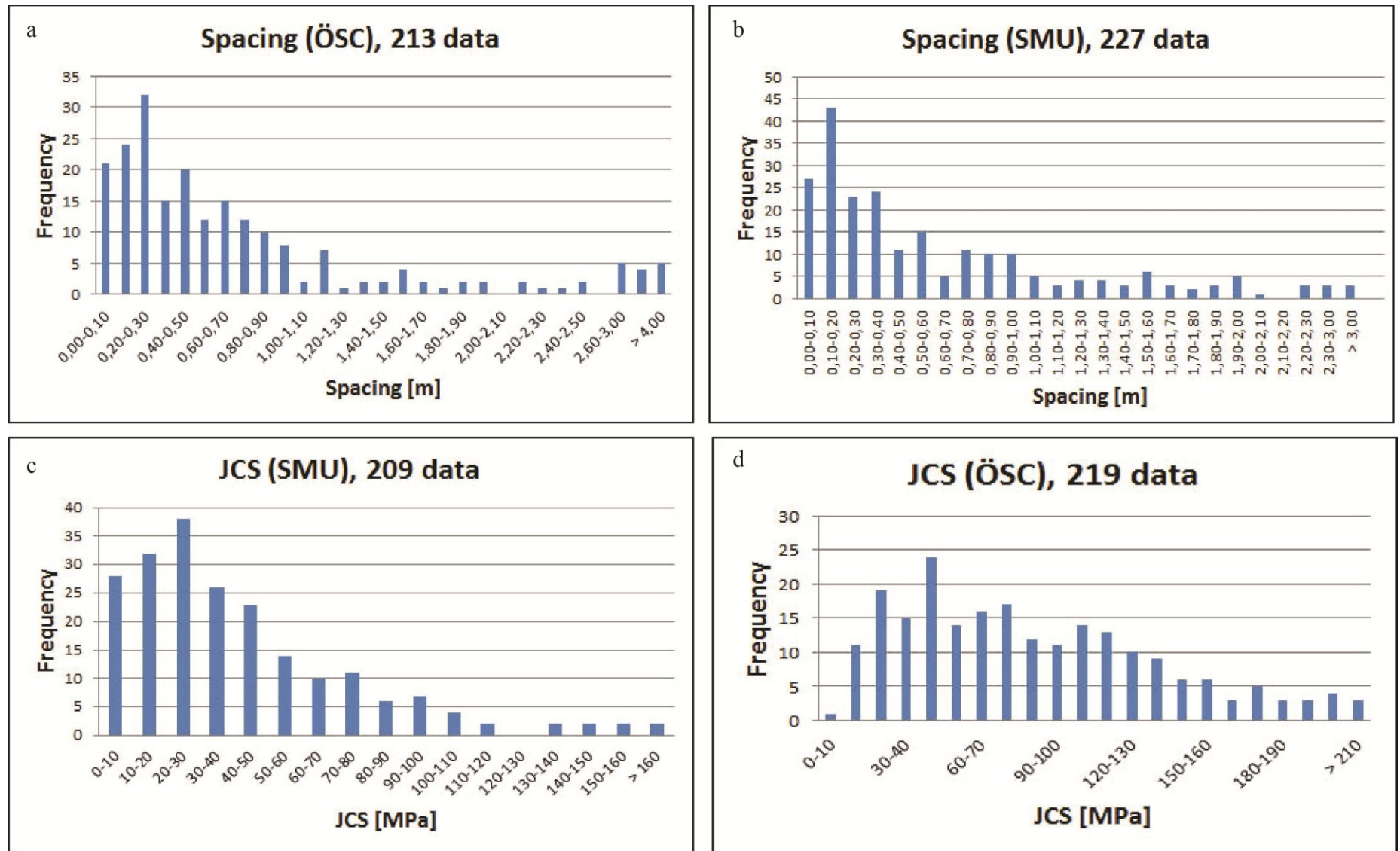


Figure 5.1

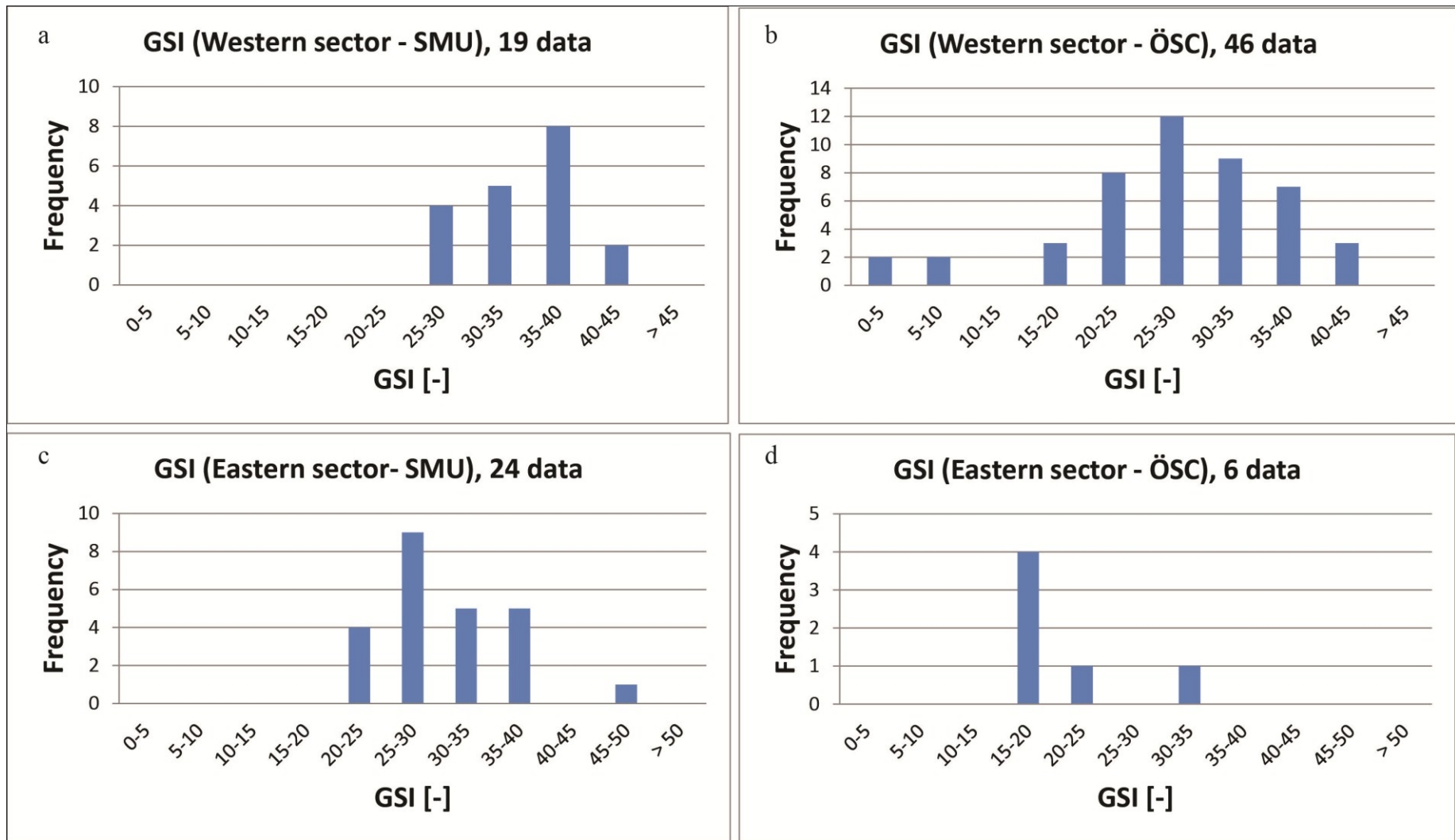


Figure 5.2

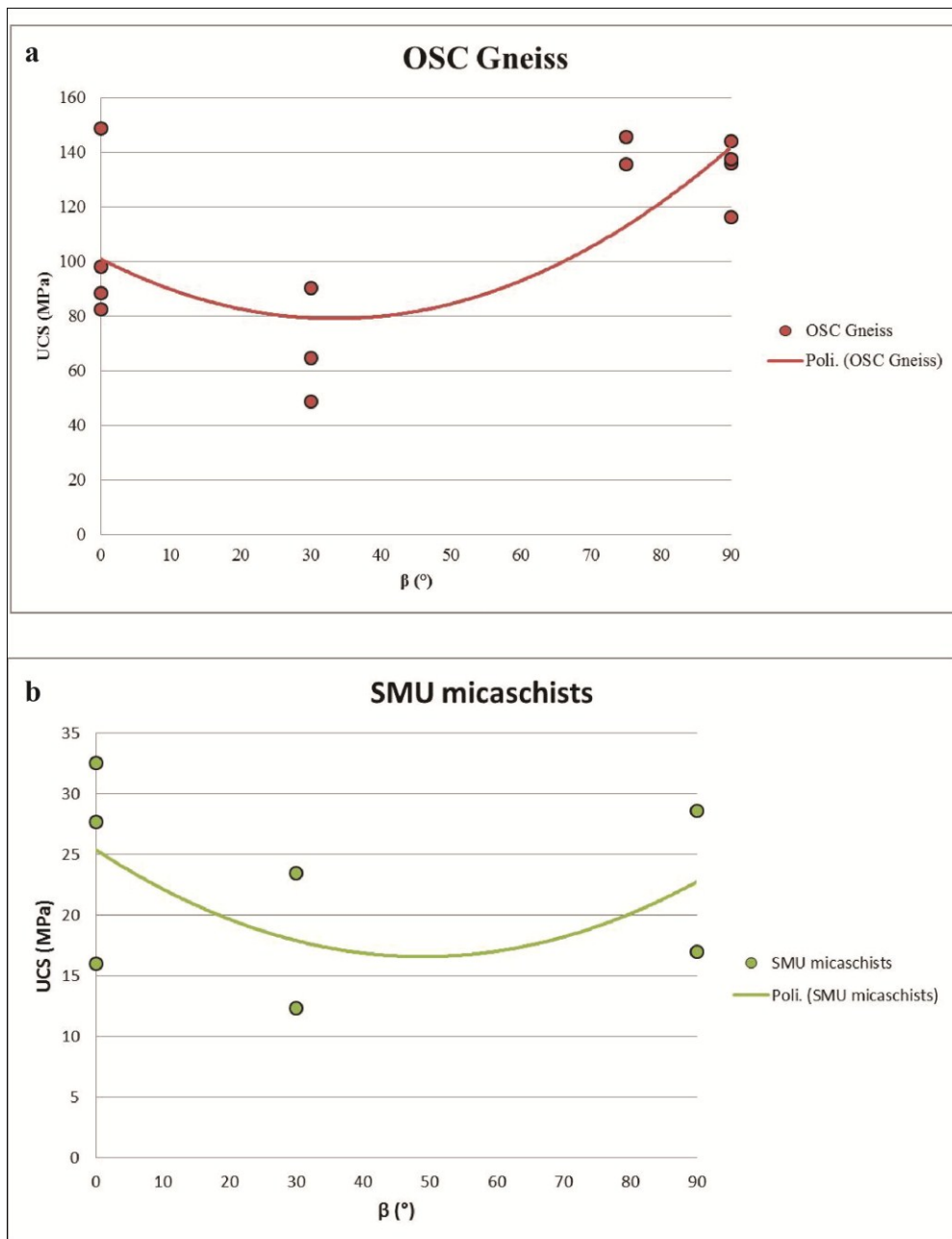


Figure 5.3

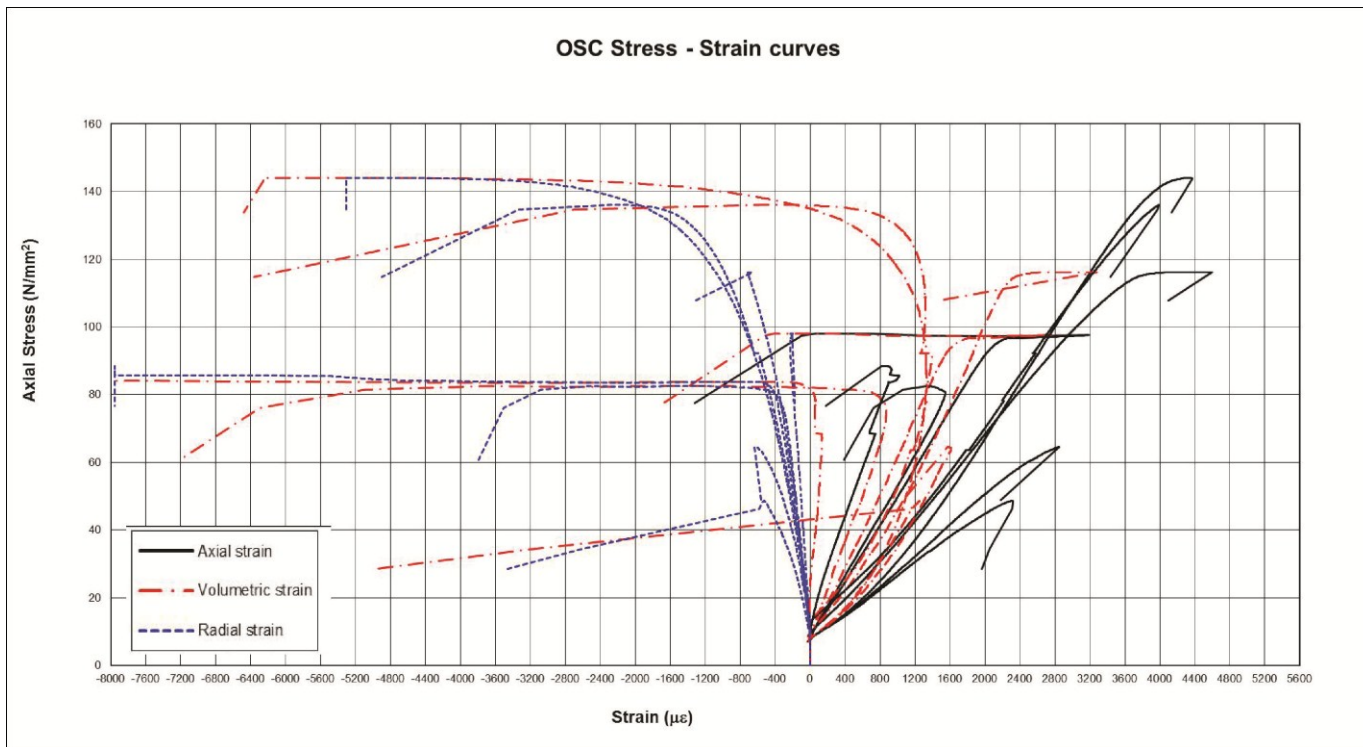


Figure 5.4

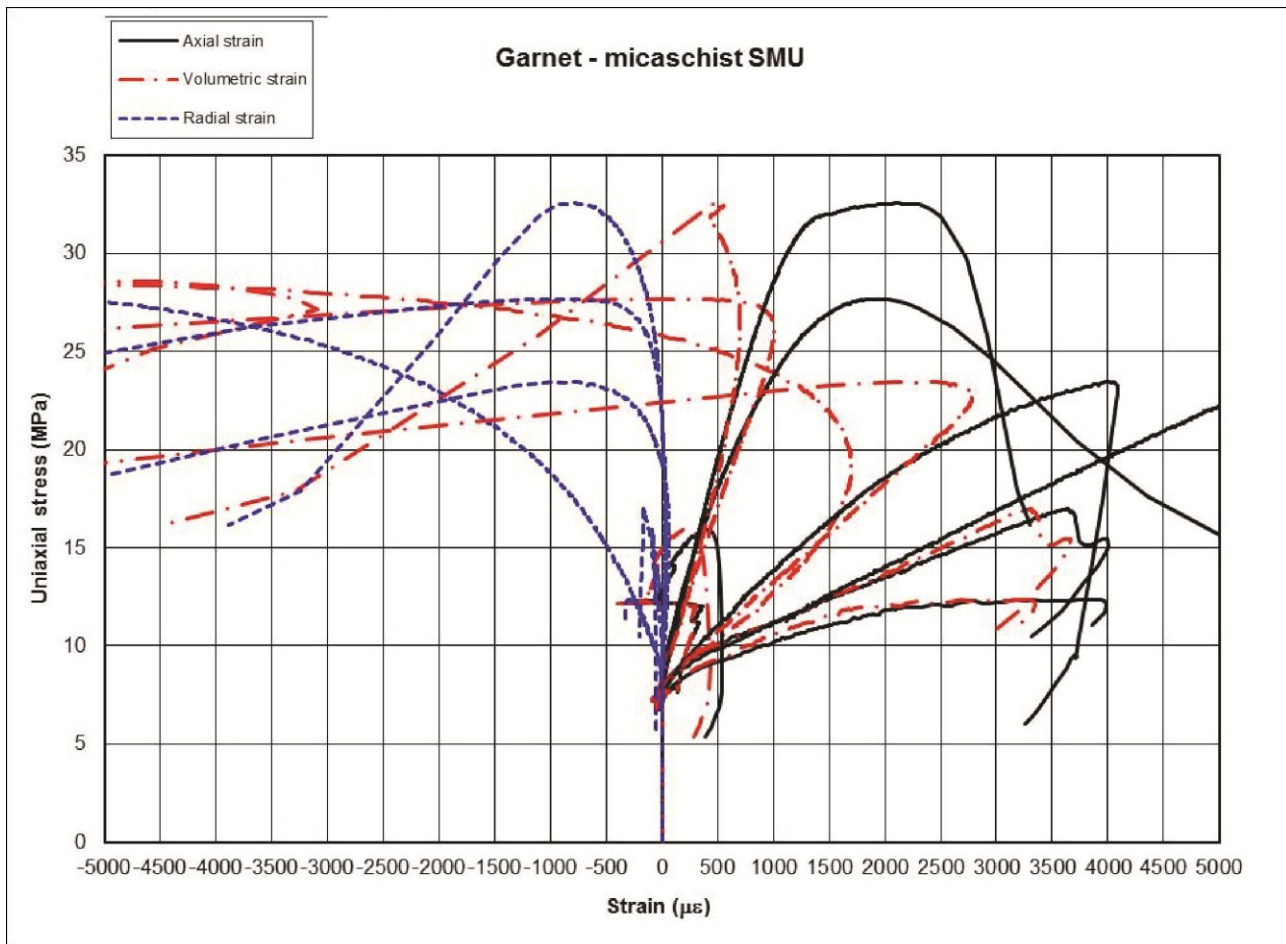


Figure 5.5

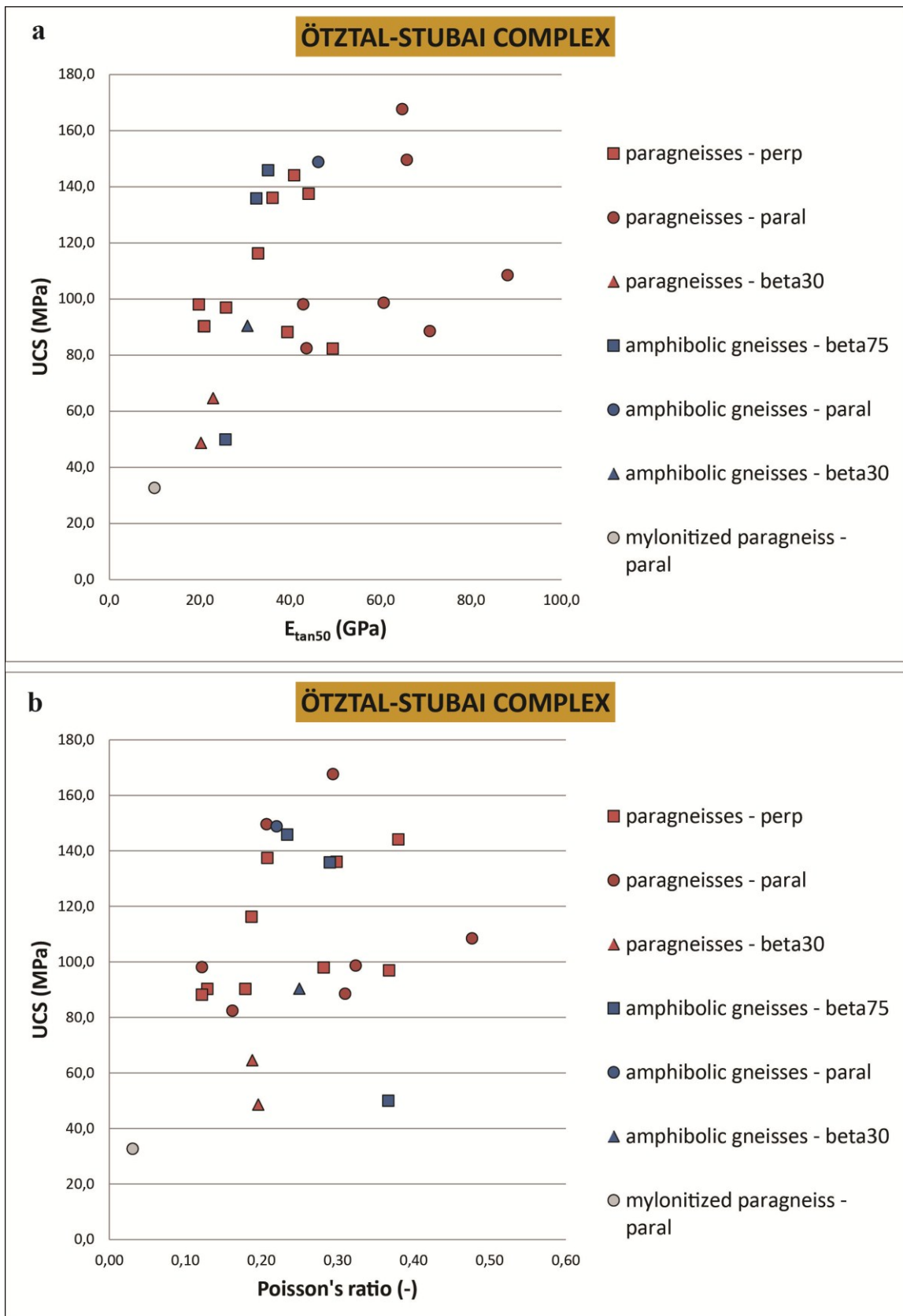
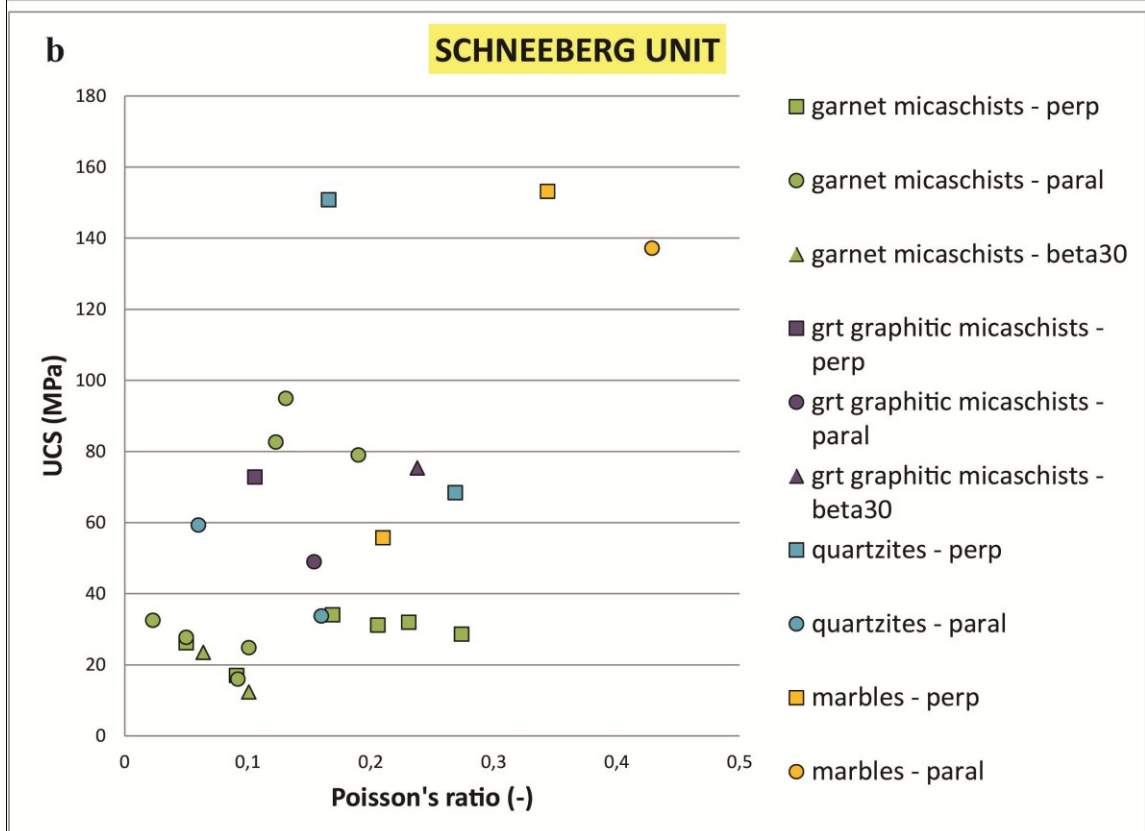
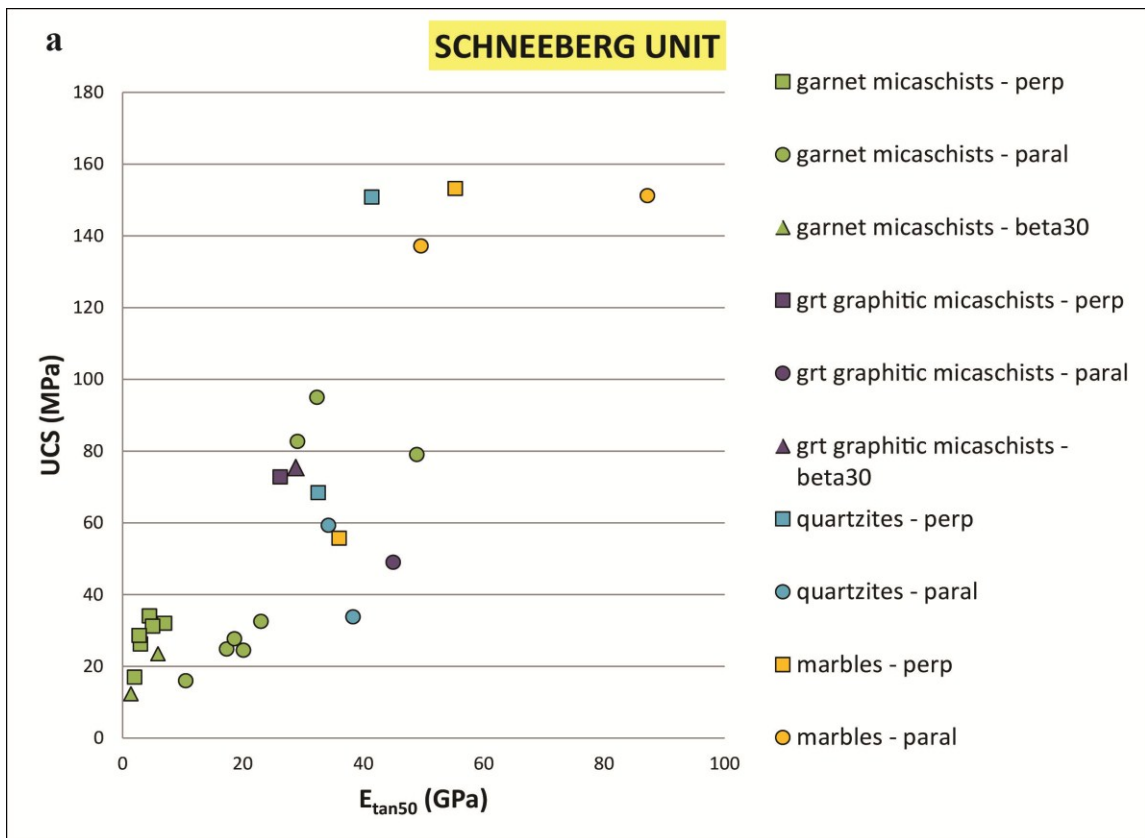


Figure 5.6





Figure

5.7



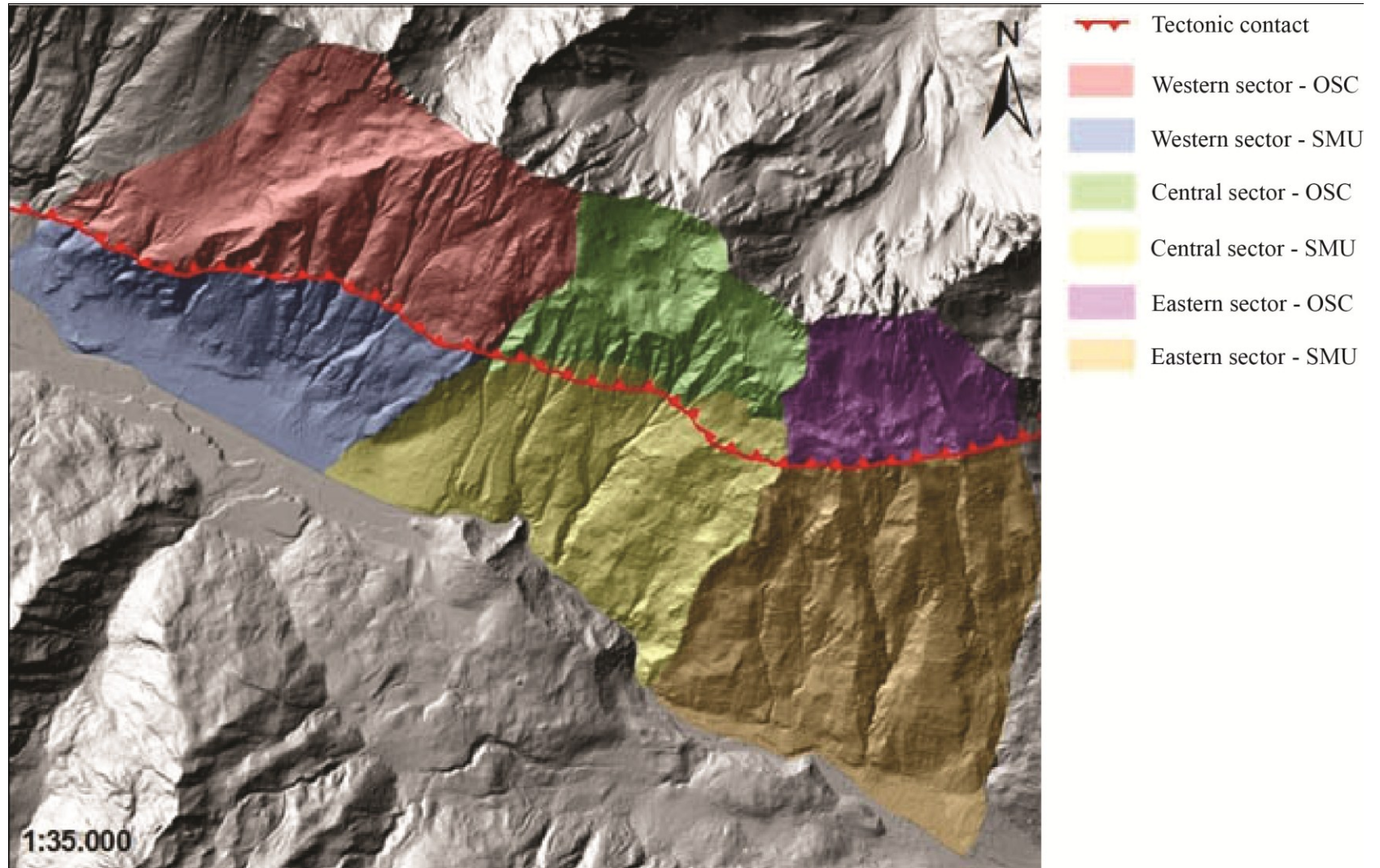


Figure 5.8

# 6. A FEM/DEM approach for modeling progressive failure in foliated rock slopes: the Ridnaun rock avalanche

Luca Zorzi, Douglas Stead, Rinaldo Genevois.

## 6.1 Introduction

The evolution of DSGSDs requires a significantly improved understanding of the mechanisms involved in order to allow the prediction of the impending landslide features. Usually, evolutionary characterization and development is carried out on the basis of the observation of indicators and precursory signals that should be unambiguous, not based on a detailed comprehension of the mechanics and dynamics of the deformation processes.

In fact, in rock slope stability analysis, the failure surface is often assumed to be structurally controlled and predefined as a continuous plane or series of interconnected planes. Such assumptions are valid in cases where the volume of the failed block is relatively small (e.g. thousands of m<sup>3</sup>) or where major persistent faults and/or bedding planes are present and favorably oriented (Brideau, 2002; Brideau et al., 2009; Eberhardt et al. 2004 and Eberhardt 2008).

In massive natural rock slopes, the presence of persistent key discontinuities enabling kinematical release is more limited, and a complex interaction between existing natural discontinuities and brittle fracture propagation through intact rock bridges is required to bring the slope to failure (Bachmann et al., 2009; Eberhardt et al. 2004 and Eberhardt 2008). The shear strength along potential failure surfaces is hence determined partly by the failure through intact rock and partly by shear along discontinuities. Until now, the relative influence of controlling factors remains unclear and requires further investigations (Bouissou et al., 2012).

The process of failure through intact rock bridges in massive rock slopes, called progressive failure (Terzaghi, 1962; Eberhardt et al., 2004, Groneng et al. 2010), entail the progressive degradation and destruction of the rock mass cohesive elements (strength degradation processes), manifested through internal slide mass deformation

and damage mechanisms, enabling the kinematic release. Thus, a model for studying rock slope stability should encompass the nucleation or activation of cracks within the rock, the possible coalescence of which would then lead to the creation of a critical failure surface. Failure in rock slopes is frequently preceded and/or followed by creep, progressive deformation (fatigue damage processes), and extensive internal disruption of the rock mass (Stead et al., 2006). Thus, factors controlling initiation and eventual sliding may be complex and not allowing simple static analysis (Stead et al., 2006). The importance of progressive failure on rock slope instability was illustrated by Eberhardt et al. (2004). In his work, Eberhardt used multi-methods approach progressing from continuum, through discontinuum, to FEM/DEM modeling approach to investigate progressive failure in the Randa rockslide in Switzerland. In this work, a multi-methods approach based on finite element (Phase2) and hybrid FEM/DEM modeling using the Elfen code (Rockfield, 2001) was used to investigate trigger mechanisms, key stages of progressive failure and fracture propagation to either back analyse and define the mechanical behavior of the Ridnaun rock avalanche. The modeling strategy used for the simulation considers the most important factors affecting the deformation such as the rock mass heterogeneity, glacial history and earthquake effects. In this chapter we want to demonstrate that the combine effect of glacial erosion and loading – unloading cycle triggers progressive failure processes responsible for progressive nucleation and propagation of fractures through intact rock with no major effect of the discontinuity network defining the rock masses, predisposing the slope to potential high energy failures.

## **6.2 Progressive failure in rock slopes**

The process of failure through intact rock in massive rock slopes, called progressive failure (Terzaghi, 1962; Eberhardt et al., 2004, Groneng et al. 2010), entail the progressive degradation and destruction of the rock mass cohesive elements (strength degradation processes), manifested through internal mass deformation and damage mechanisms, enabling the kinematic release (Hajiabdolmajid,et al, 2002; Eberhardt et al, 2004; Yan, 2008). Massive rock slopes may not experience a rapid change in kinematic state and frequently have stood in a relative stable condition over periods of thousands of years. The final failure surface may eventually develop through the interconnection of discontinuity affecting the slope. Dilation and internal deformation mechanisms may partly drive the failure processes, which normally should initiate at the toe of the rock slope where stresses are higher (Eberhardt et al., 2004; Stead et al,

2006). This is suggested by the typical DSGSD geomorphic features such as scarps, counterscarps and trenches defining the top of a deforming slope. Progressive failure mechanisms are allowed by simple decrease of rock mass strength due to slopes undercut and erosion (Jaboyedoff et al., 2009; Leroueil, 2001; Cruden and Martin, 2004), with the failure surface that can be controlled either by the geometry of the slope (Golts and Rosenthal, 1993; Jaboyedoff et al., 2004a) or by strength degradation phenomena due to glacial unloading. Agliardi et al. (2001) and Eberhardt et al. (2004) showed that Alpine valley slopes undergo slow destabilization phenomena due to valley reshaping and glacial unloading, triggering progressive failure mechanisms on brittle rock slopes.

According to Augustinus (1995), glaciation and deglaciation cycles influence rock mass stability in two main ways: steepening of rock slopes due to glacial erosion and debuttrass with consequent stress release. Rock-slope steepening increases the self-weight (overburden) shear stress acting within the rock mass (Radbruch – Hall, 1978; Bovis, 1982; Caine, 1982; Ballantyne, 2002), generating shear stress condition at the toe of the slope (Augustinus, 1995; Eberhardt et al., 2004).

In addition, during valley glaciers retreat and resultant unloading of glacially stressed rocks, strain energy is released (Ballantyne, 2002). The induced stress redistribution results in shifts in the orientation of the principal stress field in the rock mass. Thus, relaxation of tensile stress within the rock mass causes a “rebound” effect of the valley walls, whose magnitude is dependent on the residual strain energy and the modulus of elasticity of the rock (Ballantyne, 2002). Stress release may result in fracture propagation through the internal discontinuity network, along with loss of rock mass cohesion through breaking of rock bridges. Internal deformation mechanisms, damage and strength degradation processes (progressive failure) are considered to be controlled by the structural setting of the rock mass, the characteristics of the discontinuity sets (i.e. low or high persistence joints) and rock mass geology. Indeed, gravitational adjustments of rock slopes driven on one side by the interaction of changing stress conditions due to glacial over - steepening and stress relaxation following glacial debuttrass, and rock mass strength controlled by lithology and structural setting on the other. Such interaction may act as trigger for i) large scale catastrophic rock slope failure (Agliardi et al., 2001, 2012; Massironi et al, 2010), ii) large scale rock mass deformation (Eberhardt et al., 2004); iii) adjustment of rock faces by discrete rockfall events (Augustinus, 1995; Ballantyne, 2002).

Conventional linear (Mohr – Coulomb) and non-linear (Hoek – Brown) failure criterion govern strength degradation and mobilization processes, assuming implicitly a simultaneous mobilization of the cohesive and frictional strength (Yan, 2008; Barton and Pandey, 2011). This approaches, even when strain-softening models with residual strength parameters are chosen, have not been successful in predicting the damaged area in a rock mass strained beyond its peak strength (Hajiabdolmajiid et al., 2002; Barton and Pandey, 2011). To overcome this issue, Hajiabdolmajid (2001), Hajiabdolmajid et al. (2002), and Hajiabdolmajid and Kaiser (2003), starting from the work of Schmertmann and Osterberg (1960) and Martin and Chandler (1994), adopted a new constitutive based on a strain-dependent cohesion weakening – frictional strengthening (CWFS) to simulate brittle rock slope failure (i.e., Frank slide, Hajiabdolmajid, 2001). With this approach, cohesion degradation and friction mobilization are function of plastic strain ( $\epsilon_p$ ). In brittle failure of strained rock masses, cohesion degradation is driven by time – dependent progressive breaking of intact rock bridges, governing both the progressive development of the failure surface on deforming slopes and long term stability of rock slopes (Kemeny 2003).

Indeed, modeling of progressive shear plane development needs to consider both strength degradation (plastic shear strains evolve and/or tensile fracture develops) and brittle fracture propagation (Eberhardt et al., 2004).

### 6.2.1 *The Ridnaun rock avalanche*

The left slope of the Ridnaun Valley (Sterzing/Vipiteno, South Tyrol, Italy), set on the crystalline units of the Austoalpine Nappe of the alpine orogenic wedge, shows evidence of quaternary gravitational evolution which highly depends on the interaction between the slope trend and the brittle/ductile structural setting. A fully evolved gravitational collapse, having the typical features of a rock avalanche, characterizes the central part of the slope; whereas to the east and west of the rock avalanches, deep seated gravitational slope deformations (Wetterspitz DSGSD to the W, and Telfer Weissen DSGSD to the E), still involve the slope (Fig. 4.5 and 4.6; see chapter 4).

The slope is carved within the paragneiss rocks of the Oetztal - Stubai Unit and the garnet-micaschists of the Schneeberg/Monteneve Unit (Fig 4.5). These two units are separated by a NNW gentle dipping tectonic contact, which obliquely intersects the E–W slope, and is well described by ultracataclastic and mylonitic layers following the regional low angle north-dipping foliation. Approaching to the tectonic contact, relicts of an ancient foliation within the regional Sr foliation in the ÖSC are defined by folds

with sub-horizontal E-trending axes. The folds induce the change in the dip direction of the regional foliation in the ÖSC from N dipping to SE dipping. NNE-SSW and N-S trending faults, having a mean 1 m thick incoherent fault breccia, affect the entire slope. On one hand the recognized fault network together with the K1 discontinuity set, act as lateral release of the unstable areas; on the other hand, the small – scale folds in S<sub>1</sub> domain within the ÖSC coupled with the non – parallelism between the tectonic contact trend and the slope, ease the DSGSD formation and evolution (Wetterspitz DSGSD), and acted as releasing factor for the crown area of both the rock avalanche and the Telfer Weissen DSGSD. The purely brittle deformation of the ÖSC mainly in the rock avalanche and the Telfer Weissen DSGSD, is interpreted to be driven by a brittle/plastic deformation of the garnet micaschists of the SMU, throughout a widely distributed micro-cracking of rock mass. In fact, the pre – existing network of brittle discontinuity sets do not show any joint set favorably oriented to enable kinematic release.

As stated in chapter 4, the three recognized rock slope instabilities can be interpreted as three different stages of the same evolutionary path, driving a creeping deforming rock mass into a rock avalanche-type failure. The Telfer Weissen DSGSD, due to similar structural setting and dimensions, has to be considered as the pre-failure condition of the Ridnaun rock avalanche (see chapter 4). Indeed, to investigate the trigger mechanisms responsible for the failure, key stages of progressive failure and fracture propagation along the slope responsible for the ongoing creeping brittle/plastic deformation driving both the pre-failure stage of the Ridnaun rock avalanche and the ongoing DSGSDs, a back - analysis through hybrid FEM / DEM numerical modeling technique on the Ridnaun rock avalanche will be presented in this chapter.

### **6.3 Numerical analysis of progressive failure initiation and propagation**

#### *6.3.1 Material and methods*

Back analysis of a slope failure requires detailed characterization of the conditions within the rock mass, such as position of sliding surface, extends of the deforming area, earthquakes forces, etc. immediately before the failure. Analysis can be performed with trial and error of the likely rock mass and discontinuity strength, until the limit of stability equilibrium is reached (Factor of Safety, FOS = 1; Styles, 2009). In order to do that, continuum approach using the finite-element code Phase<sup>2</sup> (Rocscience, 2008) was chosen. The automated detection of the limit state was possible through the application of the “Shear Strength Reduction” technique (SSR) (Rocscience, 2004; 2008). SSR

techniques allows the evaluation of the critical Strength Reduction Factor (SRF), which can be considered an equivalent to the FOS, representing in fact the amount by which the mass strength must be reduced to result in failure. Due to the ability of the technique to show progressive reduction in strength of the rock mass, it can capture progressive failure (Diederichs et al., 2007). The ability of SSR approach in modeling progressive failure is clear when considering the method in an excavation application (Styles, 2009). In fact, once the last excavation slice is removed, shear strain can develop marking the location of either a continuous potential failure plane or widespread disruption of rock mass.

In this work, SSR using a strain softening based on Mohr – Coulomb linear criterion was used. Peak and residual input values (table 1) were evaluated through parametric analysis. Starting from field data collected during geomechanical survey (chapter 4 and 5), input data were calculated using Diederichs (2007) and Cai et al. (2004) suggestions based on GSI values, in order to follow the strain - dependent CWFS approach (see paragraph 6.2). An issue in SSR techniques is the fact that SFR considers a simultaneous downgrade of both  $c$  and  $\tan\phi$ , whereas Hajiabdolmajid (2002), Diederichs (2007) and Diederichs et al. (2007) state that independent downgrade could be important as cohesion has more variability than frictional strength.

Although continuum analyses gave useful output to analyze rock slope stability problems, the Ridnaun rock avalanche shows a complex failure mechanism, mainly driven by brittle fracturing of intact rock then reactivation of pre-existing brittle discontinuities. Thus, a new modeling approach is needed, able to model both intact rock behavior and development of fractures (Munjiza et al., 1995). In this case, the commercial code ELFEN was used (Rockfield, 2007).

The hybrid FEM/DEM approach combines aspects of both finite elements and discrete elements with fracture mechanics principles (Elmo, 2006; Elmo and Stead 2010). The ELFEN code (Rockfield, 2007) is a 2D/3D package incorporating the hybrid FEM/DEM approach, which allows the investigation of brittle-fracture initiation and development on intact rock (Cai and Kaiser, 2004), rock slope failures analysis (Eberhardt et al., 2004; Stead and Coggan, 2007, 2012), and mine pillars (Elmo et al., 2005, 2006; Pine et al., 2006).

Fracturing process in ELFEN is controlled according to fracturing criterion specified by constitutive models such as Rankine tension, rotating crack, Mohr-Coulomb etc. (Eberhardt et al., 2004; Elmo, 2006; Styles, 2009). The ELFEN code allows the progressive transition of an intact blocky rock mass into a rock debris during runout and

deposition can be simulated (Stead and Coggan, 2012). Each newly created particle is discretized and the software checks for further fracturing as the simulation continues (Elmo, 2006; Styles, 2009; Elmo and Stead, 2010; Stead and Coggan, 2007, 2012).

### 6.3.2 *Valley excavation approach*

Stress re-distribution along slopes and rock mass strength changes associated with progressive glacial processes (erosion and loading/unloading cycles) were numerically investigated so far using an "horizontal slice approach": glacial loading/unloading and bedrock erosion processes are performed through a staged removal of horizontally-shaped slices (Agliardi et al., 2001; Eberhardt et al., 2004; Hürlimann et al., 2006; Apuani et al., 2007; Massironi et al., 2010; Agliardi et al., 2012).

Differently from previous authors, Leith (2012) investigated the glacial induced damage on valley walls using a different excavation approach. Starting from a fluvial V-shape valley morphology, he numerically investigates the stress changes associated with progressive erosion of a V-shaped valley transitioning to a U-shaped beneath glacial ice through a staged removal of parabola - like slices.

Following Leith (2012) approach, a new "glacial valley - type excavation approach" was used for the numerical modeling of behavior of the left slope of the Ridnaun Valley. In this work, bedrock slices were removed in a staged manner using a "valley - approach" In order to simulate stress changes and fracture initiation and propagation associate with progressive erosion resulting in a U-shaped valley due to glacial erosion, (Fig. 5.1). With this approach the valley is shaped through glaciation and replacement of rock by glacial ice and the following ice retreat using trying to mimic the most probable natural valley shaping process.

More specifically, asymmetrical valley geometry was recreated starting from the actual geometry of the valley in its central sector (Fig.5.2). Due to the presence of stiffer lithologies on the left slope of the Ridnaun Valley, such as ÖSC complex, glacial erosion processes act in a differential manner, modeling the valley asymmetrically with gentle slopes on the right side and steeper slopes on the left side of the valley (Fig. XX). In fact, the profile of the right slope of the valley is strongly structurally controlled by the N - dipping foliation planes defining the garnet-micaschists of the SMU complex.

### 6.3.3 *Modeling of process initiation*

Initial 2D finite-element simulations were performed to investigate the role glacial processes may have played in the initiation and development of the initial condition of



progressive failure of the Ridnaun rock avalanche prior to the failure. The analysis was performed by means of the finite-element continuum code Phase<sup>2</sup> (Rocscience, 2008). Glacial unloading was simulated assuming glacial erosion of about 1300 m of rock relative to the valley bottom (Fig. 5.1). This value is in accordance with the maximum altitudes reached by the glacial ice surface in the valley based on glacial and paraglacial deposit founded during field surveys (see chapter 4).

Several model geometries were tested to avoid boundary effects on the results of the simulations.

Valley shaping process was subdivided into 12 stages which include: a) initial bedrock conditions, b) shaping of the valley through glaciation and replacement of rock by glacial ice and c) retreat of glacier from the valley into 5 stages.

Stresses were initialized assuming a stress state within a rock mass only from gravity loading alone. Thus, the  $k$  ratio was calculated based on the following equation, using the parameters in table 1:

$$k = \frac{\nu}{1 - \nu}$$

Due to the lack of knowledge on the hydrogeology of the studied slope, no analyses were performed considering pore pressures. The effect of water circulation, especially during glacial retreat, was simulated downgrading the frictional component of the strength (table 2).

The methodology used for the model was to start the investigations with simple models, and then build – up the complexity. Initial models representing the ÖSC and SMU complexes as homogeneous and isotropic rock masses were performed (input values in table 1). Then, in order to simulate the mechanical behavior of the slope in a more realistic way, discontinuities were added to mimic real structural setting of the rock mass. Metamorphic fabric (N – dipping regional foliation; see chapter 4) was reproduced by means of a parallel deterministic joint network. To represent the different fabric between the paragneisses of the ÖSC and the highly foliated garnet – micaschists of the SMU, variable spacings were used: 70 m for ÖSC and 35 for SMU (Fig. 5.3 and 5.4). Those values were chosen on a try and error basis, representing the best compromise between reasonable results and computing time.

To represent the crenulation cleavage and the C'-type shear band cleavage defining the ductile setting of the garnet – micaschists of SMU (see chapter 4), a beachler joint network (Rocscience, 2008) was used (Fig. 5.3 and 5.4).

Material properties used were based on those of glacial ice (Schulson, 1999), the paragneisses of ÖSC and garnet – micaschists of SMU (Table 1).

To investigate damage initiation, a Mohr – Coulomb elasto – plastic yield criterion was used, with input parameters listed on table 1. Modeling results show the development of tensile fracturing parallel to the topography as a consequence of glacial unloading/rebound. In fact, the key mechanisms controlling rebound – induced fracturing are the strain energy release driving the generation of tensile strength (Eberhardt et al., 2004).

Strain – softening model based on Mohr – Coulomb failure criterion was used aiming to model shear plane development on Ridnaun rock avalanche as a function of rock mass strength degradation. Strain – softening was applied using peak and residual values of the Mohr – Coulomb strength components ( $c$  and  $\phi$ ; input values in table 1). Results of the models show a progressive development of a shear zone that extends from the toe of the slope up to the tectonic contact separating the two rock masses (Fig. 5.3 and 5.4). Tensile fracture damage parallel to the topography, induced by glacial unloading and rebound, accompanied by shear deformation are localized on the garnet – micaschists of the SMU. ÖSC units are interested mainly by tensile damage only nearby the tectonic contact (Fig. 5.3 and 5.4). Thus, tensile and shear yielded elements indicate a progressive damage and widespread internal disruption of the rock masses, especially for the SMU, impeding the formation of a well - developed failure surface. In the last stage of the excavation sequence, SSR simulation was applied to evaluate the stability condition of the slope after glacial erosion and unloading. SSR approach predicts a SRF (equivalent of FoS) of 1.11, defining a quasi – stable condition of the slope. Thus, glacial erosion and unloading do not act as the trigger for the rock slope failure, but initiate a rock strength degradation process through internal rock mass disruption.

As stated in chapter 4, Given the proximity of the study area to an active seismogenic fault (Inn Valley fault; historic event around  $M_r = 7$ ), can be consider a seismic event as a realistic trigger for the Ridnaun rock avalanche. Thus, a parametric analysis was performed to investigate the earthquake forces, in terms of horizontal loading, necessary to bring the slope to unstable conditions ( $FoS < 1$ ). Parametric analysis showed that the critical  $a$  value needed to reach unstable conditions ( $FoS < 1$ ) is 0.1, mimic a low magnitude earthquake (Fig. 5.4). In fact, applying a local gravity load of  $a = 0.1$ , SSR simulation predict a SRF of about 0.91, defining unstable condition within the slope. As for the previous models, the development of a progressive shear zone is concentrated mainly in the SMU, in which shear and tensile yielding elements are widely distributed

along the shear zone. Even in this case, there is no clear indication of the development of a well - defined failure surface within the unstable area.

Results coming from finite - element analyses using the code Phase2 show that the erosion history and glacial unloading/rebound induce on one hand strength degradation processed through widespread damaging and disruption among SMU; on the other hand, deformation of the ÖSC the gneisses of the OSC react in a more brittle way through the formation of discrete tensile domains expressed in the field by scarps and counterscarps. Indeed, these results seem to support the mechanics of the Ridnaun rock avalanche hypothesized from field surveys (see paragraph 6.2.1 and chapter 4).

#### *6.3.4 Modeling of brittle fracture initiation and propagation*

Even though continuum models could capture some key aspect of progressive shear plane development at the Ridnaun rock avalanche, they have some limits regarding the investigation of brittle fracture initiation and propagation within the slope.

A Mohr – Coulomb / Rankine crack model was used aiming to investigate the development of a shear failure on the investigated slope. The basic material properties used were kept the same as those given in tables 1 and 2. The investigation of the brittle fracture initiation and propagation was performed analyzing the brittle behavior of the slope treating the two involve rock masses first as homogeneous and isotropic rock masses, and secondly as discontinuous rock masses. The discontinuities included in the model (named “fractures” in ELFEN code) aim to reproduce the metamorphic fabric of the two units. Spacing and geometry of the discontinuities are kept the same as those used to build – up the geometry for Phase<sup>2</sup> simulations. In order to take into account the effect of pore pressure and weathering - induced strength degradation deriving from both sub – glacial water circulation and rainfalls, low friction angle were applied to the fracture included in ELFEN models.

The geometry used for ELFEN simulation was reduced respect to the one used for finite – element simulation. Geometry reduction was necessary in order to reduce computational time for each simulation.

Valley shaping processes and glacial unloading effects were investigated in a staged way. Seven excavation stages were used to model glacial erosion processes, whereas the loading and unloading effect was simulated by adding extra loads on the final topography, whose magnitudes are equivalent of the glacial ice cover.

Results of the models of both approaches are provided in Fig. 5.5, whereas detailed description of input data for each simulation is in appendix A.

Field surveys, coupled with finite – element simulation, do not highlight the development of a clear failure surface, thus all ELFEN models were set up without the inclusion of a pre – existing failure plane, allowing the failure to develop through internal fracturing and shearing.

Discontinuous models suggest a staged failure. The first stage is defined by progressive fracturing starting from the toe of the slope as the last block is excavated. Then fracturing tend to progressively propagate up – slope, creating a damaged zone having a variable thickness between 50 – 100 m (Fig. XX). The model suggests that glacial erosion / rebound triggers extensive internal deformation, fracturing and dilation along the slope.

Fracturing area stopped at the glacial shoulder (Fig. 5.5), testifying the fracturing processes actively driven by in situ stresses induced through erosion and unloading. As already suggests by Leith (2012), the high-strength de-stressed rock above the shoulder favored the development of a strength-limited slope, stopping the progressive failure propagation process at the glacial shoulder (Fig. 5.5). Pre – existing discontinuities, mimic the metamorphic fabric, due to their unfavorable orientations do not have any major effect on fracture nucleation and propagation. Thus, fracturing process involved entirely intact rock domains.

The high degree of internal fracturing acts to reduce the kinetic energy available to drive the mass. Due to the low Heim's Fahrböschung (runout travel angle,  $\tan\alpha$ ; see chapter 4), it is reasonable to believe in an individual episodic event. In fact, if the mass failed through several events, the available kinetic energy would be low resulting in smaller runout.

In this scenario, even a low magnitude seismic event could enable the slope failure, which, as a result of the high degree of fracturing, will be rock avalanche in type.

#### **6.4 Discussion and conclusion**

Various numerical techniques (continuum and hybrid methods which combine both continuum and discontinuum approach to simulate brittle fracture initiation and propagation) have been applied to back-analyze the Ridnaun rock avalanche event aiming to evaluate the effect of glacial erosion/rebound and glacial unloading as trigger for progressive failure processes.

Finite difference analyses using Phase2 confirm the starting hypothesis: the erosion history and the cyclical glacial loading due to Pleistocene glaciations, induce on one hand a plastic deformation (mainly shear type deformation) among SMU; on the other

hand the gneisses of the OSC react in a more brittle way through the formation of discrete tensile domains expressed in the field by scarps and counterscarps. The mean Factor of Safety (FoS) coming from the analyses is 1.12, indicating a quasi-stable condition of the slope. This suggests that the fluvio-glacial erosion and glacial loading and unloading history provoked internal slide mass deformation and damage, leading to a strength degradation process in the rock masses. To enable kinematic release leading the slope to fail, a horizontal acceleration  $a$  due to a seismic event was considered in the simulation. Parametric analysis showed that the critical  $a$  value needed to reach unstable conditions ( $\text{FoS} < 1$ ) is 0.1, mimic a low magnitude earthquake. Given the proximity of the study area to an active seismogenic fault (Inn Valley fault; historic event around  $M_r = 7$ ), can be consider a seismic event as a realistic trigger for the Ridnaun rock avalanche. However, finite element simulation allows only an overall definition of the mechanical behavior of the slope, but impede any further detailed analyses on the key stages of progressive failure and fracture propagation at the slope scale responsible of the failure. To overcome this issue, the hybrid FEM/DEM Elfen code was used during my visit period at the Simon Fraser University in Vancouver (B.C., Canada). Elfen models clearly demonstrate that the glacial history (erosion and loading/unloading cycles) induce a damage accumulation process concentrated in the micaschists units, up to a depth of around 100 m. This result indicates that the glacial history of the valley act as a predisposing factor, initiating unstable fracture propagation in the intact rock. Pre-existing discontinuities at the slope scale, due to their unfavorable orientation to control gravitational instabilities, do not have any major effect on fracture nucleation and propagation, indicating that fracturing process involved entirely the intact rock domains. In addition, none of the models suggests the development of a critical failure surface at the base of the deforming area but, on the contrary, an intense internal fracturing and rock mass disruption confined into intact rock domains. In this scenario, even a low magnitude seismic event could enable the slope failure, which, as a result of the high degree of fracturing, will be rock avalanche in type.

## 6.5 Figure Captions

Figure 6.1: Finite-element continuum modelling of glacial loading and unloading process. The staged simulation includes: a) initial bedrock conditions, b) shaping of the valley through glaciation and replacement of the rock by glacial ice; c) retreat of glacier in 5 stages;

Figure 6.2: N – S topographic profile of the Ridnaun valley;

Figure 6.3: Finite – element Phase<sup>2</sup> simulation. The images referre to continuum modelling of glacial erosion and unloading process on basal shear zone development; a) Shear strain distribution; b) shear strain distribution coupled with yielding elements.

Figure 6.4: Finite – element Phase2 simulation. The images referre to continuum modelling of seismic effect on basal shear zone development and stability of the studied slope; a) Shear strain distribution; b) shear strain distribution coupled with yielding elements.

Figure 6.15: Hybrid finite/discrete – element model employing a Mohr – Coulomb with Rankine tensile cut – off, showing a progressive fracturing widely distributed below the glacial shoulder.

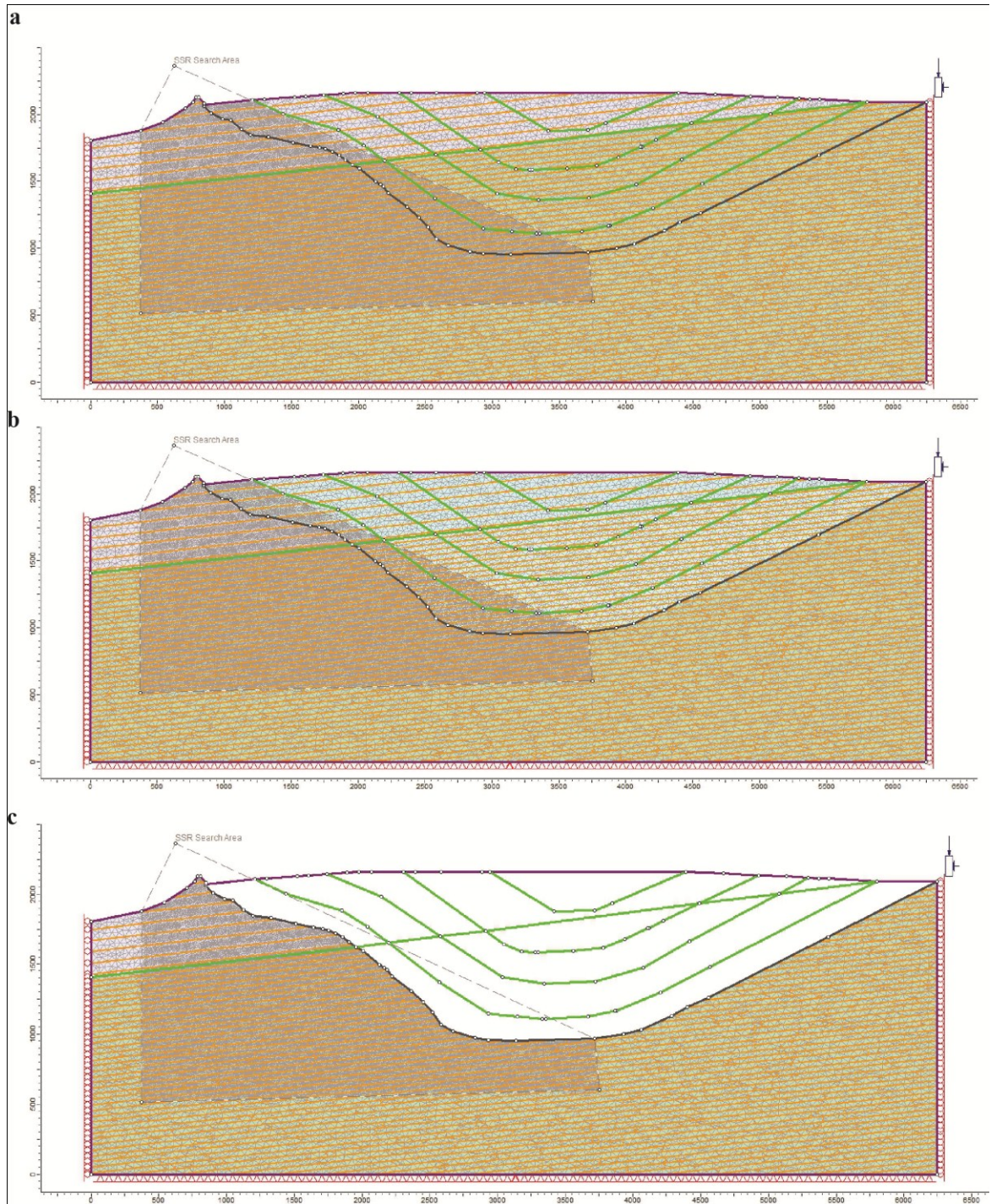


Figure 6.1



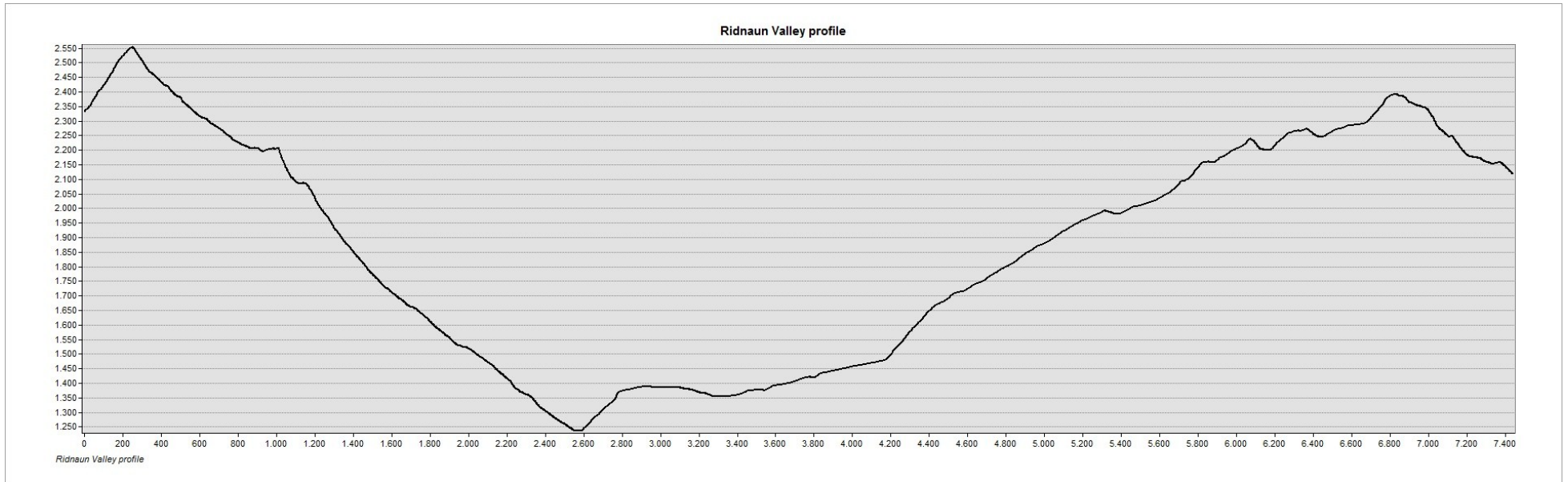


Figure 6.2



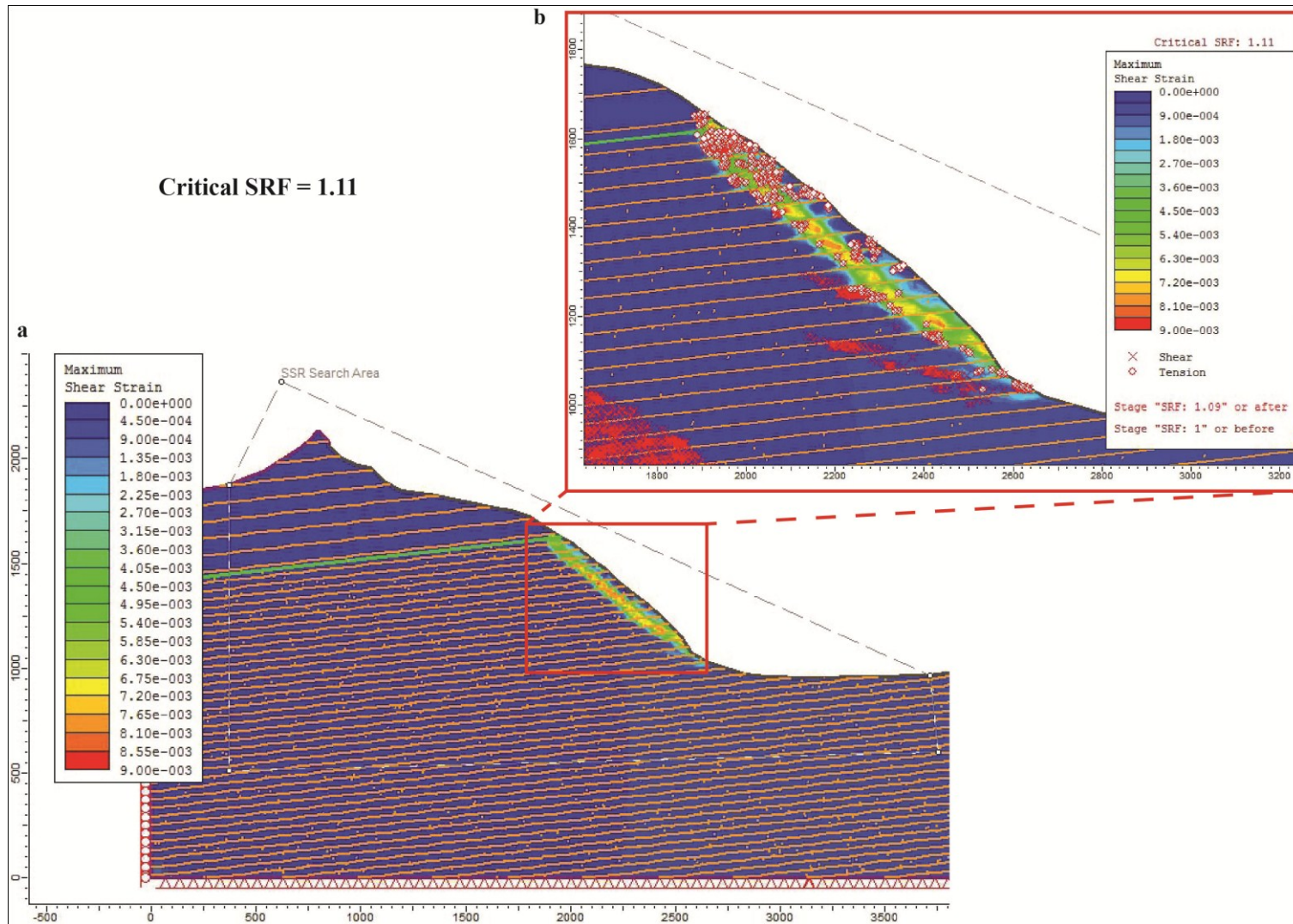


Figure 6.3

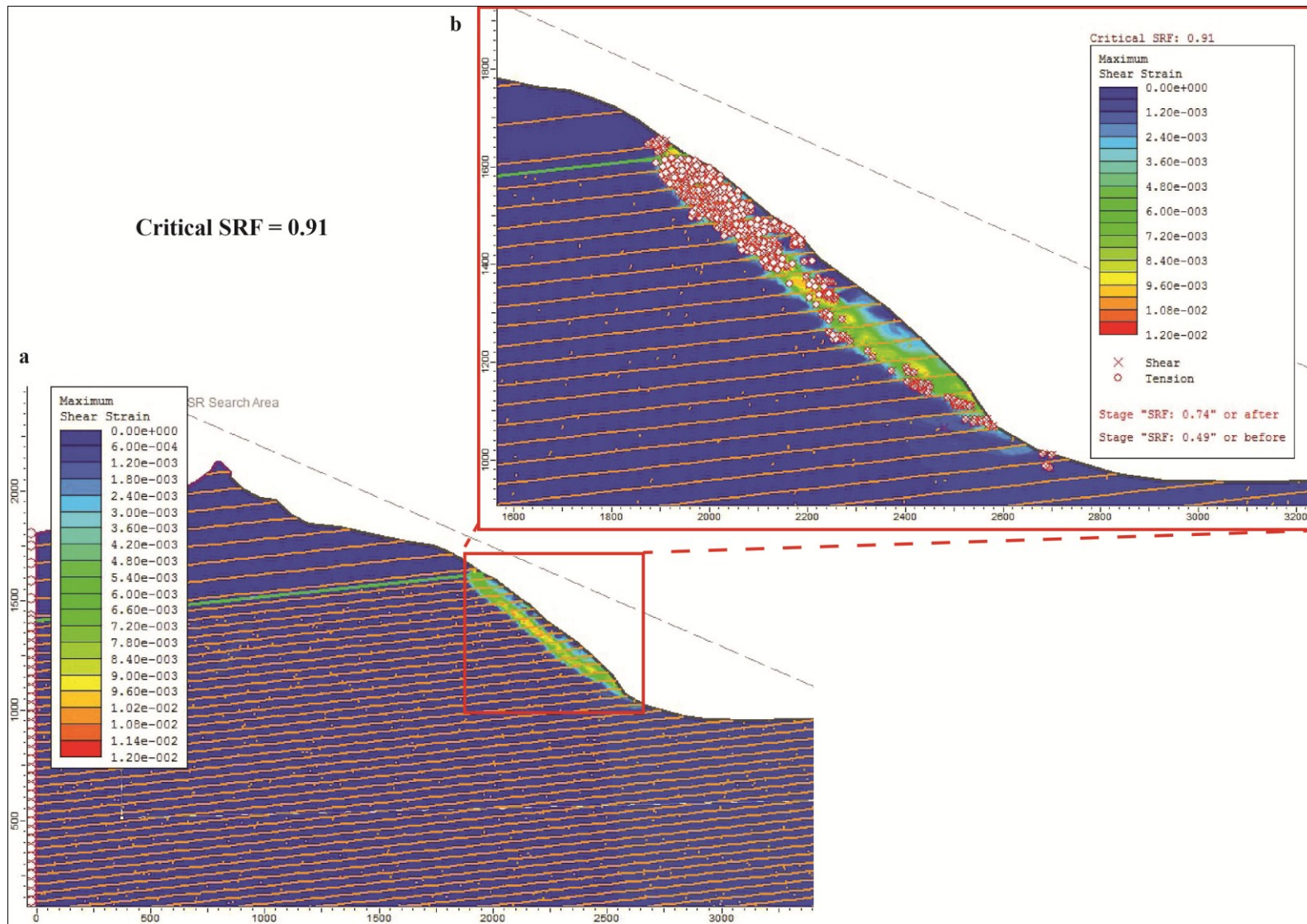


Figure 6.4

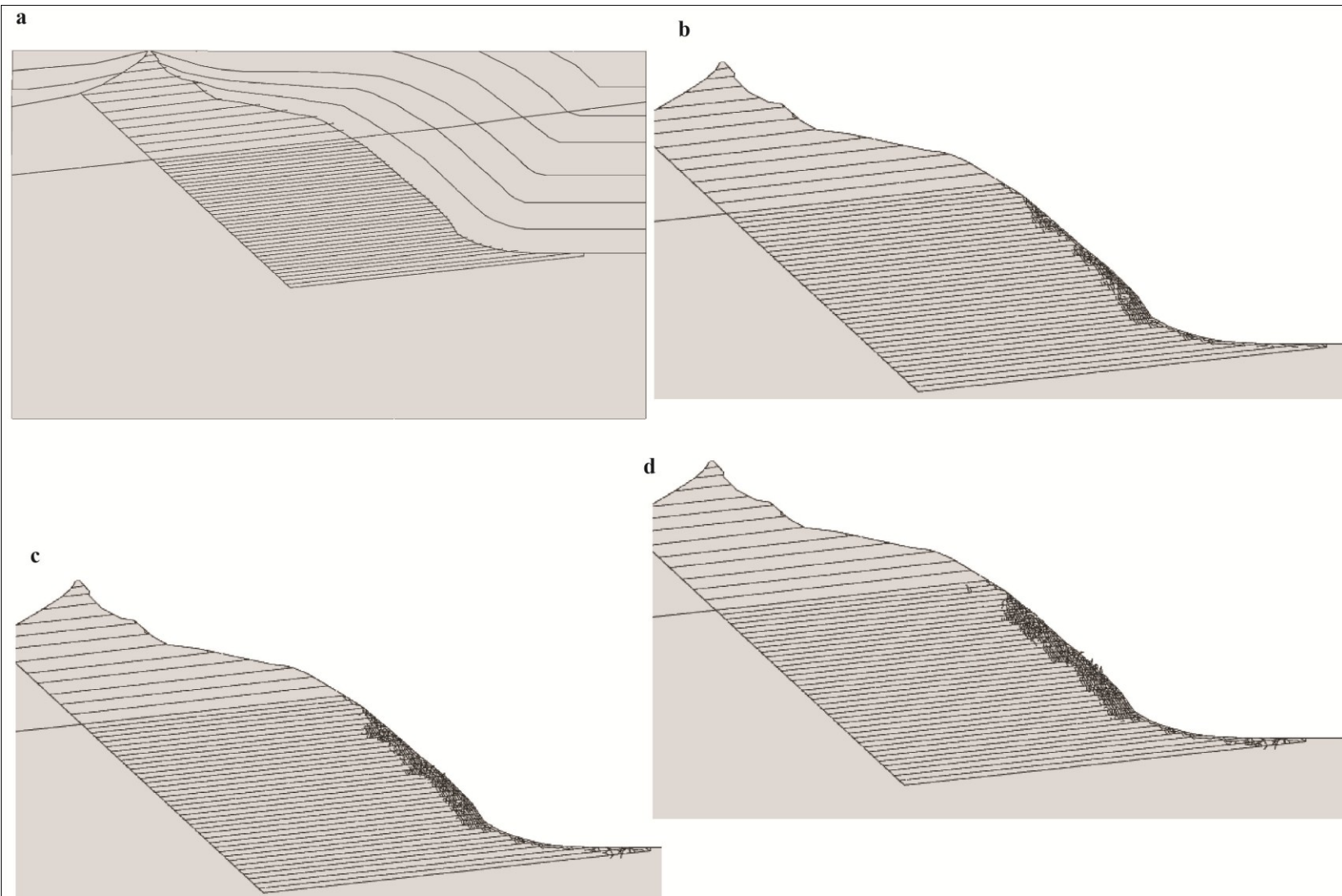


Figure 6.5

## 7. Conclusions

The left slope of the Ridnaun Valley (Sterzing/Vipiteno, South Tyrol, Italy), set on the crystalline units of the Austoalpine Nappe of the alpine orogenic wedge, shows evidence of quaternary gravitational evolution which highly depends on the interaction between the slope trend and the brittle/ductile structural setting. The multidisciplinary approach used in this work aids the understanding of the Quaternary differential evolution of the slope. The results obtained by field work and the analysis of the LiDAR-derived digital elevation model clearly revealed different gravitational movements. A fully evolved gravitational collapse, having the typical features of a rock avalanche, characterizes the central part of the slope; whereas to the east and west of the rock avalanches, deep seated gravitational slope deformations, pointed out for the first time with this work, still involve the slope. The rock avalanche, whose deposit covers an area of about 2.4 km<sup>2</sup>, had obstructed the valley, resulting in a rock avalanche – dammed lake. An ongoing gravitational deformation involves the uphill sections of the slope, next to the crown area. In addition, to the West and the East of the rock avalanche, morphostructural features as scarps – counterscarps, trenches are evident. PS and DS - SAR (Synthetic Aperture Radar) interferometry data (derived ERS, ENVISAT and RADARSAT scenes), kindly given by the Geological Survey of the Autonomous Province of Bolzano, testify an ongoing movement on both the DSGSDs bordering the rock avalanche, highlighting a most unstable area at the Western sector. Glacial unloading is to be considered as the most probable trigger for the detected DSGSDs, whereas a seismic trigger can be hypothesized for the Ridnaun rock avalanche.

The slope is carved within the paragneiss rocks of the Oetztal - Stubai Unit and the garnet-micaschists of the Schneeberg/Monteneve Unit. These two units are separated by a NNW gentle dipping tectonic contact, which obliquely intersects the E–W slope, and is well described by ultracataclastic and mylonitic layers following the regional low angle north-dipping foliation. Approaching to the tectonic contact, relicts of an ancient foliation within the regional S<sub>1</sub> foliation in the ÖSC are defined by folds with sub-horizontal E–trending axes. The folds induce the change in the dip direction of the regional schistosity in the ÖSC from N dipping to SE dipping. NNE–SSW and N–S trending faults, having a mean 1 m thick incoherent fault breccia, affect the entire slope. On one hand the recognized fault network together with the K1 discontinuity set, act as lateral release of the unstable areas; on the other hand, the small – scale folds in S<sub>1</sub>

domain within the ÖSC coupled with the non – parallelism between the tectonic contact trend and the slope, ease the DSGSD formation and evolution (Wetterspitz DSGSD), and acted as releasing factor for the crown area of both the rock avalanche and the Telfer Weissen DSGSD. The purely brittle deformation of the ÖSC mainly in the rock avalanche and the Telfer Weissen DSGSD, is interpreted to be driven by a brittle/plastic deformation of the garnet micaschists of the SMU, throughout a widely distributed micro-cracking of rock mass. Metamorphic anisotropy, such as shear band cleavages, crenulation cleavage, garnet porphyroblasts and reaction rims, has to be considered as site for micro-cracking nucleation and propagation through the rock mass. In fact, microscale analyses done on thin sections on field samples and laboratory samples, on which U tests were performed, of the garnet micaschists show that the metamorphic anisotropy (crenulation cleavage, porphyroblasts, have a strong effect on fracture nucleation and propagation. Foliation planes, crenulation cleavage and C' - type shear band cleavages act as nucleation sites, allowing the fracture nucleation and propagation through grain boundaries of micaceous minerals (mainly muscovite and biotite). High strength domains expressed by garnets and reaction rims perturb the local stress field, triggering the fracture initiation in the surrounding foliation planes and shear band cleavages. This will cause intense microcracking within intact rock leading the rock to fail through multiple fracture planes than via single failure plane.

Thus, the three recognized rock slope instabilities can be interpreted as three different stages of the same evolutionary path, driving a creeping deforming rock mass into a rock avalanche-type failure. The Telfer Weissen DSGSD, due to similar structural setting and dimensions, has to be considered as the pre-failure condition of the Ridnaun rock avalanche. Indeed, to investigate the trigger mechanisms responsible for the failure, key stages of progressive failure and fracture propagation along the slope responsible for the ongoing creeping brittle/plastic deformation driving both the pre-failure stage of the Ridnaun rock avalanche and the ongoing DSGSDs, a back - analysis through FEM and hybrid FEM / DEM numerical modeling technique on the Ridnaun rock avalanche was performed.

Finite difference analyses using Phase2 confirm the starting hypothesis: the erosion history and the cyclical glacial loading due to Pleistocene glaciations, induce on one hand a plastic deformation (mainly shear type deformation) among SMU; on the other hand the gneisses of the OSC react in a more brittle way through the formation of discrete tensile domains expressed in the field by scarps and counterscarps. The mean Factor of Safety (FoS) coming from the analyses is 1.12, indicating a quasi-stable



condition of the slope. This suggests that the fluvio-glacial erosion and glacial loading and unloading history provoked internal slide mass deformation and damage, leading to a strength degradation process in the rock masses. To enable kinematic release leading the slope to fail, a horizontal acceleration  $a$  due to a seismic event was considered in the simulation. Parametric analysis showed that the critical  $a$  value needed to reach unstable conditions ( $FoS < 1$ ) is 0.1, mimic a low magnitude earthquake. Given the proximity of the study area to an active seismogenic fault (Inn Valley fault; historic event around  $M_r = 7$ ), can be consider a seismic event as a realistic trigger for the Ridnaun rock avalanche. However, finite element simulation allows only an overall definition of the mechanical behavior of the slope, but impede any further detailed analyses on the key stages of progressive failure and fracture propagation at the slope scale responsible of the failure. To overcome this issue, the hybrid FEM/DEM Elfen code was used. Elfen models clearly demonstrate that the glacial history (erosion and loading/unloading cycles) induce a damage accumulation process concentrated in the micaschists units, up to a depth of around 100 m. This result indicates that the glacial history of the valley act as a predisposing factor, initiating unstable fracture propagation in the intact rock. Pre-existing discontinuities at the slope scale, due to their unfavorable orientation to control gravitational instabilities, do not have any major effect on fracture nucleation and propagation, indicating that fracturing process involved entirely the intact rock domains. In addition, none of the models suggests the development of a critical failure surface at the base of the deforming area but, on the contrary, an intense internal fracturing and rock mass disruption confined into intact rock domains. In this scenario, even a low magnitude seismic event could enable the slope failure, which, as a result of the high degree of fracturing, will be rock avalanche in type.

Thus, the intense microcracking at the sample scale controlled by metamorphic anisotropy, coupled with the unfavorable orientation of the regional foliation and the brittle discontinuity network at slope scale, impede the formation of a well-developed failure surface, inducing the slope to evolve into a rock avalanche type failure.



## 8. References

- Agliardi, F., Crosta, G.B., Zanchi, A., 2001. Structural constraints on deep seated slope deformation kinematics. *Eng. Geol.*, **59**, 83 – 102.
- Agliardi, F., Crosta, G.B., Zanchi, A., Ravazzi, C., 2009. Onset and timing of deep-seated gravitational slope deformations in eastern Alps, Italy. *Geomorphology*, **103**(2009) 113-129.
- Agliardi, F., Crosta, G.B., Frattini, P., 2012. Slow rock-slope deformation. In: Clague, J.J., Stead, D., 2012. *Landslides: type, mechanism and modeling*. Cambridge University Press.
- Akai, K., 1971. The failure surface of isotropic and anisotropic rocks under multiaxial stresses. *J. Soc. Mater. Sci. Japan*. **20**:122 – 128.
- Ambrosi, C., Crosta, G.B., 2006. Large sackung along major tectonic features in the Central Italian Alps. *Eng. Geol.* **83**, 183-200.
- Ambrosi, C., Crosta, G.B., 2011. Valley shape influence on deformation mechanisms of rock slopes. In: Jaboyedoff, M., 2011. *Slope Tectonic*. Geological Society, London, Special Publications, **351**, 215-233.
- Ampferer, O., 1939. Über einige Formen der Bergzerreissung. *Sitzungsberichte der Akademie der Wissenschaften Wien. Mathematisch - Naturwissenschaftliche Klasse*, **148**, 1-14.
- Apuani, T., Masetti, M., Rossi, M., 2007. Stress-strain-time numerical modeling of a deep-seated gravitational slope deformation: preliminary results. *Quaternary international* **171-172** (2007) 80-89
- ASTM. Standard method for determination of the point load strength index of rock. ASTM Standards on Disc 04.08. 2001 Designation D5731.



- Augustinus, P.C., 1995. Glacial valley cross-profile development: the influence of in situ rock stress and rock mass strength, with examples from the southern Alps, New Zealand. *Geomorphology*, **14**, 87-97
- Ballantyne, C.K., 2002. Paraglacial geomorphology. *Quaternary Science Reviews* 21 (2002) 1935-2017.
- Bargossi, G.M., Bove, G., Cucato, M., Gregnanin, A., Morelli, C., Moretti, A., Poli, S., Zanchetta, S., Zanchi, A., Ambrosi, C., Cortini, P., Crottini, A., Macconi, P., Mair, V., Marocchi, M., Montesor, L., Toffolon, G., Tumiatì, S., 2011. Note illustrative della Carta Geologica d'Italia alla scala 1:50.000 – foglio 13 Merano. ISPRA – Istituto Superiore per la protezione e la ricerca ambientale.
- Barton, N., 2002. Some new Q-value correlations to assist in site characterization and tunnel design. *International Journal of Rock Mechanics and Mining Sciences* 39 (2002) 185-216
- Barton, N., Lien, R., Lunde, J., 1974. Engineering classification of rockmasses for the design of tunnel support. *ROck Mech* 1974;6(4):189-236
- Barton, N., Choubey, V., 1977. The shear strength of rock joints in theory and practice. *Rock Mechanics*, 1/2: 1-54 (also in Norwegian Geotechnical Institut, Publication No.119).
- Barton, N., Pandey, S. K., 2011. Numerical modeling of two stoping methods in two Indian mines using degradation of c and mobilization of  $\phi$  based on Q-parameters. *International journal of rock mechanics and mining sciences* 48 (2011) 1095-1112.
- Basu, A., 2008. The point load test in rock material characterization. *J. Eng. Geol.* 53:379 – 87.
- Basu, A., Kamran, M., 2010. Point load test on schistose rocks and its applicability in predicting uniaxial compressive strength. *Int. J. of Rock Mech. And Min. Scie.* 47:823 – 828.

- Bestmann, M., Pennacchioni, G., Frank, G., Göken, M., de Wall, H., 2011. Pseudotachylyte in muscovite-bearing quartzite: coseismic friction-induced melting and plastic deformation of quartz. *Journal of Structural Geology* 33 (2011), 169-186.
- Behrestaghi, M.H.N, Seshagiri Rao K., Ramamurthy, T., 1996. Engineering geological and geotechnical responses of schistose rocks from dam project areas in India. *Engineering Geology* 44 (1996) 183 – 201.
- Bistacchi, A., Massironi, M., 2001. Introduzione alla tettonica fragile neoalpina e sua influenza sull'instabilità dei versanti. In: *Tettonica recente ed instabilità dei versanti nelle Alpi Centrali*. (Ed. Pasquarè G.), CNR and Fondazione Cariplo spec. Publ., 9-33.
- Bieniawski, Z. T., 1976. Rock mass classification in rock engineering. In: *Bieniawski, Z. t., 1976. Exploration for rock engineering, Proc. Symp. Vol.1, Cape town, Balkema, pp. 97-106*
- Bonzanigo, L., Eberhardt, E., Löw, S., 2007. Long - term investigation of a deep - seated creeping landslide in crystalline rock. Part 1. Geological and hydromechanical factors controlling the Campo Vallemaggia landslide. *Canadian Geotechnical Journal*, 44, 1157 - 1180.
- Bouissou S., Damault A., Chemenda A., Rolland Y., 2012 – Evolution of gravity-driven rock slope failure and associated fracturing: Geological analysis and numerical modeling. *Tectonophysics*.
- Bovis, M.J., 1982. Uphill-facing (antislope) scarps in the Coast Mountains, southwest British Columbia. *Geological Society of America Bulletin* 93, 804 – 812.
- Brideau, M., A., 2005. The influence of tectonics structures on rock mass quality and implication for rock slope stability. Bachelor of Science (Honors) – Simon Fraser University 2002

- Brideau M.A., Yan M., Stead D., 2009. The role of tectonic damage and brittle rock fracture in the development of large rock slope failure. *Geomorphology* 103(2009) 30-49.
- Brigo, L., 1965. Il giacimento a Pb-Zn di S. Martino di Monteneve in Alto Adige. *L'ind. Min. den Trentino Alto Adige* 2, 63-118.
- Brook, N., 1985. The equivalent core diameter method of size and shape correction in point load testing. *Int J Rock Mech. Min. Sci. Geomech. Abstr*; 1985; 22:61 – 70.
- Cai, M., Kaiser, K.P., 2004. Numerical simulation of the Brazilian test and tensile strength of anisotropic rocks and rocks with pre-existing cracks. In: *Proceedings of the SINOROCK international symposium on rock mechanics: rock characterization, modeling and engineering design methods*, 18 – 21 May, Three Gorges Project site, China. Paper 2B – 03.
- Caine, N., 1982. Toppling failures from alpine cliffs on Ben Lomond, Tasmania. *Earth Surface Processes and Landforms* 7, 133 – 152.
- Caporali, A., Braitemberg, C., Massironi, M., 2005. Geodetic and hydrological aspects of the Merano earthquake of 17 July 2001. *Journal of Geodynamics*, 39:317-336.
- Cargill, J.S., Shakoor, A., 1990. Evaluation of empirical methods for measuring the uniaxial compressive strength of rock. *Int. J. Rock Mech. Min. Sci. Geomech. Abstr.* 27:495 – 503.
- Castaldini, D., Panizza, M., Slejko, D., 1992. Breve illustrazione di un contributo al sottoprogetto ILP “ Carta del mondo delle principali faglie attive “ per l'Italia Settentrionale. *Il Quaternario*, 5(2): 287-292.
- Chigira, M., 1992. Long - term gravitational deformation of rocks by mass rock creep. *Engineering geology*, 32, 157 - 184.

- Chigira, M., Kiho, K., 1994. Deep - seated rockslide - avalanche preceded by mass rock creep of sedimentary rocks in the Akaishi Mountains, central Japan. *Engineering Geology*, 38, 221 - 230.
- Coggan J.S., Pine R.J., Stead D. and Rance J.M. 2003. Numerical modelling of brittle rock failure using a combined finite-discrete element approach: implications for rock engineering design. In: Proc. of 10th Congress of the ISRM Technology Roadmap for Rock Mechanics. South Africa. Published by The South African Institute of Mining and Metallurgy.
- Coggan J.S. and Stead D., 2005. Numerical modelling of the effects of weak mudstone on tunnel roof behaviour. In: Proc. 58<sup>th</sup> Canadian Geotechnical Conference. Saskatoon. Canada. Paper GS502. 9 pages.
- Crosta, G.B., 1996. Landslide, spreading, deep seated gravitational deformation: analysis, examples, problems and proposals. *Geog. Fis., Dinam. Quat.* 19(2), 297-313.
- Crosta, G.B., Agliardi, F, 2003. Failure forecast for large rock slides by surface displacement measurements. *Canadian Geotechnical Journal* **40**, 176-191.
- Crosta, G.B., Zanchi, A., 2000. deep - seated slope deformations: huge, extraordinary, enigmatic phenomena. In: Bromhead, B., Dixon, N., Ibsen, M. L., 2000. *Landslides in research, theory and practise*. London: Thomas Telford. pp. 351 - 358.
- Cruden, D.M., Martin, C.D., 2004. Before the Frank Slide: preparatory and triggering causes from maps and photographs. *Proceedings 57<sup>th</sup> Canadian Geotechnical Conferences, GeoQuébec 2004*.
- Deere, D.U., Miller, R.P., 1966. Engineering classification and index properties for intact rock. AFWL-TR-65-116, Air Force Weapons Laboratory. 300 pp.
- Deklotz, E.J., Brown, J.W., Sternler, O.A., 1966. Anisotropy of a schistose gneiss. *Proc. 1<sup>st</sup> Cong.Int.Soc.Rock mech., Lisbon, I:465 – 470*.

- Diederichs M.S. 1999. Instability of Hard Rock masses: The Role of Tensile Damage and Relaxation. PhD Thesis. University of Waterloo.
- Diederichs, M., 2007. The 2003 Canadian Geotechnical Colloquium: mechanistic interpretation and practical application of damage and spalling prediction criteria for deep tunneling. *Can. Geotech. J.*, 44: 1082 – 1116.
- Diederichs M.S., Coulson A., Falmagne V., Rizkalla M. and Simser B. 2002. Applications of rock damage limits to pillar analysis at Brunswick Mine. In: *Proc. 5<sup>th</sup> North Am. Rock Mech. Symp. & 17<sup>th</sup> Tunn. Assn Can. Conf.*, Toronto. Univ. Toronto Press: Toronto. pp 1325-1332.
- Diederichs, M.S., Lato, M., Hammah, R.E., Quinn, P., 2007. Shear Strength Reduction (SSR) approach for slope stability analysis. In: Eberhardt, E., Stead, D., Morrison, T., (Eds), 2009. *1st Canada – U.S. Rock Mechanics Symposium: meeting society's challenges and demands*. Vancouver, Taylor & Francis / Balkema. 1: Fundamentals, New Technologies & new ideas, pp. 319 – 327.
- Dincer, I., Acar, A., Cobano, I., Uras, Y., 2004. Correlation between Schmidt Hardness, Uniaxial Compressive Strength and Young's Modulus for Andesites, Basalts and Tuffs. *Bulletin of Engineering Geology and Environment*, 63(2):141-148.
- Eberhardt E., Stead D., Coggan J.S., 2004 – Numerical analysis of initiation and progressive failure in natural rock slopes – the 1991 Randa rockslide. *International Journal of Rock Mechanics and Mining Sciences* 41 (2004) 69-87.
- Eberhardt E., 2008 – Twenty-ninth Canadian Geotechnical Colloquium: The role of advanced numerical methods and geotechnical field measurements in understanding complex deep-seated rock slope failure mechanisms. *Can. Geotech. J.*, 45:484-510 (2008).

- Elmo, D., Coggan, J.S., Pine, R.J., 2005. Characterization of rock mass strength by combination of field mapping and numerical modeling. In: Proceedings of the 40<sup>th</sup> US rock mechanics symposium, Anchorage, Alaska.
- Elmo, D., 2006. Evaluation of a hybrid FEM/DEM approach for determination of rock mass strength using a combination of discontinuity mapping and fracture mechanics modeling, with particular emphasis on modeling of jointed pillars. Ph. D. Thesis. Camborne School of Mines. University of Exeter.
- Elmo, D., Stead, D., An integrated numerical modelling-discrete fracture network approach applied to the characterization of rock mass strength of naturally fractured pillars. *Rock Mech. Rock Eng* (2010) 43:3-19;
- Fang, Z., Harrison, J.P, 2002. A mechanical degradation index for rock. *Int. J. Rock Mech. and Min. Sci.* Vol. 38. pp. 1193-1199.
- Forcella, F., Gallazzi, D., Montrasio, A., Notarpietro A., 1982. Note illustrative relative all'evoluzione neotettonica dei Fogli 6- Passo della Spluga, 7 – Pizzo Bernina, 8- Bormio, 17 – Chiavenna, 18 – Sondrio, 19 – Tirano. In: “Contributi conclusivi per la realizzazione della Carta Neotettonica d'Italia”, 513: 239-288.
- Förster, H.,G., 1963. Die Blei-Zink-Lagerstätte Schneeberg in Südtirol. *Inst. Für Mineralogie und Lagerstättenkunde der TH Aachen* 126p.
- Frizzo, P., 1976. La serie metallifera delle Breonie affiorante nelle valli Ridanna e Fleres, in Alto Adige. Mineralizzazioni a Pb-Zn “primarie” e loro mobilizzazione nei marmi del Complesso di Monteneve a sud delle Cime Bianche di Telves. *Studi Tridentini di Scienze Naturali*, nuova serie 53, 70-106.
- Frizzo, P., Mills, J., Visonà, D., 1982. Ore petrology and metamorphic history of Pb-Zn ores, Monteneve, Tyrol, N. Italy. *Mineralium Deposita* 17, 333-347.
- Frizzo, P., 2002. Carta geomineraria del distretto metallifero di S.Martino di Monteneve-Fleres, scala 1:25000. SELCA, Firenze.

- Ghosh, D.K., Srivastava, M., 1991. Point – load strength: an index for classification of rock material. *Bull Eng Geol Env.* 44: 27 – 33.
- Ghirotti, M., Martin, S., Genevois, R., 2011. The Celentino deep - seated gravitation slope deformation (DSGSD): structural and geomechanical analyses (Peio Vallei, NE Italy). In: Jaboyedoff, M., 2011. *Slope Tectonic*. Geological Society, London, Special Publications, **351**, 235-251.
- Golts, S., Rosenthal, E., 1993. A morphotectonic map of the northern Arava in Israel, derived from isobase lines. *Geomorphology* 7, 305 – 315.
- Greco, R., Sorriso-Valvo, M., 2005. Relationship between joint apparent separation, schmidt hammer rebound value, and distance to faults in rocky outcrops, Calabria, southern Italy. *Engineering geology*, 43:371-384.
- Groneng G., Lu M., Nilsen B., Jenssen A., 2010. Modelling of time-dependent behavior of the basal sliding surface of the Aknes rockslide area in western Norway. *Engineering Geology* 114 (2010) 414-422.
- Gudmundsson, A., 2011. *Rock fractures in geological processes*. Cambridge University Press.
- Hajiabdolmajid, V., 2001. Mobilization of strength in brittle failure of rock. Ph. D. thesis, Queen's University, Kinston, Canada.
- Hajiabdolmajid, V., Kaiser, P.K., Martin, C.D., 2002. Modelling brittle failure of rock. *International journal of rock mechanics and mining sciences*; 39 (2002) 731 – 741
- Hajiabdolmajid, V., Kaiser, P., 2003. Brittleness of rock and stability assessment in hard rock tunneling. *International journal of rock mechanics and mining sciences*,
- Hammah, R.E, Yacoub, T.E., Corkum, B.C., Curran, J.H., 2005. The shear strength reduction method for the generalized Hoek – Brown criterion. *ARMA/USRMS* 05 – 810.

- Hart, R.D., 1993. An Introduction to Distinct Element Modelling for Rock Engineering. In: Comprehensive Rock Engineering. Vol. 2. Ed. J.A. Hudson. Pergamon. pp. 245-261
- Hoek, E., 1994. Strength of rock and rock masses. *ISRM News J* 2:4-16
- Hoek, E., 2006. *Practical Rock Engineering*.
- Hoek, E., and Bray, J., 1977. *Rock slope engineering*, 1st edn, IMM, London.
- Hoek, E., Diederichs, M.S., 2006. Empirical estimation of rock mass modulus. *International journal of rock mechanics & mining sciences* 43 (2006) 203 – 215.
- Hoek, E., Kaiser, P.K., Bawden, W.F., 1998. *Support of underground excavation in hard rock*. Rotterdam: A.A. Balkema.
- Hoek, E., Karzulovic, A., 2000. Rock mass properties for surface mines. In: Hustrlid, W.A., McCarter M. K., van Zyl, D.J.A., 2000. *Slope stability in surface mining*, Littleton, Colorado: Society for Mining, Metallurgical and Exploration (SME), pages 59-70.
- Hoek, E., Marinos, P., Benissi, M, 1998. Applicability of the geological strength index (GSI) classification for very weak and sheared rock masses. The case of the Athens Schist Formation. *Bull Eng Geol Env* (1998) 57:151-160.
- Hürlimann, M., Ledesma, A., Corominas, J., Prat, P.C., 2006. The deep-seated slope deformation at Encampadana, Andorra: representation of morphologic features by numerical modelling. *Engineering Geology* 83 (2006) 343 - 357.
- ISRM, Suggested method for determination of the point load strength, 1985. *Int. J. Rock Mech. Min. Sci. Geomech Abstr.* 22: 51 – 60.
- Jaboyedoff, M., Couture, R., Locat, P., 2009. Structural analysis of Turtle Mountain (Alberta) using digital elevation model: toward a progressive failure. *Geomorphology* 103 (2009) 5 – 16.



- Jaboyedoff, M., Baillifard, F., Couture, R., Locat, J., Locat, P., 2004a. Toward preliminary hazard assessment using DEM topographic analysis and simple mechanic modeling. In: Lacerda, W.A., Ehrlich, M., Fontoura, A.B., Sayo, A. (Eds.) 2004. Landslides evolution and stabilization, Balkema, Rotterdam, pp. 191-197.
- Jaboyedoff, M., Pedrazzini, A., Horton, Loye, A., Surace, I. 2008. Preliminary slope mass movements susceptibility mapping using LiDAR DEM. In Proceedings of 61th Canadian Geotechnical Conference, pp 491-426.
- Jaboyedoff, M., Oppikofer, T., Derron, M.H., Blikra, L. H., Böhme, M., Saintot, A., 2011. Complex landslide behavior and structural control: a three-dimensional conceptual model for Åknes rockslide, Norway. *Geol. Soc. Spec. Publ.*, 351, 147-161.
- Jaboyedoff, M., Oppikofer, T., Abellán, A., Derron, M., Loye, A., Metzger, R., Pedrazzini, A., 2012. Use of LIDAR in landslide investigations: a review. *Nat. Hazards*(2012) 61:5-28; DOI 10.1007/s11069-010-9634-2.
- Jing L. 2003. A review of techniques, advances and outstanding issues in numerical modelling for rock mechanics and rock engineering. *Int. J. Rock Mech. Min. Sci.* Vol. 40. pp. 283-353.
- Jing L. and Hudson J.A. 2002. Numerical methods in rock mechanics. *Int. J. Rock Mech. Min. Sci.* Vol. 39. pp. 409-427.
- Kahle, H.G., Geiger, A., Buerki, B., Gubler, E., Marti, U., Rothacher, M., Gurtner, W., Beutler, G., Bauerisma, I., Pfiffner, O.A., 1997. Recent crustal movements, geoid and density distribution; contribution from integrated satellite and terrestrial measurements. In: Results of NRP 20; deep structures of the Swiss Alps. Birkhaeuser Verlag, Basel.

- Kahraman, S., 2001. Evolution of simple methods for assessing the uniaxial compressive strength of rock. *International journal of Rock Mechanics and Mining Sciences*; 38: 981-994.
- Kellerer-Pirklbauer, A., Proske, H., Strasser, V., 2010. Paraglacial slope adjustment since the end of the Last Glacial Maximum and its long-lasting effects on secondary mass wasting processes: Hauser Kaibling, Austria. *Geomorphology* 120 (2010) 65-76.
- Kemeny, J., 2003. The time-dependent reduction of sliding cohesion due to rock bridges along discontinuities: a fracture mechanics approach. *Rock mechanics and rock engineering* (2003) 36(1), 27-38.
- Kinakin, D., Stead, D., 2005. Analysis of the distribution of stress in natural ridge forms: implications for deformation mechanisms of rock slopes and the formation of sakung. *Geomorphology*, 65, 85-100.
- Klebensberg, R. v., 1958. Südtiroler geomorphologische Studien. Das obere Eisacktal. Verlag des Amtes für Landeskunde - Remagen, Tiroler Graphik, Innsbruck, Gr.-8°, 112 pp.
- Klerck P.A. 2000. The finite element modelling of discrete fracture in quasi-brittle materials. PhD thesis. University of Swansea - Wales.
- Klerck P.A., Sellers E.J. and Owen D.R.J. 2004. Discrete fracture in quasi-brittle materials under compressive and tensile stress states. *Comput. Methods Appl. Mech. Engrg.* Vol. 193. pp 3035-3056.
- Leith, K.J., 2012. Stress development and geomechanical controls on geomorphic evolution of alpine valleys. Ph.D. Thesis. ETH Zurich.
- Leroueil, S., 2001. Natural slopes and cuts: movement and failure mechanisms. *Geotechnique*, 51, 197 – 243.

- Löw, S., Gischig, V., Willenberg, H., Alpiger, A., Moore, J.M., 2012. Randa: kinematics and driving mechanisms of a large complex rockslide. In: Clague, J.J., Stead, D., 2012. Landslides: types, mechanisms and modeling. Cambridge University Press – pp 144-171.
- Mahr, T., Nemcok, A., 1977. Deep - seated creep deformations in the crystalline cores of the Tatry Mts. Bulletin of the International Association of Engineering Geology, 16, 104 - 106.
- Marinos, P., Hoek, E., 2000. GSI: a geologically friendly tool for rock mass strength estimation. Proceedings of GeoEng 2000 Conference, Melbourne, Australia.
- Massironi, M., Bistacchi, A., Dal Piaz, G.V., Monopoli, B., Schiavo, A., 2003. Structural control on mass-movement evolution: a case study from the Vizze Valley, Italian Eastern Alps. *Eclogae geol. Helv.*, **96**, 85-98.
- Massironi, M., Genevois, R., Stefani, M., Floris, M., 2010. How an antiformal structure may influence a large mass movement on foliated metamorphic rocks: the case of Passo Vallaccia DSGSD (Eastern Italy Alps) investigated through 2D distinct element modelling. *Bull. Eng. Geol. Environ.* 70:479-501.
- Martin, C., Chandler, N., 1994. The progressive fracture of Lac du Bonnet granite. *Int. J. Rock Mech. Min. Sci.* 31(6): 643 – 59.
- Martin C.D., Christiansson R. and Soderhall J. 2001. Rock stability considerations for siting and constructing a KBS-3 repository. Swedish Nuclear Fuel and Waste Management SKB. Technical Report TR-01-38.
- Mauracher, J., 1981. Alpidische und voralpische Metamorphose und Strukturpraegung am Westende des Schneebergerzuges (Ötztaler Alpen). *Mitt. Ges. Geol.-Bergbaustud.* 27, 244-245.
- McCabe, W.M., Kroerner, R.M., 1975. High pressure shear strength of an anisotropic mica schists rock. *Int. J., Rock Mech.Min.Sci.*, 12:219-228

- Nasseri, M.H., Rao, K.S., Ramamurthy, T., 1997. Failure mechanism in schistose rocks. Int. J. Rock Mech. & Min. Sci. 34:3-4, paper No. 219
- Nemcok, A., Pasek, J., Rybar, J., 1972. Clasification of landslides and other mass movements. Rock Mechanics, 4, 71 - 78.
- Oppikofer, T., Jaboyedoff, M., Pedrazzini, A., Derron, M.H., Blikra, L.H., 2011. Detailed DEM analysis of a rockslide scar to characterize the basal sliding surface of active rockslide. J. Geophys. Res., 116, F02016, doi:10.1029/2010JF001807.
- Ostermann, M., Sanders, D., Rodnigh, H., 2010. Three rockslides shaped the valleys around Sterzing/Vipiteno, Northern Italy. In: EGU General Assembly, Vienna, Austria, p. 3356.
- Owen D.R.J., Feng Y.T. and Han K.J. 2000. Finite/discrete element analysis of multi/fracture and multi/contact phenomena. In: proc. of VECPAR 2000. Porto. Portugal.
- Owen D.R.J. Feng Y.T., Klerck P.A., Yu J. and Crook A.J.L. 2001. Computational strategies for multi-fracturing solids and particular media. In: proc. of the European conference on Computational mechanics. Cracow. Poland.
- Owen, D.R.J, Pires, F.M., De Souza Neto, E.A., Feng Y.T. 2004 (b). Continuous/discrete strategies for the modelling of fracturing solids. Publication of the Civil & Computational Eng. Centre, University of Wales – Swansea.
- Pagel, H., 1975. Zur Erzführung und Geochemie in den neuerschlossenen Teilen der Blei-Zinkerzlagerstätte Schneeberg/Monteneve in Südtirol/Alto Adige (N.Italien). Diss. Erl. Dokt. Der Freien Universität Berlin, 166p.
- Palmström, A., 2001. Measurement and characterization of rock mass jointing. In: Sharma, V.M., Saxena, K.R., 2001. In – situ characterization of rocks. A.A. Balkema publishers – Lise/Abingdon/Exton(PA)/Tokio.

- Palmström, A., 2005. Measurements of and correlation between block size and rock quality designation (RQD). *Tunnels and Underground Space Tecnily, 20*, 362 – 377.
- Palmström, A., Stille, H., 2010. *Rock engineering*. Eds. Thomas Telford.
- Passchier, C.W., Trouw, R.A.J., 2005. *Microtectonics*, Springer-Verlag, 366pp.
- Pariseau, W.G., 1993. Applications of finite element analysis to mining engineering. In: *Comprehensive rock engineering*. Vol. 1. E.ed J.A. Hudson. Pergamon. pp. 491-522
- Pedrazzini, A., Jaboyedoff, M., Froese, C.R., Langenbeberg, C.W., Moreno, F., 2011. Structural analysis of Turtle Mountain: origin and influence of fractures in the development of rock slope failures. . In: Jaboyedoff, M., 2011. *Slope Tectonic*. Geological Society, London, Special Publications, **351**, 162-183.
- Penck, A., Brückner, E., 1909. *Die Alpen im Eiszeitalter*. Ed. Tauchnitz, 3 Vol., 1200 pp., Leipzig.
- Persaud, M., Pfiffner, O.A., 2004. Active deformation in the eastern Swiss Apls; post-glacial faults, seismicity and surface uplift. *Tectonophysics*, 385 (1-4), pp. 59-84.
- Pine, R.J., Coggan, J.S., Flynn, Z.N., Elmo, D., 2006. The development of a new numerical modeling approach for naturally fractured rock masses. *Rock Mech Rock Eng* 39(5): 395 – 419.
- Prager, C., Zangerl, C., Patzelt, G., Brandner, R., 2008. Age distribution of fossil landslides in the Tyrol (Austria) and its surrounding areas. *Natural Hazard and Earth System Sciences*, 8, 377 - 407.
- Preusser, F., 2004. Towards a chronology of the Late Pleistocene in the northern Alpine Foreland. *Boreas*, **33**, 195 – 210.
- Priest, S.D., Hudson, J.A., 1981. Estimation of discontinuity spacing and tracing length using scanline survey. *Int. J. Rock Mech. Min. Sci. and Geomech Abstr.* 18, 183 – 197.

- Radbruch – Hall, D., 1978. Gravitational creep of rock masses on slopes. In: Voight B., Rockslides and avalanches, 1, natural phenomena - developments in geotechnical engineering. Elsevier(Amsterdam) 14(17):607-657
- Ramamurthy,T.,1993. Strength and modulus response of anisotropic Rocks. In: Hudson, J.A.(Editor), 1993. Comprehensive Rock Engineering. Chapt 13, Pergamon, UK, 1:315-330.
- Rockfield, 2008. ELFEN 2D/3D numerical modeling package, version 4.4.2. Swansea: Rockfield software Ltd.; 2007.
- Rocscience, 2004. A new era in slope stability analysis: Shear Strength Reduction Finite Element technique. Rocknews.
- Rocscience, 2008. Analysis and design programs of civil engineering and mining applications. <http://www.rocscience.com> .
- Romana, M., 1985. New adjustment ratings for application of Bieniawski classification to slopes. International Symposium on the role of rock mechanics. ISRM Zacatecas. 49 – 53
- Romana, M., 1993. A geomechanics classification of slopes: Slope Mass Rating. In: Hudson, J. (Eds), 1993. Comprehensive Rock Engineering. Pergamon Press. 3, 575-600.
- Romana, M., 1995. The geomechanic classification SMR for slope correction. Proceedings of the 8<sup>th</sup> International ISRM Congress.
- Sassi, F.P., Cesare, B., Mazzoli, C., Peruzzo, L., Sassi, R., 2004. The cristalline basement of the Italian eastern Alps: a rewiew of rhe metamorphic features. Per. Mineral., **73**, 23-42 SPECIAL ISSUE 2: A showcase of the Italian research in metamorphic petrology.
- Schmertmann, J.H., Osterberg, J.H., 1960. An experimental study of the development of cohesion and friction with axial strain in saturated cohesive soils. Research

- Conference on Shear Strength of Cohesive Soil. Boulder, CO, New York, American Society of Civil Engineers.
- Slejko, D., Carulli, G.B., Nicolich, R., Rebez, A., Zanferrari A., Cavallin, A., Doglioni, C., Carraro, F., Castaldini, D., Iliceto, E., Semenza, E., Zanolla, C., 1982. Seismotectonics of the eastern Southern-Alps: a review. *Boll. Geof. Teor. A.*, 31(122): 109-136.
- Schulson, E.M., 1999. The structure and mechanical behavior of ice. *Minerals Metals Mater Soc* 51(2): 21 – 7.
- Schuster, R., Scharbert, S., Abart, R., Frank, W., 2001. Permo-Triassic extension and related HAT/LP metamorphism in the Austroalpine-Southalpine realm. *Mitt. Ges. Geol. Bergbaustud.*, 45, 111-141.
- Sölva, H., Thöni, M., Grasemann, B., Linner, M., 2001. Emplacement of eo-Alpine high-pressure rocks in the Austroalpine Ötztal complex (Texel group, Italy/Austria). *Geodinamica Acta* 14 (2001) 345-360.
- Sölva, H., Grasemann, B., Thöni, M., Thiede, R., Habler, G., 2005. The Schneeberg Normal Fault Zone: normal faulting associated with Cretaceous SE-directed extrusion in the Eastern Alps (Italy/Austria). *Tectonophysics* 401(2005) 143-166.
- Stead, D., Eberhardt, E., Coggan, J.S., 2006. Developments in the characterization of complex rock slope deformation and failure using numerical modelling techniques. *Engineering geology* 83 (2006) 216 – 235.
- Stead, D., Coggan, J.S., 2006. Numerical modelling of rock slope using a total slope failure approach. In: Evans, S.G., Scarascia Mugnozza, G., Strom, A., Hermanns, R.L., 2006. *Landslides from massive rock slope failures*. Dodrecht, Netherlands: Springer, pp. 131-142.

- Stead, D., Coggan, J.S., 2012. Numerical modeling of rock-slope instability. In: Clague, J.J., Stead, D., 2012. Landslides: types, mechanisms and modeling. Cambridge University Press – pp 144-171.
- Stini, J., 1941. Unsere Taler wachsen zu: Geologie und Bauwesen. 18, 71 - 79.
- Styles, T.D., 2009. Numerical modelling and analysis of slope stability within fracture dominated rock masses. Ph.D. thesis. University of Exeter.
- Tang, C., Hudson, J.A., 2010. Rock failure mechanisms explained and illustrated. CRC Press – Taylor&Francis Group.
- Tansi, C., Sorriso-Valvo, M., Greco, R., 2000. Relationship between joint separation and faulting: an initial numerical appraisal. *Engineering Geology*, 52: 225-230.
- Terzaghi K., 1963 – Stability of steep slope on hard unweathered rock. *Geotechnique* 1962:12:251-270
- Thöni, M., 1999. A review of geochronological data from the Eastern Alps. *Schweiz. Mineral. Petrogr. Mitt.* 79 (1), 209-230.
- Van Gool, J.A.M., Kempe, M.M.J., Schreurs, G.M.M.F., 1987. Structural investigation along an E-W cross-section in the southern Ötztal Alps. In: Flügel, H.W. & Faupl, P. (ed.) *Geodynamics of the Eastern Alps*. Deuticke Wien, Vienna, 214-225.
- Van Husen, D., 1997. LGM and late-glacial fluctuation in the eastern Alps. *Quaternary International.*, Vols 38/39, pp. 109-118.
- Van Husen, D., 2000. Geological processes during the Quaternary. *Mitteilungen der Österreichische Geologische Gesellschaft* 92, 135-156.
- Van Husen, D., 2004. Quaternary glaciations in Austria. In: Ehlers, J., Gibbard, P.L., (Eds.), 2004. *Quaternary Glaciations – Extent and Chronology Part I: Europe*. Elsevier, London, pp. 1-13.



- Varnes, D.J., 1978. Slope Movement Types and Processes. In Special Report 29: Landslides and Engineering Practice (E.B. Eckel, ed.), HRB, National Research Council, Washington DC, pp. 20-47, 1958.
- Whittaker, B.N., Singh, R.N., Sun, G., 1992. Rock fracture mechanics: principles, design and applications. Amsterdam: Elsevier, pp. 570.
- Willye, D., Mahr, C., 2005. Rock Slope Engineering – Civil and Mining. Spon Press, Taylor and Francis Group, 4<sup>th</sup> edition.
- Yan, M., 2008. Numerical modelling of brittle fracture and step-path failure: from laboratory to rock slope scale. Ph. D. Thesis – Simon Fraser University.
- Zanchetta, S., 2010. The Texel-Schneeberg boundary in the Pfossen valley (Merano, NE Italy): geological-structural map and explanatory notes. Italian Journal of Geosciences (Boll.Soc.Geol.It.), Vol. 129, No. 2 (2010), pp. 395-407.
- Zangerl, C., Eberhardt, E., Perzmaier, S., 2012. Kinematic behavior and velocity characteristics of a complex deep - seated crystalline rockslide system in relation to its interaction with a dam reservoir. Engineering Geology, 112, 53 - 67.
- Zischinsky, U., 1966. On the deformation of high slopes. Proceeding of the First Congress of the International Society of Rock Mechanics, Lisboa, 2, 179-185.
- Zischinsky, U., 1969. Über Sackungen. Rock Mech. 1(1), 30-52.
- Zorzi, L., Massironi, M., Surian, N., Genevois, R., Floris, M., -. How multiple - foliation may control large gravitational phenomena: a case study from the Cismon Valley, eastern Alps, Italy. Geomorphology - accepted, pending revisions.

#### Web-reference

<http://www.provincia.bz.it/informatica/cartografia/cartografia-download.asp>

<http://www.silverschmidt.com/>

# 9. Appendix A

Neutral file used in the hybrid FEM/DEM ELFEN code.

```
# Material database = ridnaun
# Material selected = osc_eb
# Non linear Criterion = rankine_with_fracture
Material_data { 7
  Material_name {
    "osc_eb"
  }
  Elastic_material_flags { NFGELA { 4 }
    0 1 0 0
  }
  Elastic_properties { NMPRP { 15 }
    3e+010 0 0 0.3 0 0 0 0 0 0 0 2700 0 0
  }
  Plastic_material_flags { NMFPLS { 2 }
    0 19
  }
  Plastic_properties { NPRPLS { 5 }
    6e6 40 5 1.5e6 200
  }
  Failure_material_flags { 3
    0 1 1
  }
  Failure_properties { 2
    1e6 200
  }
  Fracturing_material_flags { 2
    0 1
  }
  Fracturing_properties { 1
    0
  }
}
```

```

}
Number_state_variables {
  12
}

# Material database = ridnaun
# Material selected = smu_eb
# Non linear Criterion = rankine_with_fracture
Material_data { 6
  Material_name {
    "smu_eb"
  }
  Elastic_material_flags { NFGELA { 4 }
    0 1 0 0
  }
  Elastic_properties { NMPRP { 15 }
    2.1e+010 0 0 0.27 0 0 0 0 0 0 0 0 2700 0 0
  }
  Plastic_material_flags { NMFPLS { 2 }
    0 19
  }
  Plastic_properties { NPRPLS { 5 }
    3e6 30 5 1e6 200
  }
  Failure_material_flags { 3
    0 1 1
  }
  Failure_properties { 2
    1e6 200
  }
  Fracturing_material_flags { 2
    0 1
  }
  Fracturing_properties { 1
    0

```

```
}  
Number_state_variables {  
  12  
}  
}
```